DOCTORAL PROGRAM IN
INFORMATION AND COMMUNICATION TECHNOLOGY

Doctoral candidate

Davide Pirrone

Cycle	**30°**
Thesis	**Advanced Methods for Change Detection in Multi-polarization and Very-High Resolution Multitemporal SAR Images**
Advisor	**Francesca Bovolo (Fondazione Bruno Kessler)**
Co-advisor	**Lorenzo Bruzzone (University of Trento)**

1. List of publications

- **Book chapters:**

  - M. Dalla Mura, J.A. Benediktsson, J. Chanussot, L. Bruzzone, “Advances in Change Detection Techniques for Multitemporal SAR Images”, in Mathematical Models for Remote Sensing Image Processing, Ed. B. Aiazzi, F. Bovolo, L. Bruzzone, A. Garzelli, D. Pirrone, C. Zoppetti, Springer Verlag, ISBN-13.

- **Conference Proceedings:**

  - Pirrone, D., Bovolo, F. and Bruzzone, L., "Analysis of backscattering behaviors for partially damaged buildings in VHR SAR images." In Proceedings of *SPIE Remote Sensing* (Tolouse, France, September 21 – 24, 2015).

  - Pirrone, D., Bovolo, F. and Bruzzone, L., "A novel framework for change detection in bi-temporal polarimetric SAR images." In Proceedings of SPIE Remote Sensing (Edinburgh, France, September 26 – 29, 2016).

  - De, S., Pirrone, D., Bovolo, F., Bruzzone, L., Bhatthacharya, A., “A novel change detection framework based on deep learning for the analysis of multi-temporal polarimetric SAR images” In Proceedings of *IEEE Geoscience And Remote Sensing Symposium (IGARSS)* (Forth Worth, United States, July 23-28, 2017)

  - Pirrone, D., De, S., Bhattacharya, A., Bruzzone, L., Bovolo, F., “Unsupervised change detection in built-up areas by multi-temporal polarimetric SAR images” In Proceedings of *IEEE Geoscience And Remote Sensing Symposium (IGARSS)* (Forth Worth, United States, July 23-28, 2017)

- **Submitted, Under Review and Ready to Submit**

  - Pirrone, D., De, S., Bhattacharya, A., Bruzzone, L., Bovolo, F., “An Unsupervised Approach to Change Detection in Built-Up Areas by Multi-Temporal Full-pol SAR Images”, In *IEEE Geoscience and Remote Sensing Letters* (submitted).

  - Pirrone, D., Bovolo, F., Bruzzone, L., “An Approach to Unsupervised Detection of Fully and Partially Destroyed Buildings in Multi-temporal VHR SAR Images" In *IEEE Transactions of Geoscience and Remote Sensing* (ready to submit).

  - Pirrone, D., Bovolo, F., Bruzzone, L., “A Novel Framework for Unsupervised Multi-class Change Detection in Dual-pol Intensity SAR Images”, In *IEEE Transactions of*

Geoscience and Remote Sensing (ready to submit).

2. Research/study activities

- **Period abroad**

  - Internship of 3 months in the Laboratoire d'Informatique, Systèmes, Traitement de l'Information et de la Connaissance, Université de Savoie, (supervisors: Prof. A. Atto and Prof. E. Trouvé).

- **Reviewer Activities**

  - IEEE Transactions of Geoscience and Remote Sensing
  - IEEE Journal of Selected Topics in Applied Earth Observations and Remote Sensing
  - IEEE Geoscience and Remote Sensing Letters
  - International Journal of Applied Earth Observations and Geoinformation

- **Student Co-supervision**

  - "Change Detection in Polarimetric SAR Images", Maddalena Sebastiani (master course project)
  - "Damage detection in Urban areas from complex PolSAR images", Thomas Leardini (master course project)
  - "Texture-based Change Detection in Urban Areas from VHR SAR images", Antonio Fiore (bachelor thesis)
  - "Automatic Detection of Partially and Fully Destroyed Buildings in Multitemporal VHR SAR data" Daniel Bogale Aykadu (master thesis)
  - "A Novel Approach to Multiple-Change Detection in Complex Polarimetric SAR Data", Annalisa Tomasini (master thesis).
  - "Integrazione di immagini satellitari a risoluzione molto elevate e dati vettoriali OpenStreetMap", Enrico Cescato (high-school project)

PhD Dissertation



International Doctorate School in Information and Communication Technologies

DISI - University of Trento

Advanced Methods for Change Detection in Multi-polarization and Very-High Resolution Multitemporal SAR Images

Davide Pirrone

Advisor:
Dr. Francesca Bovolo
Fondazione Bruno Kessler

Co-Advisor:
Prof. Lorenzo Bruzzone
Università degli Studi di Trento

January 2019

I am tormented with an
everlasting itch for things remote.
I love to sail forbidden seas.
(H.Melville)

Abstract

Change Detection (CD) aims at identifying physical changes in multi-temporal data of the same scene. It is one of the most important topics in multi-temporal remote sensing image analysis, because of its many monitoring applications. One of the most important imaging sensors for CD is Synthetic Aperture Radar (SAR), which have imaging capabilities for all-day all-weather conditions. In the last two decades, a relevant increase of SAR imagery has been observed with (sub)metric resolution (Very High Resolution SAR) and/or with multiple polarimetric channels (Polarimetric SAR). The two kinds of SAR imagery provide an enhanced information with respect to the past that can be investigated for improving the CD capabilities. To this end, novel advanced methodologies need to be designed. In this thesis, we devoted our attention to improving the state of the art both in PolSAR and VHR SAR multi-temporal image analysis with focus on change detection. Concerning the PolSAR imagery, the availability of multi-polarization multi-temporal scattering information represents an added value for detecting changes. In the literature, polarimetric information has been mainly exploited for single-data image classification, exploring the discrimination capabilities of the polarimetric features. For CD applications, the largest part of the literature considered PolSAR imagery for tackling binary CD only and a poor effort has been devoted in the discrimination of multiple kinds of change classes. However, polarimetric data can provide relevant information in many monitoring applications

. In this thesis, we aim at developing advanced methodologies for the exploitation of the polarimetric information in multi-temporal information extraction. More in detail the contributions are focused on the following tasks.

1. *An approach for unsupervised multi-class change detection in bi-temporal dual-pol SAR images is proposed. The approach is based on a multi-dimensional change index that describes the multitemporal scattering behaviors of samples along each polarimetric channel. Based on the scattering theory, the change index is expected to behave in different ways according to the kind of change. A theoretical analysis is conducted to detect change preferred direction and an unsupervised strategy based on this index is designed to automatically distinguish among the multiple change classes.*

2. *An approach for unsupervised change detection of built-up areas from bi-temporal full-pol SAR images is proposed. The approach introduces a novel change index based on both scattering power and scattering mechanism information for focusing*

on changes built-up elements.

3. *An approach for the characterization of the temporal evolution and change dynamics in full-pol SAR image time-series is proposed. The approach exploits both the main polarimetric decomposition features and the wavelet analysis in the time domain. It explores wavelet approximation and detail components for multi-temporal classification and change detection purposes.*

Concerning the VHR SAR imagery, the metric resolution represents a key factor in analysis of built-up areas, allowing for building level analysis. The investigation of VHR SAR imagery has proven to be effective in the detection of fully destroyed buildings, because of the large difference in the scattering pattern before and after the destruction. Less effort has been devoted in the analysis of partially-destroyed buildings. However, this building category has also a critical role in damage-assessment applications, thus partially-destroyed building detection represents a relevant topic.
In this thesis, an approach for the unsupervised detection of fully and partially destroyed buildings in bi-temporal VHR SAR images is proposed. A novel multi-temporal scattering model for partially destroyed buildings is introduced to the literature and integrated, together with the model of fully destroyed buildings, into a hierarchical change detection strategy, based on the expected change size.
For all the contributions, an analysis of the state of the art and limitations is conducted. Then, a detailed description of the proposed methods is provided. Experimental results for each of the methods are illustrated to confirm their validity.

Keywords:
Remote Sensing, Radar, Bi-temporal Change Detection, Multi-polarization, Very High Resolution, Polarimetric Change Vector, Multi-class Change Detection, Built-up Change Detection, Building Change Detection, Partially-Destroyed Building.

Acknowledgements

Because of the large period of time of the PhD, many acknowledgments are due to people who supported me for many years and contributed to part of this work. I will try my best for writing them all.
First of all, I would like to thank Dr. Francesca Bovolo for the privilege of having her as my supervisor. She taught me how to tackle research goals and she gave me technical and human support during times harsher than usual.
A special thank to Prof. Lorenzo Bruzzone, which I had the honor of having as co-advisor. Since my first informal meeting in a cafeteria of Rome, his forward thinking, his divulgation capabilities and his deep knowledge of the topic made me understand what people I would be glad to become in my next future.
A special thank is also due to Prof. Abdourrahmane Atto and Prof. Emmanuel Trouvé for giving me their precious support during my collaboration at Université Savoie Mont-Blanc. A special thank is also due to Prof. Guillaume Ginolhac and his family, for his warm welcome during my earlier days in Annecy.
I would like to thank all the past and present staff of the Remote Sensing Laboratory at the Department of Information Engineering and Computer Science, University of Trento. In particular, I would like to thank Aravind and Elena for their positivity and resilience, during both good and harsh times. I would like to thank all the staff of the Computer Science, Systems, Information and Knowledge Processing Laboratory, Université Savoie Mont-Blanc, for their warm welcome and for the nice little moments spent during my days in Annecy. In particular, I would like to thank Emna, Alex, Hela and Étienne for their attitude of life. I would like to thank the friends living in Rome and in my hometown Isernia, for holding the friendship flame on. I would like to thank Prof. Avik Bhattacharya for all the interesting scientific discussions on old and new topics, and Dr. Shaunak De, for his polyhedral spirit and for proposing Skype calls on scientific topics on any possible time.
From each of them, I tried to learn at least a bit of what they have shown me during all the time spent together. But foremost, I would like to thank my family and Rosanna for all their support. The accomplishment of this work is partially theirs.

The work compiled in this thesis has been fully supported by the research grant from the Fondazione Bruno Kessler, Italy.

Contents

1 Introduction **1**

1.1 Introduction and Motivations 1

1.1.1 Overview of the Novel Contributions 4

1.1.2 A Novel Framework for Unsupervised Multi-class Change Detection in Dual-pol Intensity SAR Images 4

1.1.3 An Unsupervised Approach to Change Detection in Built-Up Areas by Multi-Temporal Full-pol SAR Images 5

1.1.4 Wavelet Temporal Analysis of Polarimetric Decomposition Parameters over Alpine Glaciers 5

1.1.5 An Unsupervised Approach to Change Detection in Built-Up Areas by Multi-Temporal Full-pol SAR Images 5

1.2 Structure 6

2 State of the art **9**

2.1 Background on SAR imagery 9

2.1.1 SAR imaging principle 10

2.1.2 SAR image properties 11

2.1.3 Polarimetric SAR (PolSAR) imagery 12

2.1.4 Very High Resolution SAR (VHR SAR) imagery 15

2.2 Unsupervised Change Detection in SAR imagery 16

2.2.1 Bi-temporal Comparison 18

2.2.2 Change information extraction 20

2.3 Unsupervised Change Detection in PolSAR imagery 25

2.4 Unsupervised Change Detection in VHR SAR imagery 26

3 A Novel Framework for Unsupervised Multi-class Change Detection in Dual-pol Intensity SAR Images **29**

3.1 Introduction 30

3.2 Intensity-based Polarimetric Change Vector Analysis 33

3.2.1 Polarimetric Change Vector . . . 33
3.2.2 Single date backscattering behavior . . . 35
3.2.3 Multi-temporal backscattering behavior: change model . . . 37
3.3 Proposed CD Approach in Dual-Pol SAR images . . . 40
3.3.1 Binary CD along the magnitude . . . 41
3.3.2 Multi-class CD along the direction . . . 43
3.4 Experimental Results . . . 45
3.4.1 Chennai dataset . . . 46
3.4.2 Los Angeles dataset . . . 51
3.4.3 Sardinia dataset . . . 55
3.5 Conclusion . . . 56

4 An Unsupervised Approach to Change Detection in Built-Up Areas by Multi-Temporal Full-pol SAR Images 61
4.1 Introduction . . . 61
4.2 Proposed CD approach in Full-pol SAR images . . . 63
4.2.1 Definition of the change index . . . 64
4.2.2 Automatic Change Detection of built-up areas . . . 65
4.2.3 CD of built-up areas in large images . . . 66
4.3 Experimental Results . . . 67
4.3.1 Single-change Scenario . . . 68
4.3.2 Multi-change Scenario . . . 68
4.4 Conclusion . . . 72

5 Wavelet Temporal Analysis of Polarimetric Decomposition Parameters over Alpine Glaciers 75
5.1 Introduction . . . 75
5.2 Proposed multi-temporal framework for Full-pol SAR images . . . 77
5.2.1 Definition of the polarimetric features . . . 77
5.2.2 Definition of the geometrical and arithmetical wavelet operators . . . 78
5.2.3 L-size Spline Stationary Wavelet transform (SSW) . . . 79
5.2.4 Multiscale Discrete Wavelet transform with L-size filters (MDW) . . . 80
5.3 Data processing . . . 80
5.4 Experimental results . . . 83
5.4.1 Separation of multi-temporal classes . . . 84
5.4.2 Change Detection and Evolution Analysis . . . 86
5.5 Conclusion . . . 89

6 An Unsupervised Approach to Change Detection in Built-Up Areas by Multi-Temporal Full-pol SAR Images **95**
6.1 Introduction . . . 95
6.2 Building scattering model in single-time VHR SAR images . . . 98
6.2.1 Standing Building . . . 98
6.2.2 Fully Destroyed Building . . . 100
6.2.3 Partially Destroyed Building . . . 101
6.3 Building scattering model in multi-temporal VHR SAR images . . . 105
6.3.1 Fully destroyed buildings . . . 106
6.3.2 Partially destroyed building . . . 107
6.4 Proposed approach for unsupervised building Change Detection in VHR SAR images . . . 110
6.4.1 Multi-temporal comparison and Backscattering CD . . . 111
6.4.2 Hierarchical level 1: Fully-destroyed building detection (FDBD) . . 112
6.4.3 Hierarchical level 2: Partially-destroyed building detection (PDBD) 114
6.4.4 CD Map Fusion . . . 115
6.5 Experimental Results . . . 115
6.5.1 Crop 1: Modern Residential Area . . . 116
6.5.2 Crop 2: Medieval Residential Area . . . 120
6.6 Conclusion . . . 123

7 Discussion and future developments **125**
7.1 Conclusions . . . 125
7.2 Future developments . . . 127
7.2.1 Book Chapters . . . 128
7.2.2 International Conferences . . . 128
7.2.3 International Journals (Submitted, Under Review and Ready to Submit) . . . 128

Bibliography **131**

List of Tables

2.1 Overview of the principal bi-temporal CD methods for MR-SAR imagery. . 24
2.2 Overview of the principal bi-temporal CD methods for Polarimetric SAR imagery. 27

3.1 Overview of the multi-temporal acquisitions for the experimental results. . 46
3.2 Chennai dataset: confusion matrix, and overall accuracy (OA) for the proposed approach (Otsu Thresholding). 49
3.3 Chennai dataset: performance comparison with state-of-the-art methods. . 49
3.4 Los Angeles dataset: confusion matrix, and overall accuracy (OA) for the proposed approach (Otsu thresholding). 53
3.5 Los Angeles dataset: performance comparison with state-of-the-art methods. 53
3.6 Sardinia dataset: confusion matrix, and overall accuracy (OA) for the proposed approach (Bayesian thresholding). 59
3.7 Sardinia dataset: performance comparison with state-of-the-art methods. . 59

4.1 Confusion Matrix for the proposed approach. (Single-change scenario). . . 70
4.2 Overview of Performance assessment. (Single-change Scenario). 70
4.3 Confusion Matrix for the proposed approach. (Multi-change scenario). . . . 72
4.4 Overview of Performance assessment. (Multi-change scenario). 72

5.1 Kullback-Leibler distance for the empirical distributions of eigenvalue-eigenvector decomposition features with Gaussian and Gamma ditribution. 84
5.2 Performance analysis for overall class separation indicator, for different polarimetric features and wavelet strategies. 89
5.3 Performance analysis for δ, for different polarimetric features and wavelet strategies. 90
5.4 Performance analysis for R_C, for different polarimetric features and wavelet strategies. 90

6.1 Homogeneous surface-scattering regions for standing building scenario . . 99

6.2 Surface scattering contributions for partially-destroyed building. 102
6.3 Multi-bounce contributions for partially-destroyed building. 103
6.4 Parameters used in the experiments: (a) common parameters; (b) FDBD and PDBD specific parameters. 119
6.5 Crop 1: Detection assessment of the proposed approach for L'Aquila dataset. 120
6.6 Crop 2: Detection assessment of the proposed approach for L'Aquila dataset. 123

List of Figures

1.1 Temporal evolution of the geometrical resolution capabilities for SAR systems. 2
1.2 Temporal evolution of the polarimetric capabilities for SAR systems. Because of the processing boundaries, SAR systems operate with a trade-off between fine geometrical resolution and the use of more polarimetric channels. 3

2.1 SAR imaging geometry. 10
2.2 Geometrical distortions in SAR images. 12
2.3 Polarimetric imaging principle. 13
2.4 SAR images from TerraSAR-X sensor acquired over the Luneburg urban area (Germany): (a) MR image (simulated); and (b) VHR image. 16
2.5 Block scheme for a CD approach based on post-classification comparison. . 17
2.6 Block scheme for a CD approach based on joint analysis of the multi-temporal images. 17
2.7 Block scheme for a CD approach based the multi-temporal comparison and the extraction of the change information. 18

3.1 Change behavior in the PCV feature space. 40
3.2 Block diagram of the change detection method. 41
3.3 Chennai dataset: multi-temporal backscattering false color composition for (a) VV Channel; (b) VH Channel. R, B: Oct. 2015; G: Nov. 2015. No-change appears in gray shades, backscattering increase and decrease in green and magenta, respectively. 48
3.4 Chennai dataset: bivariate polar histogram (white dashed circle - T_ρ, black dashed line - T_{12}). 48
3.5 Chennai dataset: magnitude mixture model. 48
3.6 Chennai dataset: (a) BIC analysis with respect K (minimum value is reached for $K = 2$); (b) direction histogram and estimated mixture model for $K = 2$. 49

3.7 Chennai dataset maps: (a) Reference; (b) Proposed (Bayesian thresholding); (c) Proposed (Otsu thresholding); (d) LLR; (e) EM2DGM; (ω_{nc} - white, Ω_c - black, ω_{c1} - blue, ω_{c2} - red). 50
3.8 Los Angeles dataset: multi-temporal backscattering false color composition for (a) HH Channel; (b) HV Channel. R, B: Apr. 2009; G: May. 2015; No-change appears in gray shades, backscattering increase and decrease in green and magenta, respectively. 52
3.9 Los Angeles dataset: bivariate polar histogram (white dashed circle - T_ρ, black dashed line T_{12}). 52
3.10 Los Angeles dataset: magnitude mixture model. 52
3.11 Los Angeles dataset: (a) BIC analysis with respect K (minimum value is reached for $K = 2$); (b) direction histogram and estimated mixture model for $K = 2$. 53
3.12 Los Angeles dataset maps: (a) Reference; (b) Proposed (Bayesian thresholding); (c) Proposed (Otsu thresholding); (d) LLR; (e) EM2DGM; (ω_{nc} - white, Ω_c - black, ω_{c1} - blue, ω_{c2} - red). 54
3.13 Sardinia dataset: multi-temporal backscattering false color composition for (a): HH Channel; (b) HV Channel. R, B: May. 2016; G: Jul. 2016. No-change appears in gray shades, backscattering increase and decrease in green and magenta, respectively. 56
3.14 Sardinia dataset: bivariate polar histogram (white dashed circle - T_ρ, black dashed lines - T_{12}, T_{23}). 57
3.15 Sardinia dataset: magnitude mixture model. 57
3.16 Sardinia dataset: (a) BIC analysis with respect K (minimum value is reached for $K = 3$); (b) direction histogram and estimated mixture model for $K = 3$. 57
3.17 Chennai dataset maps: (a) Reference; (b) Proposed (Bayesian thresholding); (c) Proposed (Otsu thresholding); (d) LLR; (e) EM2DGM; (ω_{nc} - white, Ω_c - black, ω_{c1} - blue, ω_{c3} - gray, ω_{c3} - red). 58

4.1 Block scheme for the proposed approach. 63
4.2 Pauli RGB false-color composite for (a) pre-, and (b) post-event scene; (c) Δ. (Single-change scenario). 68
4.3 (a) CD map for the proposed approach; (b) Reference map ; (c) CD map for LLR. (Single-change scenario, ω_{nc} - white, ω_{c2} - black) 69
4.4 (a) CD map for HHLR-BT; (b) CD map for GD-PCAK; (c) CD map for $\Delta\alpha$-BT. (Single-change scenario, ω_{nc} - white, ω_{c2} - black) 69

4.5 Pauli RGB false-color composite for (a) pre-, and (b) post-event scene; (c) Δ. (Multi-change scenario). 70
4.6 (a) CD map for the proposed approach; (b) Reference map; (c) CD map for LLR. (Multi-change scenario, ω_{nc} - white, ω_{c1} - orange, ω_{c2} - black). . . 71
4.7 (a) CD map for HHLR-BT; (b) CD map for GD-PCAK; (c) CD map for $\Delta\alpha$-BT. (Multi-change scenario, ω_{nc} - white, ω_{c1} - orange, ω_{c2} - black). . . 71

5.1 Example of Stationary wavelet based on Haar-1 family. 81
5.2 Example of Spline stationary wavelet of 3 elements based on Haar-1 family. 81
5.3 Example of multi-scale wavelet analysis based on Haar-1 family (2 levels). . 81
5.4 Pauli false color composition for times t_1 (a) and t_7 (b); R1 - Cyan; R2 - Magenta; R3 - Green; R4 - Blue; R5 - Yellow; R6 - Red. 82
5.5 Images from the approximation component of SW-H, SW-α and SW-A, for t_1, t_2 (a,b,c) and t_6, t_7 (d,e,f), respectively. 85
5.6 Images from the approximation component of SSW-H, SSW-α and SSW-A, for t_1, t_2, t_3 (a,b,c) and t_5, t_6, t_7 (d,e,f), respectively. 86
5.7 Images from the approximation component of SW-f_s, SW-f_d, SW-f_v and SW-f_h, for t_1, t_2 (a,b,c,d) and t_6, t_7 (e,f,g,h), respectively. 87
5.8 Images from the approximation component of SSW-f_s, SSW-f_d, SSW-f_v and SSW-f_h, for t_1, t_2, t_3 (a,b,c,d) and t_5, t_6, t_7 (e,f,g,h), respectively. 87
5.9 Temporal trend for the approximation component of: SW-H (a); SW-α (b); SW-f_h (c); SW-f_v (d). 88
5.10 Images from the detail component of SW-H, SW-α and SW-A, for t_1, t_2 (a,b,c) and t_6, t_7 (d,e,f), respectively. 91
5.11 Images from the detail component of SSW-H, SSW-α and SSW-A, for t_1, t_2, t_3 (a,b,c) and t_5, t_6, t_7 (e,f,g), respectively. 92
5.12 Images from the detail component of SW-f_s, SW-f_d, SW-f_v and SW-f_h, for t_1, t_2 (a,b,c,d) and t_6, t_7 (e,f,g,h), respectively. 93
5.13 Images from the detail component of SSW-f_s, SSW-f_d, SSW-f_v and SSW-f_h, for t_1, t_2, t_3 (a,b,c,d) and t_5, t_6, t_7 (e,f,g,h), respectively. 93
5.14 Temporal trend for the approximation component of: SW-H (a); SW-α (b); SW-f_h (c); SW-f_v (d). 94

6.1 Standing building: (a) acquisition geometry and building slices for $\phi = 0$; (b) backscattering signature for a single slice, $L_R \geq L_{RT}$. Scattering terms: a (ground), b (double bounce), c (wall), d (roof), e (shadow). 99

6.2 Standing building with $\phi \neq 0$: (a) acquisition geometry and building slices; (b) example of backscattering pattern for a standing building, with $W > H \cot\theta$, $\phi = \pi/4$, $(K_a = 0.2, K_c = K_d = 5)$. 100

6.3 Partially destroyed building: (a) Acquisition geometry and building slices for $\phi = 0$; (b) Backscattering signature with surface scattering contributions for a single slice based on the ray-tracing method, $L_R \geq L_{RT2}$. Scattering terms: a (ground), c_w (wall), c_d (debris), d (roof), e (shadow). . 102

6.4 Example of acquisition geometry of partially destroyed building for $\phi \neq 0$ and building slices. Aspect angle effect generates four profiles, namely A (yellow), B (dark green), C (red) and D (light green). 104

6.5 Example of backscattering pattern for a partially destroyed building for $\phi = \pi/4, \Delta H_H = H/4, \alpha = \pi/6$ $(K_a = 0.2, K_c = K_d = 5)$. 105

6.6 Multi-temporal pattern for fully destroyed buildings, for (a) $\phi = 0$; (b) $\phi = \pi/4$. R,B: pre-event image; G: post-event image. Backscattering increase and decrease are represented in green and magenta, respectively. Representation of the geometrical features associated to the pair of regions R_I (in green) and R_D (in magenta) for the multi-temporal scattering pattern. 106

6.7 LR Patterns for partially destroyed buildings with different values set for parameters $\{\alpha, \Delta H_H, \phi\}$: (a) $\{\pi/12, H/4, 0\}$; (b) $\{\pi/12, H/4, \pi/3\}$; (c) $\{\pi/4, 3H/4, 0\}$; (d) $\{\pi/4, 3H/4, \pi/6\}$. Areas of backscattering decrease and increase are represented in magenta and green, respectively. 109

6.8 Hierarchical representation of the Building CD problem. 111

6.9 Block scheme of the proposed approach. 111

6.10 Set of moving windows used for the candidate detection with dimensions z_1, z_2. 113

6.11 Examples of membership function: a) Sigmoid function with $s = 10, t = 0.5$; and b) Gaussian function with $\mu = 0.35, \sigma^2 = 0.332$. 114

6.12 Crop 1: a) Multi-temporal false color composition of SAR images (R,B: September 2009, G: April 2009); b) Optical post-event image; c) Backscattering CD Map M_{opt}, with increase and decrease represented in magenta and green, respectively; d) Candidate gray-scale map $C^{(1)}$; e) Candidate gray-scale map $C^{(2)}$; f) Multi-class building CD map overlapped with multi-temporal false color composition of the SAR images (ω_1 (red), ω_3 (yellow), ω_4 (blue)). 117

6.13 Crop 1: Examples for buildings detected by the proposed approach: a) miss (above) and correct (below) detection for Fully Destroyed building class; b) correct detection for Partially Destroyed Building class; c) false alarm for Partially Destroyed Building class; d) miss detection for Partially Destroyed Building class. 121
6.14 Crop 2: a) Multi-temporal false color composition of SAR images (R,B: September 2009, G: April 2009); b) Optical post-event image; c) Backscattering CD Map M_{opt}, with increase and decrease represented in magenta and green, respectively; d) Candidate gray-scale map $C^{(1)}$; e) Candidate gray-scale map $C^{(2)}$; f) Multi-class building CD map overlapped with multi-temporal false color composition of the SAR images (ω_1 (red), ω_2 (green), ω_3 (yellow), ω_4 (blue)). 122

Chapter 1

Introduction

In this chapter, an overview of the proposed contributions is presented. The chapter delineates the importance of the change detection problem, the potentiality and the limits offered by the enhanced information in SAR imagery in terms of geometry (i.e., Very-High Resolution SAR imagery) or polarimetry (i.e., PolSAR imagery). These aspects point the novelty of the contributions of this thesis. Finally, a description of the structure of the thesis is presented.

1.1 Introduction and Motivations

Since long, remote sensing technology has proven to be an important support for the Earth observation and for understanding man-made and natural phenomena. The key aspect of the remote sensing, indeed, lies in the information acquisition when the targets are too far or complex to be studied with proximity sensing. Thus, imaging sensors, using either active or passive technology, are mounted on either spaceborne or airborne platforms and are able to provide satellite/airborne images for a wide range of applications. The most adequate choice depends on the geometrical and radiometrical characteristics the phenomenon to be analyzed [37; 129].
In the recent years, thanks to the support from satellite constellations and proper data policies, the scientific community dealt with a large amount of available images. This led the data processing and analysis turning to unsupervised or weakly supervised strategies. Moreover, the same support increased the interest of the community to the use of multi-temporal data. In particular, they have been applied to classification, which uses multi-temporal information for having larger robustness, and change detection.
This thesis focuses on the Change Detection (CD) problem, which aims at identifying changes through the analysis of two or more images acquired at different times over the same scene. CD is used for several applications related to the analysis of both man-made

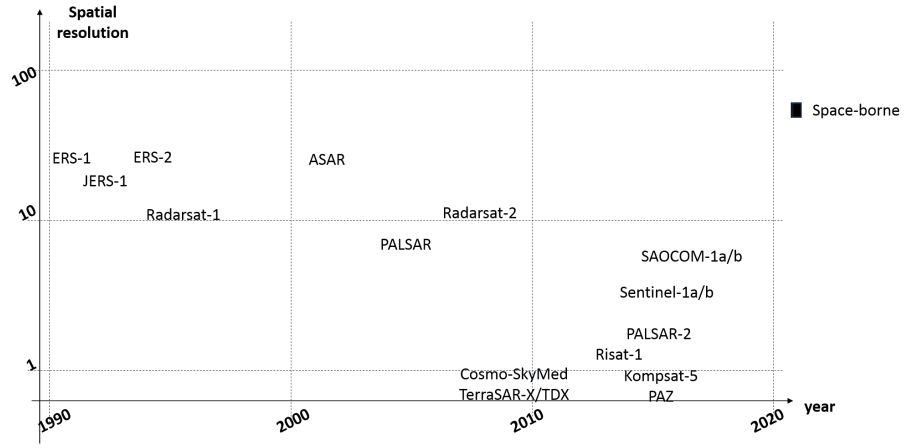

Figure 1.1: Temporal evolution of the geometrical resolution capabilities for SAR systems.

(e.g., damage assessment [33; 140], urbanization [17]) and natural scenes (e.g., crop monitoring [67], deforestation [215]). Looking at the change temporal scale, abrupt changes are evaluated with the comparison of a pair of multi-temporal images (i.e., pre- and post-event) [146], while smooth changes require the analysis of an image time seriesfor monitoring the evolution [97].

In remote sensing imagery, two main categories of images are considered, namely optical and SAR images. Optical images are acquired by passive sensors and present a large information content given by the multiple spectral channels in both the visible and the infrared spectrum. For these images, a large effort has been put in the development of automatic unsupervised CD methodologies [112; 139]. However, the utilization of the optical imagery is limited by the dependence on both the daytime season and the cloud-coverage weather conditions. Conversely, Synthetic Aperture Radars (SARs) are active sensors that transmit and receive coherent radiation backscattered from the targets with an off-nadir geometry. SAR systems may be designed at different microwave frequencies, ranging from the L (e.g., Sentinel-1 and PALSAR) to the X band (e.g., TerraSAR-X and Cosmo-SkyMed). The use of a microwave active technology makes these instruments insensitive to both night and cloud coverage, creating a benefit for the multi-temporal applications, where a prompt acquisition may be required. On the other hand, the interpretation of the SAR imagery is a complex task, because of the geometrical distortions over non-flat targets and the intrinsic speckle noise [165].

Let us consider the most important SAR systems operating in the last two decades. A large part of the available SAR imagery is characterized by a geometrical resolution in the order of decades of meters (i.e., Medium Resolution SAR) and the backscattering in-

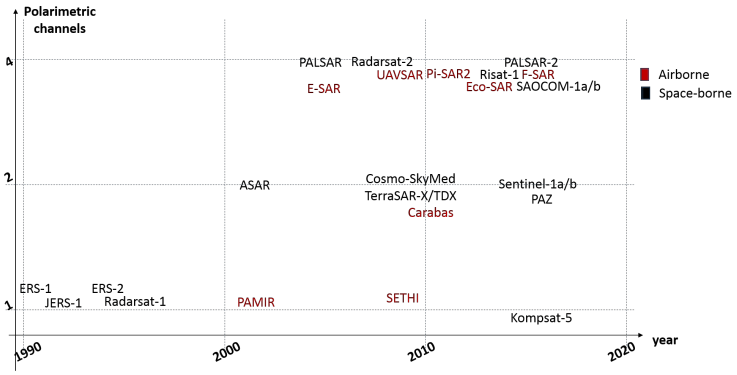

Figure 1.2: Temporal evolution of the polarimetric capabilities for SAR systems. Because of the processing boundaries, SAR systems operate with a trade-off between fine geometrical resolution and the use of more polarimetric channels.

formation measured with the same polarization for both the transmitted and the received radiation,i.e., single-pol information. The SAR of the ERS-1 mission, acquiring on the single VV polarimetric channel with a resolution of 30 meters (see Fig. 1.1 and Fig. 1.2), is an example of such systems. From the radiometrical perspective, this involves a limited characterization of the scattering. From the geometrical perspective, the comparison between the geometrical resolution and the average scatterer size presents the resolution cells as homogeneous and makes a pixel-based analysis as appropriate.

In the last decade, SAR sensors has shown a remarkable enhancement of the imaging capabilities in terms of geometrical resolution and polarimetric content. Concerning the geometrical resolution, some satellite missions (e.g., Cosmo-SkyMed, TerraSAR-X or TANDEM-X, see Fig. 1.1) and airborne missions provided data with resolution at metric or sub-metric scale, i.e. Very High Resolution (VHR) data [204; 40]. This kind of imagery provided a novel vision, in particular when focusing on a urban scenario, where we may have the necessity of discriminating targets at metric scale, such as buildings or part of them. In the CD perspective, some interest in the literature has been already devoted to the automatic analysis of urban changes at building scale (i.e., the detection of demolished or new buildings) [146]. A Poor effort has been spent in the analysis of VHR SAR data for discriminating multiple kind of building changes, depending on the change severity (i.e., different level of demolition) [119].

For MR SAR imagery, an enhancement in the polarimetric content has been achieved by means of Polarimetric SAR (PolSAR) systems, which detect backscattering information with different polarization combinations for the transmitted and the received radiation (e.g., Sentinel-1, which works with two polarimetric channels, or PALSAR2 and the future RADARSAT Constellation Mission, exploring the full combination, see Fig. 1.2). Polari-

metric capabilities have proven to largely help the target detection and the classification of SAR images in single-time analysis [122]. However, a small effort has been applied in the use of polarimetric information in change detection or isolating/separating different kinds of changes over multi-temporal SAR images [175].
Thus, advanced tailored methodologies need to be designed for: i) the exploitation of the polarimetric information for discriminating multiple change classes; ii) the exploitation of the meter-scale scattering information for discriminating building changes at different severity scale, because of the lack thereof.

1.1.1 Overview of the Novel Contributions

On the basis of the aforementioned considerations about both the VHR and the Polarimetric SAR imagery and the limitation in their use in the automatic detection of multiple kind of changes, this thesis focuses on the development of advanced methodologies for the unsupervised change detection in discriminating multiple kinds of change. Concerning the analysis of PolSAR imagery, the following contributions are introduced in this work.

1. an approach for unsupervised multi-class change detection in bi-temporal dual-pol intensity SAR images;

2. an approach for unsupervised change detection of built-up areas from bi-temporal full-pol SAR images;

3. an approach for the characterization of the temporal evolution and the detection of abrupt and smooth changes in full-pol SAR image time-series;

Concerning the analysis of VHR SAR imagery, the contribution of the thesis focuses on the detection of fully and partially destroyed buildings from bi-temporal VHR SAR images. The next sub-sections give a brief description of the proposed approaches.

1.1.2 A Novel Framework for Unsupervised Multi-class Change Detection in Dual-pol Intensity SAR Images

In the last decade, acquisitions from Polarimetric SAR systems have become more and more popular, in particular considering dual-pol acquisition mode (e.g, Sentinel-1). This increased the interest in the use of the polarimetric information for change detection applications. The literature tackled the problem by focusing on a binary CD problem, distinguishing classes of change and no-change only. However, the polarimetric information introduces the possibility of exploring the kind of the change and, thus, discriminating multiple change classes. In this work, a novel multi-dimensional change index is

introduced for the representation of the multi-temporal polarimetric information. Based on the scattering theory, the index introduces the discrimination of the different change classes. Based on this model, an automatic unsupervised CD strategy for bi-temporal dual-pol SAR images is presented. The strategy automatically estimates and separates the multiple kinds of changes.

1.1.3 An Unsupervised Approach to Change Detection in Built-Up Areas by Multi-Temporal Full-pol SAR Images

The use of full-polarimetric complex information has been often consider in the detection of urban targets by considering single-time SAR images, because of its scattering peculiarities. However, the multi-temporal changes of urban areas represent an important information that has been poorly tackled in the PolSAR-based literature. This contribution proposes an unsupervised approach for detecting changes of built-up elements in bi-temporal full-polarimetric SAR images. The approach introduces a novel change index, based on the joint use of overall scattering power and average scattering mechanism information, that is very sensitive to changes associated to built-up elements. Unsupervised thresholding of the proposed index based on the Bayesian theory leads to the identification of classes associated to constructed and demolished built-up elements.

1.1.4 Wavelet Temporal Analysis of Polarimetric Decomposition Parameters over Alpine Glaciers

The continued acquisitions from operating Polarimetric SAR systems led the scientific community to the use of image time series for multi-temporal applications, as they also guarantee information redundancy for a robust analysis. In order to define multi-temporal comparison operators, wavelet transform can be applied in the temporal domain. The transform can both provide average information, that can be adopted for making a robust estimation of the scene and used for discriminating different classes, and the detail information, associated to the change level of the sequence. This work investigates the performance of the combination of multiple polarimetric features and wavelet strategies for both the multi-temporal classification and changes analysis. An application scenario is considered for the analysis, describing the seasonal evolution of a glacier site in France.

1.1.5 An Unsupervised Approach to Change Detection in Built-Up Areas by Multi-Temporal Full-pol SAR Images

Multi-temporal SAR data with a metric geometrical resolution represent an important tool in the change detection of buildings. Based on the geometrical model of the building

and the scattering theory, multi-temporal models have been inferred for fully destroyed buildings, but it is frequent the case of buildings with partial damages. In this chapter, we propose a geometrical model for the partially destroyed building, based on specific assumptions, and we conduct a scattering analysis for the definition of a multi-temporal pattern associated to the damaged building. We integrate the model into an automatic unsupervised approach for the detection of both fully and partially destroyed buildings from multi-temporal VHR SAR data.

1.2 Structure

The thesis is organized into six chapters. In the present chapter, the motivations for the research contributions were presented and the novel contributions sketched.
Chapter 2 delineates the characteristics of the SAR imagery and the current state of the art for CD problem with multi-temporal in multi-temporal polarimetric and VHR SAR images.
Chapter 3 introduces a novel framework based on a pair of multi-temporal dual-pol intensity SAR images for the detection of multiple kinds of change. The framework maps changes into different regions of the proposed feature space, based on the polarimetric backscattering properties. It also estimates and automatically separates the optimal number of change classes. The effectiveness of the framework has been tested on three multi-temporal datasets with different kinds of change and different complexity, acquired by Sentinel-1.
Chapter 4 presents a novel approach for the automatic detection of changes in built-up areas based on the complex information of multi-temporal full-polarimetric SAR images. The method considers features coming from the state-of-the-art polarimetric decompositions in order to define a robust change index sensitive to the changes in the built-up elements. An unsupervised thresholding strategy is applied for detecting changes. The approach has been validated on two bi-temporal datasets of full-polarimetric images acquired by UAVSAR.
Chapter 5 presents a novel framework for time series of full-pol SAR images based on the joint use of arithmetical and geometrical wavelet transforms on full-polarimetric features. The multi-temporal features are exploited for both the separation of multi-temporal natural classes and for the analysis of changes with different temporal evolution. The proposed framework has been evaluated on a multi-temporal dataset of Radarsat-2 full-polarimetric image time series.
Chapter 6 introduces a novel methodology for the detection of partially and fully destroyed buildings in multi-temporal VHR SAR images. The methodology is based on the

definition of multi-temporal scattering model for fully and partially destroyed buildings, under some simplifying assumptions. For both the cases, the model is used for the definition of a fuzzy-logic set that associates patterns of multi-temporal scattering to buildings multi-temporal signatures. A hierarchical approach is considered for separating the building changes at different scales. The effectiveness of the framework has been tested on two multi-temporal VHR SAR datasets acquired by Cosmo-SkyMed constellation over the city of L'Aquila before and after the earthquake in 2009.
Finally, Chapter 7 draws the conclusions of this thesis and provides future developments. The chapters describing the novel contributions in this dissertation are to be considered as independent to each other and therefore result self-consistent. Readers interested to one of the aforementioned topics can read a single chapter without the need of reading the whole dissertation.

Chapter 2

State of the art

This chapter aims at providing a basic knowledge of the benefits and the drawbacks associated to SAR imagery with meter-scale resolution and with polarimetric information It also aims at illustrating the state of the art about the unsupervised change detection problem with VHR SAR and PolSAR imagery. The chapter is organized into four sections. The first section describes the fundamentals of SAR image processing at medium resolution, leading to the novel aspects introduced by both the VHR and the Polarimetric SAR systems. In the last three sections, an overview of the different unsupervised change detection methodologies present in the state of the art is illustrated for medium resolution SAR imagery (Section 2.2), where the research has been mainly focused in the past, then for Polarimetric SAR (Section 2.3) and for VHR SAR (Section 2.4) imagery.

2.1 Background on SAR imagery

SAR is an imaging active system operating in the microwave spectrum, in a range of frequencies delimited by the P (0.25-0.5 GHz) and the Ka band (25-40 GHz). Most of the operating SAR systems work in L (1-2 GHz), C (2-4 GHz) or X band (8-12 GHz). The SAR operating principle makes it poorly sensitive to both sunlight-illumination and cloud-coverage conditions and sensitive to the roughness and dielectric properties of the targets. These two peculiarities make SAR system as one of the most interesting remote sensing systems [182]. SAR systems exploit the radar principle, by transmitting microwave pulses and measuring the signal intensity and the target distance. In particular, a coherent measure of the intensity is obtained from the set of elementary scatterers present in the area element. SAR are mounted on moving platforms (i.e., airborne or spaceborne). By exploiting the platform movement along the azimuth direction, and the transmission of the signal with a squinted geometry along the slant-range direction, orthogonal to the movement, SAR creates a scattering intensity image in the range-azimuth domain. In

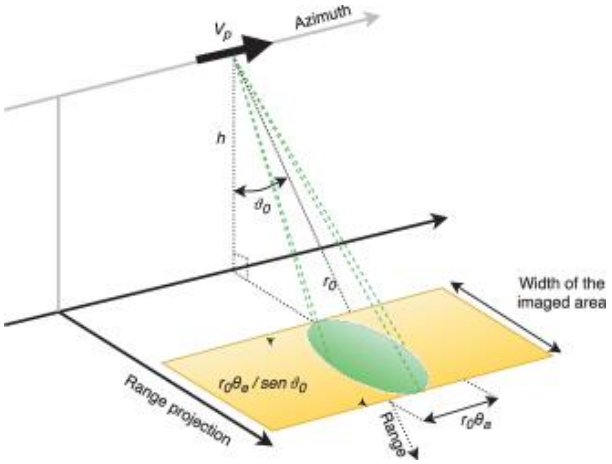

Figure 2.1: SAR imaging geometry.

order to improve the discrimination capabilities of the imaging radar, SAR exploits the use of proper signal waveforms and the target illumination from multiple positions in the azimuth direction.

2.1.1 SAR imaging principle

Fig. 2.1 shows the SAR imaging geometry. Let us define the nominal incidence angle θ of the radiation with respect to the target surface normal. It is possible to separate the analysis for range and azimuth directions. Along the range direction, the antenna illuminates the ground with an angle θ, while in the azimuth direction the pointing is vertical. For an antenna with dimensions l_{al}, l_{ac} along and across track respectively, radar footprint dimensions can be derived from the antenna theory [182].

$$S_r = \frac{\lambda R_0}{l_{al} \cos\theta} \tag{2.1}$$

$$S_a = \frac{\lambda R_0}{l_{ac}} \tag{2.2}$$

being R_0 and λ the slant-range distance of the target and wavelength of the microwave pulse. In order to evaluate the geometrical resolution on the range direction, we consider the pulse waveform. SAR systems use frequency-modulated signals like chirps, which have a instantaneous frequency linearly increasing with time $f_i(t) = r_c t$, being r_t the system chirp rate [165]. For a signal with time width τ and corresponding bandwidth $B_c = r_c \tau$, SAR presents a geometrical resolution along the ground range direction as follows:

$$\delta_{gr} = \frac{c_0}{2B \sin\theta} = \frac{\delta_{sr}}{\sin\theta} \tag{2.3}$$

being c_0 and δ_{sr} the wave propagation speed and the geometrical resolution along the slant range direction, respectively. The azimuth geometrical resolution equals to S_a for a real antenna, but the value is significantly improved by generating the synthetic aperture for the antenna. This considers the target illumination from multiple positions in azimuth (see Fig. 2.1), with the creation of an antenna with dimension L_{sa}:

$$L_{sa} = \frac{2\lambda R_0}{l_{ac}} \tag{2.4}$$

this leads to a final value δ_a for the azimuthal resolution:

$$\delta_a = \frac{\lambda R_9}{L_{sa}} = \frac{l_a c}{2} \tag{2.5}$$

2.1.2 SAR image properties

SAR imagery measures the target scattering, which typically considers an aleatory component modeled as Lambertian cosine law and a deterministic specular component. The presence of the two components is related to ratio between the target surface roughness, indicated in terms of a root-mean-square height s and λ. In particular, rough surfaces (i.e., $s >> \lambda$) tend to present a Lambertian scattering, while smooth surfaces (i.e., $s << \lambda$) tend to present a specular scattering.
As mentioned above, two important properties of the SAR images are the presence of a multiplicative noise on the scattering intensity and the strong geometrical distortions in presence of non-flat targets. The scattering echo propagating from the single elementary cell to the SAR antenna is a complex signal, composed by in-phase and quadrature components. Each of the two components is a coherent sum of the contributions from the multiple elementary scatterers of the target cell. An amplitude-phase representation for the overall signal is typically considered.

$$r(t) = \sum_{n=1}^{N} \sqrt{\sigma_{0n}} e^{j\phi_n} \tag{2.6}$$

being σ_{0n}, ϕ_n the intensity and the phase of the complex contribution from the n-th elementary scatterer and N the total number of elementary scatterers in the cell.
For MR SAR images on homogeneous regions, it is reasonable assuming a large values N for the resolution cells. This implies a fully-developed speckle phenomenon and a probabilistic modeling for the two signal components, assumed both with Gaussian distribution with same variance. The corresponding amplitude and intensity result distributed as Rayleigh-Rice and exponential probability density function (pdf), respectively. This results in a multiplicative noise effect on the SAR data. The effect can be mitigated by

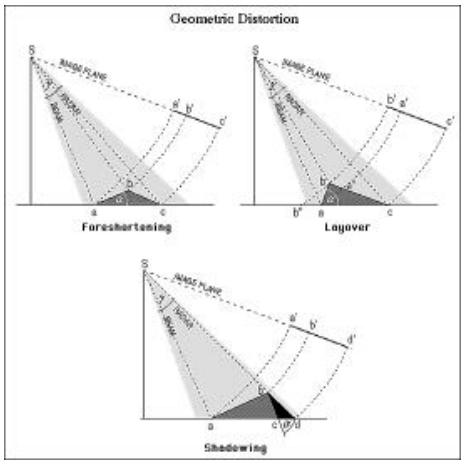

Figure 2.2: Geometrical distortions in SAR images.

considering an averaging homogeneous intensity values (multilooking). The multi-looked intensity is modeled with a random variable x Gamma distributed and presents a mean intensity reduced by a factor L, being L the Equivalent Number of Looks (ENL) and σ^2 the variance of the two Gaussian complex components [182; 143].

$$p(x) = \frac{L^L x^{L-1}}{\sigma^{2L}(L-1)!} \exp\left(-\frac{Lx}{\sigma^2}\right) \tag{2.7}$$

More flexible statistical models have been also proposed in the literature for SAR amplitude and intensity [156; 157; 120; 126]. Conversely, a uniform pdf is generally considered for the SAR phase.

Because the off-nadir acquisition geometry, the illumination of non-flat targets may generate three possible geometrical distortions. Fig. 2.2 provides an overview of the distortions. In the foreshortening effect, the sensor maps the inclined surfaces facing and opposing the sensor with shortened and lengthened regions, respectively. Layover sums multiple contributions from positions with same slant range and maps them into a bright single value. Conversely, shadow maps very low scattering for target elements occluded by obstacles [182].

2.1.3 Polarimetric SAR (PolSAR) imagery

In the interaction between the target and the microwave radiation, polarimetry plays an important role. We consider a plane of incidence containing the propagation direction vector and orthogonal to the surface. In that plane, the electrical field presents two components oscillating in the plane of incidence (i.e., parallel polarization) and on a orthogonal direction (i.e., orthogonal polarization). Assuming a linear polarization basis,

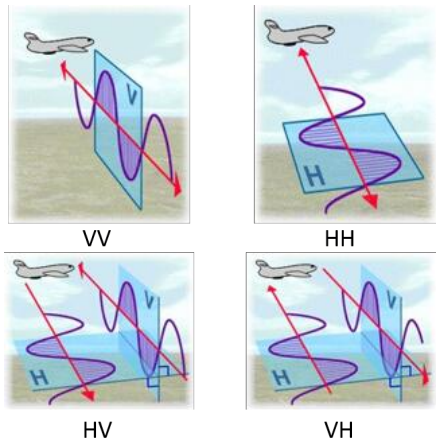

Figure 2.3: Polarimetric imaging principle.

parallel and orthogonal polarization are redefined as vertical and horizontal polarizations, respectively. By alternatively transmitting and receiving with the two orthogonal linear polarizations, co-polarization (co-pol) and cross-polarization (cross-pol) scattering complex coefficients are derived (see Fig. 2.3). They are represented in a more compact form as a scattering matrix S [182; 122].

$$S = \begin{bmatrix} S_{hh} & S_{hv} \\ S_{vh} & S_{vv} \end{bmatrix} \tag{2.8}$$

being S_{pq} the complex scattering coefficient measured for the transmission and reception with polarizations p and q respectively, $p, q \in \{H, V\}$. For natural targets, reciprocity theorem asserts the equivalence of the two cross-pol coefficients (i.e., $S_{hv} \simeq S_{vh}$). Classical SAR systems consider the single and same polarization for both transmitted and received radiation, measuring scattering on a single polarimetric channel (i.e., HH or VV for linear-polarization systems). A larger information content related to multiple polarimetric channels, is obtained with Polarimetric SAR (PolSAR) systems, which measure scattering on more polarimetric channels, by varying the polarization for the transmitted and/or received radiation. In particular, dual polarimetric (dual-pol) data consider two polarimetric channels with a fixed transmission polarization (i.e., HH-HV or VV-VH) or co-polarization channels only (i.e., HH-VV). Full polarimetric (full-pol) data consider all the polarimetric channels (i.e., HH-HV-VH-VV)

The scattering characterization with matrix S is reasonable only for elementary targets, with a deterministic behavior. Natural targets are distributed, thus their scattering is determined by the composition of multiple contributions from elementary scatters. Thus,

a scattering second-order statistics as the Covariance matrix C is considered as descriptor.

$$C = k_l^{\dagger} k_l = \begin{bmatrix} C_{11} & C_{12} & C_{13} \\ C_{21} & C_{22} & C_{33} \\ C_{31} & C_{32} & C_{33} \end{bmatrix} \tag{2.9}$$

being $k_l = \begin{bmatrix} S_{hh} & S_{hv} & S_{vv} \end{bmatrix}$ the complex scattering vector represented in the lexicographic basis. An alternative formulation considers a representation in the Pauli basis, with a scattering vector $k_p = \frac{1}{\sqrt{(2)}} \begin{bmatrix} [S_{hh} + S_{vv}; S_{hh} - S_{vv}; 2S_{hv} \end{bmatrix}$ and the corresponding Coherency matrix T.

$$T = k_p^{\dagger} k_p = RCR^T \tag{2.10}$$

$$R = \begin{bmatrix} 1 & 1 & 0 \\ 0 & 0 & \sqrt{2} \\ 1 & -1 & 0 \end{bmatrix} \tag{2.11}$$

In homogeneous areas, complex scattering vector can be modeled with a multivariate zero-mean Gaussian distribution, with covariance matrix Σ.

$$p(k, \Sigma) = \frac{1}{\pi^p |\Sigma|} \exp\left(-k^H \Sigma^{-1} k\right) \tag{2.12}$$

being p the number of polarimetric channels and k the complex scattering vector, $k \in \{k_l, k_p\}$. This makes the corresponding second-order statistics modeled with a complex Wishart distribution.

$$p(M) = \frac{1}{\Gamma_p(L)|\Sigma|^n} |C|^{L-p} \exp\{-tr|\Sigma^{-1} M|\} \tag{2.13}$$

being $tr(\cdot)$ the matrix trace operator, L the number of looks and $M \in \{C, T\}$. Advanced statistical models for polarimetric imagery of heterogeneous areas have been proposed in [79; 92; 30; 90].

T allows a simple representation of the scattering associated to different scattering mechanisms, in particular surface scattering, volume scattering and the double-bounce, associated to dihedral structures. The scattering intensity of these mechanisms is represented on the diagonal elements of T. Polarimetric decompositions from the state of the art can be applied to T in order to derive a set of few features describing the polarimetric behavior of the target [64]. In [65], eigenvalues λ_i and corresponding eigenvectors $v_i = \left[\cos\alpha_i, \sin\alpha_i \cos\beta_i e^{\delta_i}, \sin\alpha_i \sin\beta_i e^{\gamma_i}\right]^T e^{j\phi_i}$ of the matrix $T, i = 1, 2, 3, \lambda_1 > \lambda_2 > \lambda_3 \geq$ are used for deriving three polarimetric features, namely Anisotropy A, Entropy H and average Alpha angle α.

$$A = \frac{\lambda_2 - \lambda_3}{\lambda_2 + \lambda_3} \tag{2.14}$$

$$H = \sum_{i=1}^{3} \frac{\lambda_i}{\sum_{i=1}^{3} \lambda_i} \log \left(\frac{\lambda_i}{\sum_{i=1}^{3} \lambda_i} \right) \tag{2.15}$$

$$\alpha = \sum_{i=1}^{3} \frac{\lambda_i \alpha_i}{\sum_{i=1}^{3} \lambda_i} \tag{2.16}$$

H measures the degree of scattering randomness ranging from 0 (i.e., a single scattering mechanism is present) to 1 (i.e., all the scattering mechanisms have equal power). A measures the importance of the second dominant scattering mechanism in the range 0-1 as well. α characterizes the average scattering type of the target cell. High values are associated to the double-bounce scattering mechanism, while low values are associated to the surface scattering. Intermediate values are associated to the volume scattering [122]. Other strategies consider T as the linear combination of contributions associated to elementary targets, for which coherency matrix can be derived from the scattering properties. In particular, most of the power-based decompositions consider three [211; 89; 122] or four contributions [26; 220; 187], associated to the double-bounce, surface, volume and helix scattering.

$$T = f_s T_{surf} + f_d T_{double} + f_h T_{helix} + f_v T_{volume} \tag{2.17}$$

being $f_s, f_v, f_h, f_d, T_{surf}, T_{volume}, T_{helix}, T_{double}$ the power coefficients and the coherency matrices associated to the surface, volume, helix and double-bounce mechanism, respectively [122]. The two polarimetric decompositions are at the base of both the CD method presented in Chapters 4 and 5.

2.1.4 Very High Resolution SAR (VHR SAR) imagery

As introduced above, the VHR SAR are characterized by a metric or sub-metric geometrical resolution. In the analysis of urban areas, this resolution introduces the capability of investigating the scene at building level. Fig. 2.4a and 2.4b shows a comparison of two SAR example images acquired over urban areas at medium and very-high resolution, respectively.

In VHR SAR imagery, the comparison of the metric geometrical resolution and the common targets makes the number of elementary scatterers in the resolution cell much lower than that for MR SAR imagery. Thus, the speckle is not fully developed and the scattering composition presents a more complex probabilistic behavior than that described above. In the literature, different statistical models have been proposed for both the scattering amplitude and the intensity over heterogeneous regions. They rely on a statistical model with two aleatory variables associated to the speckle and the texture of the scene [90; 203; 227], respectively. The texture becomes uniformly distributed in the

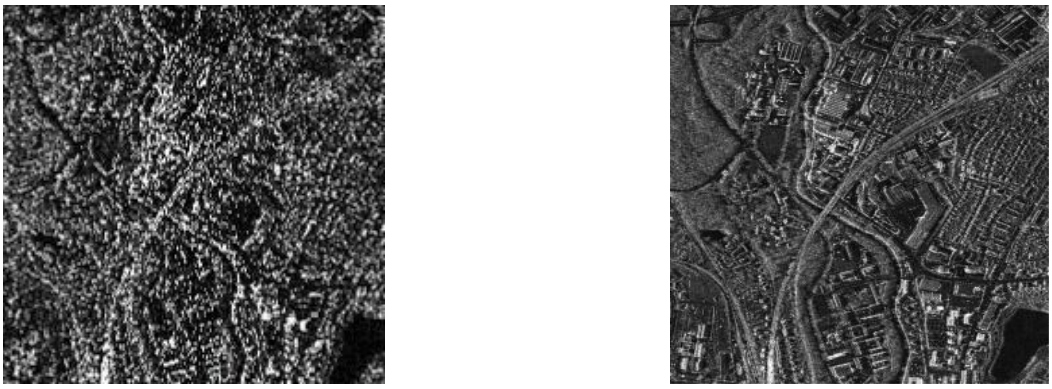

(a) (b)

Figure 2.4: SAR images from TerraSAR-X sensor acquired over the Luneburg urban area (Germany): (a) MR image (simulated); and (b) VHR image.

MR SAR data.
Moreover, the geometrical distortions and the presence of specular contributions becomes strongly present in VHR SAR images, in particular for urban scenes, where the buildings scattering present a geometric composition of different regions associate to layover, double-bounce and shadow [146].

2.2 Unsupervised Change Detection in SAR imagery

Change detection aims at identifying changes of natural features by analyzing images acquired on the same scene at different times, typically with the same acquisition modalities. A preliminary processing stage is usually assumed for the data, including both radiometric and calibration of the single-time data and co-registration of the multi-temporal images on common geometry (i.e., coverage and pixel size). A denoising stage aims at reducing the speckle effect. CD strategies can tackle bi-temporal analysis [112; 17; 22; 4; 7; 127; 169; 224; 109; 4; 136; 192; 108], in which images are pre- and post-event, or time-series analysis, describing phenomena temporal evolution on a larger set of acquisitions [178; 199; 198; 68; 135; 46; 112; 37].
In the first instance, let us consider bi-temporal CD. In the literature, several methods involving SAR imagery for bi-temporal CD have been proposed. An overview of the principal methods is presented in Table 2.1. Some methods considered the information fusion from SAR and optical data [44; 63; 173; 213], or the integration with ancillary GIS-based data [94; 73; 207]. However, a large part of SAR CD approaches considers multi-temporal SAR information, with same sensors and same acquisition modalities (i.e., nominal incidence angle and geometrical resolution). These approaches are grouped into supervised,

semi-supervised and unsupervised approaches, depending on the amount of prior information describing the nature of the change (i.e., land-cover transition), that can be used for the training the detector. Supervised CD methods include post-classification comparison, in which single-time SAR images are classified with supervised approaches and the multi-temporal comparison of the classification maps generates the CD map (see Fig. 2.5) [174; 74]. The map represents possible transitions of land-cover classes. However, the accuracy of post-classification comparison methods is affected by that of both the single-time classification maps. An alternative supervised strategy considers the joint classification

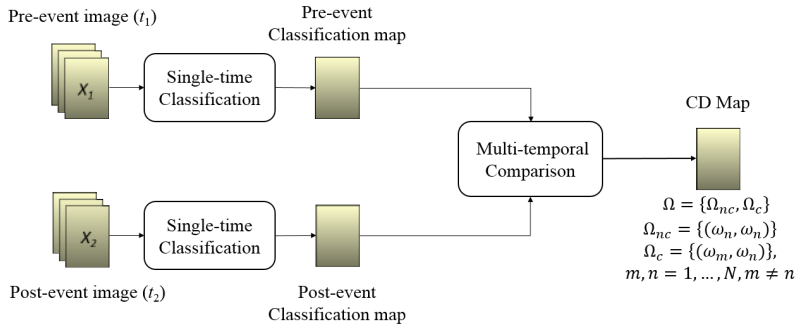

Figure 2.5: Block scheme for a CD approach based on post-classification comparison.

of the input multi-temporal images with deep neural networks [103]. However, supervised approaches suffer from the lack of large training data, so many applications tend to consider unsupervised CD approaches (see Fig. 2.6). Some approaches consider the joint image analysis with robust multi-dimensional clustering (i.e., Fuzzy c-means [8]). However, the presence of speckle and geometrical characteristics in SAR imagery affect

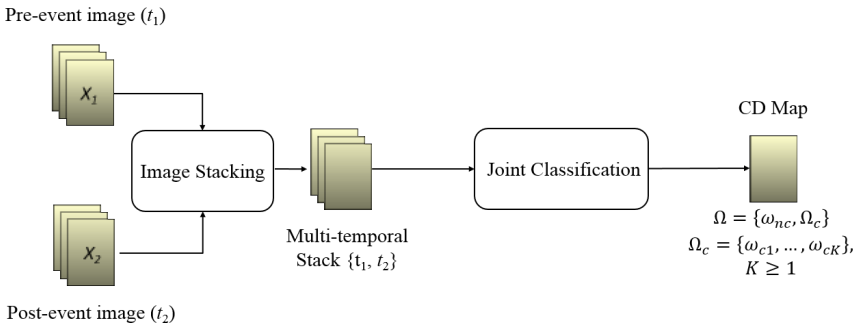

Figure 2.6: Block scheme for a CD approach based on joint analysis of the multi-temporal images.

the effectiveness of these approaches. This leads the preference to methods relying on: i) a comparison of the input bi-temporal images, generating a change index CI; and ii)the

extraction of the change information from the CI (see Fig. 2.7). Several strategies for

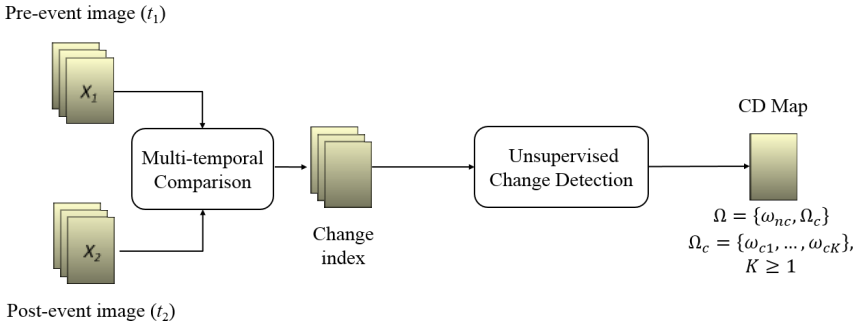

Figure 2.7: Block scheme for a CD approach based the multi-temporal comparison and the extraction of the change information.

the two steps have been proposed in the literature. More details for the two steps are illustrated in the subsections below.

2.2.1 Bi-temporal Comparison

Let X_1, X_2 be the two SAR images acquired on the same scene at times $t_1, t_2, t_1 < t_2$ and properly pre-processed. The multi-temporal comparison and the generation of CI can be performed either pixel- or context-based. Most of the pixel-based CI indices is defined with a ratio operator (e.g., ratio [156; 225], min-ratio [17; 5; 224], log-ratio [22; 24; 95; 33], Gauss-log-ratio [108]), in which intensity increase and decrease are mapped into values larger or smaller than 1, respectively. The effectiveness of this operation. compared to that of image differencing (popular for CD in optical images) is motivated by the statistical model of the single-time images X_1, X_2. By assuming a model in Eq. 2.7 for both images, and defining $X_r = X_2/X_1$ and $X_d = X_2 - X_1$ as the image ratio and difference CIs, respectively, the two corresponding pdfs would result:

$$P(X_r) = \frac{(2L-1)!}{(L-1)!^2} \frac{X_r^{L-1} \bar{X_r}^L}{(X_r + \bar{X}_r)^{2L}} \tag{2.18}$$

$$P(X_d) = \frac{L^L}{(L-1)!} \frac{\exp\left(-\frac{LX_d}{\bar{X}_2}\right)}{(\bar{X}_1 + \bar{X}_2)^L} \sum_{j=0}^{L-1} \frac{j!(L-1+j)!}{(L-1-j)!} X_d^{L-1-j} \left[\frac{\bar{X}_1 \bar{X}_2}{L(\bar{X}_1 + \bar{X}_2)}\right]^j \tag{2.19}$$

The two expressions show how $p(X_r)$ depends on the ratio of the intensity means, while $p(X_d)$ depends on both the difference of the intensity means and the single-time intensity values. So, ratio-based operators highlight changes in the same ways for both high and low values, unlike the difference-based operators [182; 37]. The use of the log-scale for

ratio (i.e., log-ratio operator) gives a more symmetric contrast for the increase and decrease change and changes the residual speckle component into an additive contribution. Log-ratio maps scattering increase and decrease into values larger and smaller than 0, respectively. In binary change detection, a single class of intensity change is inferred by considering minimum/maximum ratio [17; 109] (or absolute value of log-ratio [108]).

$$x_{MR} = 1 - \min\left\{\frac{I_2}{I_1}, \frac{I_1}{I_2}\right\} \tag{2.20}$$

$$X_{GLR} = \left|\log \frac{X_2}{X_1}\right| \tag{2.21}$$

Ratio operation is exploited also in context-based strategies, using the intensity of the pixel neighborhood [93; 76; 198; 102; 229; 57; 100]. The use of context-based operators provides a suitable and robust detection for changes of large targets, as they detect changes in the mean value associated to the pixel neighborhood. For the same reason, they exhibit larger robustness to speckle presence. In turn, pixel-based indices are more suitable detectors in case of changes preserving the neighborhood mean information. Mean-ratio [93; 76] is one of the neighborhood-based operators, it is defined as the ratio of the intensity means computed in a local neighborhood.

$$X_{\mu R}(x) = \frac{\sum_{i\in N(x)} I_2(i)}{\sum_{i\in N(x)} I_1(i)} \tag{2.22}$$

being $N(x)$ the neighborhood of the pixel x. In [198], a robust mean ratio operator is defined with a non-local approach, in which the was taken by considering all the pixels j of the image, $j \neq x$ with weights expressed in terms of pixel ratio pdf.

$$X_i^{NLM}(x) = \sum_{j\neq i} \frac{1}{Z(x)} \exp(-\frac{d(x,j)^2}{h^2}) X_i(j) \tag{2.23}$$

being h a filtering parameter and $Z(i)$ a normalization constant. In [100], a linear combination of the pixel-based and context-based mean-ratio operators is defined as CI, taking into account both the single-pixel intensity values and the local neighobrhood information, with weights dependent on the scene heterogeneity.

$$X_{mixR} = \frac{\sigma(\bar{x})}{\mu(\bar{x})} \frac{\min(I_1(x), I_2(x))}{\max(I_1(x), I_2(x))} + \left(1 - \frac{\sigma(\bar{x})}{\mu(\bar{x})}\right) \frac{\sum_{i\in N(x)} \min(I_1(x), I_2(x))}{\sum_{i\in N(x)} \max(I_1(x), I_2(x))} \tag{2.24}$$

A different approach considers neighborhood for a local estimation of the image statistical properties for the single-time image and a statistical similarity measure defined as CI. One of the most popular similarity measure is represented by the Kullback-Leibler distance (KLD) [113].

$$KLD(X_1, X_2) = \frac{1}{2}\left(KL(X_1, X_2) + KL(X_2, X_1)\right) \tag{2.25}$$

$$KLD(X_1, X_2) = \int p_(X_1) \log \frac{p(X_1)}{p(X_2)} dX_1 \tag{2.26}$$

Parametric forms of the distance can be derived assuming single-time statistical models. In [113], a parametric expression of the KLD based on the Gamma distribution model has been proposed with Edgeworth-series approximation. Other similarity measures in the literature include the mutual information [7; 4; 7], Jeffrey divergence [233] and Jensen-Shannon distance [222]. Some works considered the use of image transformations for CD, which highlight the geometrical information of the SAR images. In particular, Stationary Wavelet Transform [5; 32; 70; 11], Non-Subsampled Contourlet Transform [108; 128] and Fast Discrete Curvelet Transform [190; 11] separate the approximation and the details information on different scale levels and orientation levels.
Minor approaches include a keypoints-based graph [169] and the comparison of single-time segmented SIFT images [214].

2.2.2 Change information extraction

Let be R the CI feature selected for the multi-temporal comparison. In the analysis of R for the unsupervised extraction of the change class, different strategies have been proposed in the literature, based on either clustering or definition of separating thresholds. Hard clustering, such as k-means [234; 127; 115] or mean-shift clustering [4; 7], and soft-clustering approaches such as the Fuzzy C-means [101; 102; 141; 191], have been proposed in the literature. K-means clustering considers the iterative minimization of the within-class sum of squares [80]. The assignment of the feature sample r to one of the K classes based on the minimum distance between the sample and the centroids. In the fuzzy C-means, the class assignment is based on fuzzy membership functions describing the effectiveness of the pixel assignment for each class. The separation of the P points into C classes is obtained with the iterative minimization process of the cost function J

$$J = \sum_{n=1}^{N} \sum_{k=1}^{K} u_{kn}^m d^2(y_n, c_k) \tag{2.27}$$

At each iteration, both the centroids c_k and the membership functions u_{kn} are updated as follows.

$$c_k = \frac{\sum_{n=1}^{N} u_{kn}^m y_n}{\sum_{n=1}^{N} u_{kn}^m} \tag{2.28}$$

$$u_{kn} = \left[\sum_{j=1}^{K} \frac{d^2(y_n, c_k)}{d^2(y_n, c_j)} \right]^{-\frac{1}{m-1}} \tag{2.29}$$

being $d(y_n, c_k) = \|y_n - c_k\|_2$. The mean-shift clustering is an iterative non-parametric procedure which estimates the continuous pdf by considering the local density over values t and using a Kernel smoothing function $K(s-t)$ decreasing with distance s [7]. A derivative of the Kernel function is used for estimating the point at the next iteration, until convergence The algorithm estimates the modes associated to the sample set.
For thresholding strategies, The normalized data distribution $p(r)$ is modeled as a mixture of K components associated to the K classes. Each class ω is defined with a prior probability $P(\omega)$ and marginal distribution $p(r|\omega)$. Without loss of generality, let us consider a binary CD problem, with two classes: no-change ω_{nc} and change ω_c separated with threshold value T.

$$p(r) = P(\omega_{nc})p(r|\omega_{nc}) + P(\omega_c)p(r|\omega_c) \tag{2.30}$$

The analysis can be extended to K classes (i.e, two change classes associated to intensity increase and decrease), with the definition of $K-1$ threshold values. Some thresholding approaches fix a false alarm probability P_{fa} [57]. A numerical estimation of the threshold T can be obtained, considering the integral expression of P_{fa} in terms of the probability density function $p(r)$.

$$P_{fa} = 1 - \int_{-\infty}^{t} p(r)dr \tag{2.31}$$

Automatic thresholding selection can be obtained based on the Bayesian theory, with equality of the class posterior probabilities, or the minimization of a class-dependent cost function. In Bayesian approaches [35; 32; 55; 24; 25; 197], the separating threshold is decided such that:

$$P(\omega_c)p(r|\omega_c) = P(\omega_{nc})p(r|\omega_{nc}) \tag{2.32}$$

Both prior probabilities and marginal distributions are estimated with Expectation Maximization (EM) algorithm, which iteratively estimates the mixture parameters giving the maximum likelihood estimation. Some thresholding approaches are based on the optimization of a histogram-based cost function $J(T)$(e.g., Kittler-Illingworth thresholding [113; 22; 23; 17] or its generalized version [157; 69])

$$J(T) = \sum_{l=L_{min}}^{L_{max}} h(r)c(r,T) \tag{2.33}$$

being $h(r)$ the histogram of r, L_{max}, L_{max} the minimum and maximum bin of $h(r)$ and $c(r,T)$ a function defined as:

$$c(r,T) = \begin{cases} -2\log P(\omega_u|r,T)) & r \leq T \\ -2\log P(\omega_c|r,T)) & r > T \end{cases} \tag{2.34}$$

For both the groups of automatic thresholding strategies, prior probabilities and marginal distributions are determined with Maximum Likelihood Estimation or, for more complex models, with Method of Log-Cumulants [157]. Several statistical models have been proposed for marginal distributions modeling log-ratio (i.e., Gaussian [24] and Generalized Gaussian [25], Generalized Gamma ratio [125]), SAR amplitude ratio (e.g, Log-normal [156; 17], Nakagami-ratio, Weibull-ratio [17; 224], Generalized Gaussian [17] or Generalized Gamma ratio [69]). Other approaches refined the model by introducing a dependence of the class prior probabilities on the spatial context. This was typically modeled as Hidden Markov Chain [51], a Markov Random Field [212; 219; 102; 24] or Conditional Random Field [125]. The estimation of the unknown terms and the context-based prior model is conducted with Simulated Annealing, Maximal Posterior Mode [51] or Iterated Conditional Mode [225]. Other approaches include active contours [56] and the fusion of change informaiton coming from multiple channels [157] or scale levels [32; 5; 113; 55].
For CD methodologies based on an automatic thresholding selection, the effectiveness of the selection assumes that change and no-change classes have a proper statistical representation. For input images with large size, as for the case of VHR SAR imagery, it is possible that the no-change class presents a sharply dominant part in the mixture. This would introduce errors in the automatic threshold selection. In order to overcome this effect, a split-based CD approach was introduced in [33]. The approach divides the CI into S rectangular split, each with size $S_R \times S_A$. For the k-th split, a measure of the internal change information is defined with pixel variance σ_k^2. Large variance values indicate the equivalent presence of change and no-change classes, while small variance values indicate that the no-change class has a dominant presence in the split. Let μ_{σ^2} and σ_{σ^2} be the mean and the standard deviation of the variance set $\sigma_k^2, k = 1, ..., S$. Threshold selection is finally applied on a subset of image splits with a larger class balance. The split set is composed based on the condition:

$$\sigma_k^2 \geq \mu_{\sigma^2} + B\sigma_{\sigma^2}, k = 1, ..., S \tag{2.35}$$

The split-based approach has been applied in the definition of CD approaches tailored for specific applications, such as the building damage assessment [146] or the port surveillance [39]. The approach was used in the development of both the unsupervised CD method for Full-pol SAR images presented in Chapter 4 and the unsupervised CD method for VHR SAR images presented in Chapter 6.
In [33; 5] the authors considered a scale-driven CD approach based the combination of the multi-temporal information at different scale, in order to preserve detail information and mitigate the presence of outliers in the final CD map. In the approach, X_{lr} is decomposed with a dyadic approach at different resolution scale levels. The result of the decomposition

is image set $X_{ms} = \{X_{lr}^0, X_{lr}^1, ..., X_{lr}^{N-1}\}$, where X_{lr}^n represents the log-ratio information at scale scale n, $n = 0, ..., N-1$ and X_{lr}^0 indicates the original image (i.e., $X_{lr}^0 = X_{lr}$). The decomposition was conducted with Two-Dimensional Stationary Wavelet Transform, which keeps the transform invariant to translation, by avoiding the decimation step (used in Discrete Wavelet Transform). Other approaches in the literature consider Laplacian pyramid decomposition [3].

The filtering process starts with the definition of $\{X_{lr}$ as approximation wavelet component of level $n = 0$. For each scale level n, a set of high-pass and low-pass filters is iteratively applied the approximation component. This generates a four components in the wavelet domain: a lower-resolution approximation component (i.e., $X_{lr}^{LL(n+1)}$) and three detail components for vertical (i.e., $X_{lr}^{LH(n+1)}$), horizontal (i.e., $X_{lr}^{HL(n+1)}$) and diagonal (i.e., $X_{lr}^{HH(n+1)}$) directions, respectively. The four components can be defined in terms of two-dimensional signal convolution as follows:

$$X_{lr}^{LL(n+1)}(i,j) = \sum_{p=0}^{D^n-1} l^n[p]\, l^n[q]\, X_{lr}^{LL(n)}(i+p, j+q) \tag{2.36}$$

$$X_{lr}^{LH(n+1)}(i,j) = \sum_{p=0}^{D^n-1} l^n[p]\, h^n[q]\, X_{lr}^{LL(n)}(i+p, j+q) \tag{2.37}$$

$$X_{lr}^{HL(n+1)}(i,j) = \sum_{p=0}^{D^n-1} h^n[p]\, l^n[q]\, X_{lr}^{LL(n)}(i+p, j+q) \tag{2.38}$$

$$X_{lr}^{HH(n+1)}(i,j) = \sum_{p=0}^{D^n-1} h^n[p]\, h^n[q]\, X_{lr}^{LL(n)}(i+p, j+q) \tag{2.39}$$

being D^n the length of the wavelet filters at scale n and l^n, h^n the impulse response of the low-pass and high-pass filters, respectively. The response for the high-pass filter is obtained by reversing the order of the coefficients and by changing the sign of the even-indexed coefficients. A Two-Dimensional Inverse Stationary Transform (2D-ISWT) is applied to the approximation components $X_{lr}^{LL(n)}, n = 0, ..., N-1$ for obtaining the multi-scale image set X_{ms}. In 2D-ISWT, a set of inverse filters $\left[l^{(k)}\right]^{-1}, k = 1, ..., n$ are applied for each approximation component $X_{lr}^{LL(n)}$. Inverse filter response $\left[l^{(k)}\right]^{-1}$ is defined such that:

$$\left[l^{(k)}\right]^{-1}(p) * \left[l^{(k)}\right](p) = \delta(p) \tag{2.40}$$

The multi-scale decomposition was used in the development of the unsupervised CD method for VHR SAR images presented in Chapter 6.

Table 2.1: Overview of the principal bi-temporal CD methods for MR-SAR imagery.

Multitemporal Input data	**Multitemporal comparison**	**Detection strategy**
Methods based on image comparison	Single-pixel ratio	Constant false alarm probability [57], Bayesian [198], KI thresholding[69; 225], K-means [115]
	Single-pixel min-ratio	KI thresholding [17; 156]
	Single-pixel log-ratio	Bayesian [24; 22; 32; 35; 125] KI thresholding [23; 25; 109]
	Single-pixel Gaussian log-ratio	K-means [108], Bayesian (Wang2016)
	Local-context-based mean ratio	Bayesian [76; 51], Fuzzy C-means [102]
	Nonlocal-context-based mean ratio	Manual thresholding [224], Bayesian [198]
	Mutual information	Mean shift clustering [7; 5; 4]
	Kullback-Leibler distance	KI thresholding [113]
	Jeffrey divergence	K-means [233]
	Jensen-Shannon distance	Bayesian with context [222]
	Gabor transform	K-means [127]
	Wavelet transform	Bayesian [5; 33; 54], Manual thresholding [70; 113], Active contours [56], Multiscale fusion [33; 113]
	Curvelet transform	Manual thresholding [190]
	Contourlet transform	K-means [128; 108]
	Keypoints-based graph	Manual thresholding [169]
Others		Information fusion SAR+GIS [94; 73; 207]
		Information fusion SAR+Optical [44; 63; 173; 213]
		SAR Post-classification comparison [174; 74]
		SAR Supervised joint classification [103]
		SAR Unsupervised joint classification [8]
		SIFT-based SAR segmentation+comparison [214]

2.3 Unsupervised Change Detection in PolSAR imagery

If we consider Polarimetric SAR imagery, a large effort has been devoted to binary CD. In particular, many approaches in the literature defined the CD problem as hypothesis test, where the two hypotheses H_0 and H_1 were associated to the change and no-change class. The hypothesis test was typically evaluated with a similarity measure and a threshold value defined by fixing a desired false alarm probability. The approaches considered either Likelihood (or Generalized Likelihood) ratio test [163; 117; 52; 67; 162; 19], complex-kind Hotelling-Lawley trace [6], mutual information [82], feature-space geometrical distances [180; 58] and statistical distances [161; 81; 58].
Likelihood ratio tests the goodness of fit of the statistical model of the two multi-temporal images. For Wishart distribution, the test evaluates the equality of the two covariance matrices in terms of likelihood, with hypotheses $\Sigma_1 \neq \Sigma_2$ and $\Sigma_1 = \Sigma_2 = \Sigma$ associated to change ad no-change, respectively.

$$LLR = \frac{L(\Sigma)}{L(\Sigma_1)L(\Sigma_2)} = \frac{(n+m)^{(n+m)p}}{n^{pn}m^{pm}} \frac{|C_1|^n |C_2|^n}{|C_1 + C_2|^{n+m}} \tag{2.41}$$

being $L(\Sigma)$ the model likelihood, n, m the number of looks of C_1 and C_2, respectively. Based on the logarithmic form of LLR, Symmetrical Revised Wishart distance and Bartlett distance have been proposed [230].

$$d_W(C_1, C_2) = \frac{1}{2}\left(\log|C_1| + \log|C_2| + tr(C_1^{-1}C_2 + C_2^{-1}C_1)\right) \tag{2.42}$$

Most of the approaches were based on the assumption of homogeneous areas for the two multi-temporal images. A hypothesis Log-Likelihood test for heterogeneous data was proposed in [152]. A multi-variate version of the Kullback-Leibler divergence has been proposed for polarimetric SAR data in [81; 161], given the assumption of Wishart distribution for the two single-time polarimetric covariances C_1, C_2.

$$KLD(C_1, C_2) = \frac{1}{2}\left(KL(C_1, C_2) + KLD(C_2, C_1)\right) \tag{2.43}$$

$$KL(C_1, C_2) = \frac{1}{2}\int_{Supp(C)} p(C_1)\log\frac{p(C_1)}{p(C_2)}dC = \frac{1}{2}\log\left(\frac{|\Sigma_2|^n}{|\Sigma_1|^n}\right) + Ltr(\Sigma_2^{-1}\Sigma_1 - I) \tag{2.44}$$

For the computation of the entropy-based test, an entropy measure $H(C_i)$ is defined for the covariance matrix $C_i, i = 1, 2$. For large number of looks L, the entropy difference considering the true and the estimated distribution tends to be a Gaussian with variance σ_H^2. The entropy-based test [161] compares the entropy associated to the two multi-temporal images, with an index:

$$S_H\{C_1, C_2\} = L\frac{|H(C_1) - H(C_2)|^2}{\sigma_H^2(C_1) + \sigma_H^2(C_2)} \tag{2.45}$$

Popular entropy measures considered in the state of the art are Shannon H_S and Renyi entropy with order β H_R.

$$H_S = -\int p_C(C,\Sigma,L)\log p_C(C,\Sigma,L)dC \tag{2.46}$$

$$H_R = (1-\beta)^{-1}\log\int p_C^{\beta}(C,\Sigma,L)dC \tag{2.47}$$

In [180], the authors considered a transformation of the complex Covariance matrix C into a real-value Kennaugh matrix K [122] and the computation of geodesic distance between the target Kennaugh matrix and Kennaugh matrix associated to elementary targets. Geodesic distance GD between two Kennaugh matrices K_1, K_2 is given by

$$GD(K_1,K_2) = \cos^{-1}\left(\frac{tr(K_1^{-1}K_2)}{\sqrt{tr(K_1^{-1}K_1)}\sqrt{tr(K_2^{-1}K_2)}}\right) \tag{2.48}$$

A PCA-based K-means clustering was applied for detecting the change class. Automatic thresholding approaches (e.g., Kittler-Illingworth thresholding) for the aforementioned similarity measure were proposed in [134; 223; 96].
Other approaches are based on the definition of curvelet-based features from multiple polarimetric channels [189; 43], the optimization of contrast measures [71; 147; 148; 149; 176]), the fusion of change detection maps obtained by multiple SAR features [157], or the thresholding of multi-temporal features from state-of-the-art polarimetric decompositions [196; 121; 61; 62; 193].An overview of the principal PolSAR-based CD methods is reported in Table **??**. A large part of these methods tackled the CD as a binary problem, measuring a single change class. A poor effort has been devoted in the separation of change classes, with thresholding of cross-correlation coefficients derived after polarization state conformation [176] or the thresholding of decomposition features, following the paradigm for the single-pol SAR images [167].

2.4 Unsupervised Change Detection in VHR SAR imagery

The peculiarities illustrated above for VHR SAR data make the CD approaches for MR SAR data not much effective, requiring some modifications. Thus, some dedicated CD strategies were proposed in the literature for the analysis of VHR SAR data. In [5; 4; 7], CD considers the bivariate analysis of the pair of VHR SAR images. Mean-shift clustering is applied on multi-temporal data scatterplot and modes of the bivariate distributions are derived. Changes are associated to modes distant from the scatterplot diagonal.
In [31], a wavelet decomposition is applied to the single-time VHR SAR images. Approximation and detail coefficients for the two images are grouped into a feature vector,

Table 2.2: Overview of the principal bi-temporal CD methods for Polarimetric SAR imagery.

CD strategy	**Reference**
(Generalized) Likelihood Ratio	[52; 67]
Hotelling-Lawley trace	[6; 96]
Mutual Informaiton	[82]
Geometrical distances	[180; 58]
Statistical distances	[81; 161]
Curvelet transform	[189; 43]
Optimization of contrast features	[148; 149; 176]
Decomposition features thresholding	[196; 121; 62]
Multi-channel CD fusion	[157]

modeled as a multi-variate Gaussian. Pairwise components are compared with Kullback-Leibler divergence and a total sum of the different contributions is defined as CI.
In [190], multi-temporal comparison of the two images is applied on the Curvelet-transformed images and soft thresholding applied. Curvelet transform is exploited in a unsupervised strategy for the detection of building damages [42]. Their use on the pre-event image allows the detection of candidates associated to double-bounce and the integration of this information with the multi-temporal CI.
In [21], a local estimation of the statistical properties of both the single-time images is performed, by considering complex coherent SAR data. A complex Gaussian model is assumed for each single-time image, with a Markovian model for taking into account the pixel context. Unknown model parameters are retrieved with EM algorithm. A similarity measure of the two single-time image models, expressed in terms of the Kolmogorov-Smirnov test, is used for producing the CD map.
A robust CD approach based on the multi-scale representation of the Jensen-Shannon divergence has been proposed in [222]. In this approach, Jensen-Shannon divergence is computed on multi-scale components of the single-time VHR SAR images. The multiple similarity measures are modeled as a hierarchical MRF, so an estimation of the marginal posterior model is used for generating the final CD map.
Because of the very high resolution, the single pixel may not convey enough information and pixel- and context-based methods may not be very efficient in tackling the multi-temporal analysis for heterogeneous scenes. Thus, object-based CD methods were developed for the analysis of multi-temporal VHR SAR data [136; 226; 111; 98]. The

methods consider a preliminary segmentation of the single-time images and a comparison and change information extraction on the segmented single-time images. Some approaches consider the segmentation on the single-time image with region growing **??**. Here, the two segmented maps are compared for generating a preliminary change extent. This information is exploited in a pixel-based multi-temporal comparison of the VHR SAR images for refining the final CD map.

Two CD approaches, tailored for maritime surveillance [39] or monitoring of built-up areas [146], are based on a different object-based strategy. This considers a pixel-based CD and the extraction of objects from the single-time images obtained for an optimal scale level, depending on the characteristics of investigated targets. The objects are derived with window-based detectors and a multi-temporal comparison of the objects is conducted with statistical similarity measures.

Other approaches consider the segmentation on the change index. In [136], the two single-time images are compared and thresholded. Region growing was applied on pixels showing a large multi-temporal variation, until convergence. A connected component analysis was conducted on the resulting multi-temporal objects for deriving the final CD map.

In [77], the two VHR SAR images are directly compared for the derivation of a pixel-based CD map. Then, then an object-based analysis is conducted on the CI, by applying morphological component analysis with wavelet and curvelet transform, yielding a object-based CD map. The two CD maps are finally combined into a global CD map.

Chapter 3

A Novel Framework for Unsupervised Multi-class Change Detection in Dual-pol Intensity SAR Images

In the recent years, Polarimetric SAR (PolSAR) systems became a suitable tool for multi-temporal monitoring, with regular acquisitions in different polarimetric channels. Change Detection (CD) methods in polarimetric data mainly focus on binary change detection, whereas the polarimetric information provides features that can be exploited for separating multiple kinds of change. In this contribution, we introduce a novel model for the characterization of multi-temporal changes in bi-temporal dual-polarimetric data. The model is based on the novel definition of a polarimetric change vector (PCV), which separates kinds of change in terms of target properties of the two considered scenes, according to the scattering theory. The proposed model is used to design an unsupervised CD strategy that discriminates the multiple kinds of change classes. Experimental results conducted on three multi-temporal PolSAR datasets with different complexity in terms of number and kinds of change classes confirm the effectiveness of the approach and the better performance with respect to the state of the art. [1] [2]

[1]The candidate would thank Dr. Shane Cloude for his precious comments in the analysis of the single-time backscattering behavior.

[2]Part of this chapter appears in [171].

3.1 Introduction

The temporal monitoring of the Earth is a crucial topic for several applications. Some applications consider the analysis of long-time series for studying the impact of climatic events at large time scale[118]. Others focus on the impact of abrupt changes and require a steady monitoring of the area, such as in the case of disaster management [61; 167; 171]. In this context, Change Detection (CD) is defined as the process of identifying changes by means of the analysis of images acquired at different times over the same geographical area. For CD, spaceborne Synthetic Aperture Radar (SAR) imagery represents a powerful tool, as the acquisition of these data is not affected by the cloud coverage and the sun illumination. These properties increase the amount of useful regular acquisitions that can be considered on the scene compared to passive sensors, especially in extremely cloudy areas.

SAR systems provide a measure of backscattering information of the scene, by transmitting and receiving with linear polarization (i.e., H or V) [143]. The interpretation of this information is a complex task, as SAR imagery is characterized by geometrical distortions and multiplicative speckle noise. Geometrical distortions are given by the squinted geometry of acquisition over non-flat targets (e.g., mountains or built-up areas). Speckle is due to the coherent sum at the receiver of the signals returned by the multiple elementary scatterers in the SAR resolution cell.

Because of the properties of the SAR data, target discrimination in either single-time or multi-temporal analysis requires appropriate methodologies. In the literature, several CD approaches based on SAR data have been presented. Some of them are based on the multi-temporal comparison of the classification maps generated from the single-time SAR images (i.e., post-classification comparison methods [16]). However, a large part of the state-of-the-art approaches are based on the comparison of multi-temporal SAR images and the unsupervised information extraction from the resulting Change Index (CI). The CI can be derived on either a pixel-by-pixel basis or by exploiting the spatial context information. The latter option mitigates the effects of the speckle noise on the results.

Several comparison operators have been proposed for the generation of the CI and can be selected on the basis of the kind of data and their statistics. In SAR data, by areas with uniform texture, pixel intensity is modeled with an exponential probability density function and the noise is modeled as being multiplicative. These elements support the use of ratio-based comparison operators [184], including normalized-mean ratio [4; 17], log-ratio [143; 157; 22; 146] or Gauss log-ratio [108]. The representation in the logarithmic scale has the double effect of transforming the residual noise in an additive contribution and enhancing ratio values smaller than 1, which corresponds to backscattering decrease.

Other approaches are based on distance measures (i.e., Kullback-Leibler distance [113]) or features coming from the Information Theory (e.g., Mutual Information [44]), and take advantage of neighborhood information.
The aforementioned approaches mostly rely on the use of single polarimetric channels. Because of this, they often end up with identifying presence/absence of changes or in the best case they distinguish no-change from backscattering increase and decrease only. Nevertheless, the backscattering variation in single polarimetric data provides only a limited information about the nature of the kind of change, so that a multi-class change detection is not feasible or limited to the detection of backscattering increase and decrease. In this context, Polarimetric SAR (PolSAR) sensors extend the SAR imaging capabilities by transmitting and/or receiving on more polarizations [122], thus providing a more powerful tool for multi-class CD. Two types of polarimetric data are available, namely full-polarimetric (full-pol) and dual-polarimetric (dual-pol). In full-pol data, all the combinations are exploited, by transmitting and receiving on the two alternate polarizations (H and V). In dual-pol data, only two of the combinations are taken. In some cases, the two combinations are related to a fixed transmitting polarization (i.e., $HH - HV$ or $VV - VH$). In others, only co-polarizations (i.e., $HH - VV$) are considered. For simple targets, PolSAR data are usually expressed in terms of the scattering matrix S [122]:

$$S = \begin{bmatrix} S_{hh} & S_{hv} \\ S_{vh} & S_{vv} \end{bmatrix} \tag{3.1}$$

where S_{pq} is the complex scattering coefficient for the pq- polarimetric channel. In case of targets with complex spatial structure, the characterization is demanded to second-order statistics, with the definition of a polarimetric covariance matrix C:

$$C = e^{\dagger}e = \begin{bmatrix} C_{11} & C_{12} & C_{13} \\ C_{21} & C_{22} & C_{33} \\ C_{31} & C_{32} & C_{33} \end{bmatrix} \tag{3.2}$$

being $e = \begin{bmatrix} S_{hh} & S_{hv} & S_{vv} \end{bmatrix}$ the scattering vector and $(\cdot)^{\dagger}$ the hermitian operator. Diagonal elements of C are associated to the scattering intensity for the different polarimetric channels. Same information can be represented by the Coherency T through a change of basis as well. Advanced polarimetric decompositions of this matrix provide features effectively enhancing the polarimetric information [122; 167]. For full-pol data, both S and C have all non-zero elements. For dual-pol data, one of the elements of S is set to zero, while a subset vector e with the two non-zero elements is used for the definition of C [122]. In this chapter, we focus on the use of dual-pol intensity data with fixed

transmitting polarization.
CD applications exploiting polarimetric data are typically based on likelihood ratio tests [67; 122], the fusion of change maps obtained by single polarimetric features [122] or the descriptive analysis of the features coming from the polarimetric decompositions [43; 122; 143; 157; 167]. However, to the best of our knowledge, the aforementioned CD approaches aim at performing binary CD (i.e., they identify presence/absence of change without considering that changes may have different causes and thus semantic); sometimes they separate among increase and decrease of the backscattering in single polarimetric channel, but none of them aims at distinguishing among several possible multitemporal backscattering mechanism associated to different kinds of change on the ground [167]. Nevertheless, the information from polarimetric channels suggests the possibility of separating more than one or two kinds of change and of providing hints about their semantic meaning, leading to a multi-class CD. Unsupervised multi-class CD has been tackled in multi-temporal optical images, with the definition of multidimensional change index and proper techniques for the information visualization and thresholding [38; 133]. However, the difference between optical and PolSAR data in terms of both available channels (spectral and polarimetric, respectively) and data statistics makes the optical-based methods from the literature not applicable [183]. A first attempt to jointly use more polarimetric channels for multi-class change detection has been done by the authors in [171] only recently. Thus, more effort is required to fully take advantage of the polarimetric channels information for the discrimination of multiple (i.e., more than two) change classes.
In this chapter, we propose a framework for the representation and the discrimination of change classes based on a model of the multi-temporal behavior of dual-pol SAR backscattering information, which is inspired by [171]. These changes are mapped into specific regions of the space of the polarimetric change vectors and their physical meaning is analyzed according to their impact on the backscattering. We also propose an unsupervised CD strategy which exploits the proposed model for separating the no-change class and discriminating the different kinds of change. The strategy is proposed for medium/high resolution SAR images, so that samples can be assumed as independent and identically distributed. An automatic estimation of the optimal number of change classes is obtained by the use of a state-of-the-art model selection criterion (i.e., Bayesian Information Criterion). The capability of the proposed method to identify multi-class changes becomes highly interesting due to the growing offer of polarimetric data in public archives, in particular for the analysis of the dual-pol data, which are freely available in Sentinel-1 data archive [205].
The chapter is structured into five sections. Sec. 3.2 illustrates the proposed CD polarimetric framework and describes the behavior of the change and no-change classes. Sec.

3.3 presents a novel unsupervised CD strategy for complex PolSAR data, based on the proposed framework. Sec. 3.4 presents datasets and experimental results. Finally, Sec. **??** draws the conclusions and illustrates future developments.

3.2 Intensity-based Polarimetric Change Vector Analysis

3.2.1 Polarimetric Change Vector

Let us consider two intensity dual-pol SAR images X_1, X_2 with size $M \times N$, acquired over the same scene at times $t_1, t_2 (t_1 < t_2)$, respectively. Let us assume that pre-processing step is applied to the pair of images (i.e., calibration, multilooking, geocoding and coregistration). By considering intensity data, off-diagonal elements of the matrix C are neglected, thus no correlation information is assumed between the two polarimetric channels. Each polarimetric image $X_i, (i = 1, 2)$ is modeled as a data-cube structure, in which the generic spatial location (x, y) is associated to a vector $X_i(x, y)(x = 1, ..., M, y = 1, ..., N)$, with two components. Let p be the fixed transmission polarization and q its orthogonal polarization. X_i is defined as follows:

$$X_i(x, y) = [X_i^{pp}(x, y), X_i^{pq}(x, y)], p, q \in \{H, V\}, p \neq q \tag{3.3}$$

where $X_i^{pp}(x, y), X_i^{pq}(x, y)$ are the backscattering coefficients measured for the pixel in position (x, y) of the i-th image on the co- and cross-polarimetric channels, respectively. Starting from the information in X_1 and X_2, a multi-temporal model can be derived for mapping multiple kinds of change based on their backscattering properties. The proposed model is based on a novel multi-polarimetric multi-temporal log-ratio comparison of the input images and on the subsequent representation of the multi-polarimetric multi-temporal information in the dual-pol log-ratio feature space. The novel comparison operator is a polarimetric version of the log-ratio:

$$X_{LR} = [X_{LR}^{pp}, X_{LR}^{pq}] \tag{3.4}$$

$$X_{LR}^{pp} = \log \frac{X_2^{pp}}{X_1^{pp}} \tag{3.5}$$

$$X_{LR}^{pq} = \log \frac{X_2^{pq}}{X_1^{pq}} \tag{3.6}$$

The output X_{LR} is named as Polarimetric Change Vector (PCV). Each PCV component refers to a polarimetric channel and thus codes different characteristics of the change information. Log-ratio components in the PCV have positive/negative values associated to increase/decrease of the SAR intensity in the corresponding polarimetric channel and,

thus, to different kinds of change. The PCVs span a two-dimensional orthonormal feature space. The information in this feature space can be represented in a two dimensional coordinate systems: the Cartesian one (given by the log-ratio values for the two polarimetric channels) or the polar one. The relationship between polar and Cartesian coordinates is given by:

$$\rho = \sqrt{(X_{LR}^{pp})^2 + (X_{LR}^{pq})^2}, \rho \geq 0 \tag{3.7}$$

$$\phi = \arctan \frac{X_{LR}^{pq}}{X_{LR}^{pp}}, \phi \in [0, 2\pi] \tag{3.8}$$

where ρ is the magnitude and ϕ is the direction of the PCV. No-change and change classes can be characterized according to their magnitude and direction properties. On the one hand, no-change class does not exhibit relevant backscattering variation in both the co- and cross-pol channels. Both the PCV elements assume values close to 0. Thus, ρ is expected to have values close to 0 as well. On the other hand, change classes are associated to significant backscattering variations (either positive or negative) in one or both the polarimetric channels, (i.e., one or both the conditions $X_1^{pp} \neq X_2^{pp}$ and $X_1^{pq} \neq X_2^{pq}$ are satisfied). Therefore, at least one of the two PCV elements is significantly different from zero. In these cases, magnitude values are in average higher than those of the no-change class.

Let ω_{nc} be the class of unchanged pixels. The complementary class Ω_c represents the macro-class of all the possible kinds of change. In the feature space, classes ω_{nc} and Ω_c can be separated with a magnitude threshold T_ρ, thus the corresponding loci, namely a circle C_{nc} and an annulus A_c, are defined as:

$$C_{nc} = \{\rho, \phi : 0 \leq \rho \leq T_\rho, 0 \leq \phi < 2\pi\} \tag{3.9}$$

$$A_c = \{\rho, \phi : \rho > T_\rho, 0 \leq \phi < 2\pi\} \tag{3.10}$$

Direction values are almost uniformly distributed and thus exist in the whole domain of ϕ. Therefore, the direction provides no relevant information for the no-change class. Nevertheless, the direction can be used for discriminating among the change classes in the macro-class of changes Ω_c, as it assumes different values according to the effects of changes on the physical parameters of the scene. Different change classes assume positive, null or negative values for each PCV element. They correspond to different possible direction values in the PCV polar domain. For the sake of simplicity, we assume eight possible preferred direction values. The first four directions $\phi \in \{\frac{\pi}{4}, \frac{3\pi}{4}, \frac{5\pi}{4} \frac{7\pi}{4}\}$ correspond to the cases in which the absolute values of the two PCV elements X_{LR}^{pp} and X_{LR}^{pq} are similar to each other. The second set of directions $\phi \in \{0, \frac{\pi}{2}, \pi, \frac{3\pi}{2}\}$ includes the cases in which the absolute value of one component is stronger than the other. Each kind of change

can be mapped into a region of the PCV feature space surrounding its specific preferred direction. Let $\omega_{ck}, k = 1, ..., 8$ be the k-th change class, where:

$$\Omega_c = \bigcup_{k=1}^{8} \omega_{ck} \tag{3.11}$$

Each class ω_{ck} is mapped into an annular sector S_k having magnitude greater than T_ρ and limited by the thresholds $T_{k1}^{\phi}, T_{k2}^{\phi}$ along the direction. The first sector presents a discontinuity for $\phi = 0$. This discontinuity makes the sector S_1 as the union of two intervals defined by thresholds T_{11}, T_{12}

$$S_k = \{\rho, \phi : \rho > T_\rho, T_{k1}^{\phi} \leq \phi < T_{k2}^{\phi}, T_{k1}^{\phi} \leq T_{k2}^{\phi}\}, k \neq 1 \tag{3.12}$$

$$S_1 = \{\rho, \phi : \rho > T_\rho, 0 \leq \phi < T_{12}^{\phi}, T_{11}^{\phi} < \phi < 2\pi, T_{11}^{\phi} \geq T_{12}^{\phi}\} \tag{3.13}$$

Despite the sensitivity of the backscattering to a large set of physical variables, three main variables are individuated that characterize land-cover backscattering, namely the local roughness, the water content and the presence of targets with non-zero height. Such parameters can be used for the definition of a qualitative model of the backscattering information for both X_1 and X_2. Changes on the ground induce change-dependent variations on those physical parameters. Therefore, these can be used to model the behaviors of different kinds of change. Accordingly, Sec. 3.2.2 recalls single-date backscattering behavior for some targets, while Sec. 3.2.3 derives the multi-temporal polarimetric behavior in case of change.

3.2.2 Single date backscattering behavior

In order to model the physical changes in terms of backscattering variation on both co-pol and cross-pol channel, let us first analyze the sensitivity of the backscattering with respect to the parameters of both the sensor and the target. Among them, we examine the polarimetric channel and the frequency band as sensor parameters. However, an extended backscattering analysis is out of the purpose of this work and further details can be found [208; 209].

Polarimetric channels show different sensitivity to targets with different structure based on the scattering theory. Among the co-pol channels, the VV channel is more sensitive to the horizontal elements, while the HH is more sensitive to vertical structures with dihedral elements. The cross-polarimetric channel VH highlights the presence of depolarizing elements [220].

The selection of the frequency band on the SAR system highlights different scene layers,

as it affects the value of both the surface penetration depth (together with the dielectric constant) and roughness directly [218; 209]. Systems with lower frequencies (i.e., P- and L-band systems) are able to penetrate and detect targets on deeper layers, with high co-pol scattering, while at higher frequencies (i.e., C- and X-band systems) they sense information on the shallower layers [29; 110; 50]. The information of the deeper layers may be seen as cross-polarized signal because of the depolarizing effect of the target internal structure.

Sensor parameters can be assumed to be stable for different acquisitions, such that backscattering variations can be defined in terms of the target parameters only. They include the dielectric constant, the surface roughness, the local incidence angle, the aspect angle and the presence of dihedral elements.

The dielectric constant, associated to the bio-physical properties of the target, affects both the penetration depth and the backscattering intensity. One of the elements impacting on natural target backscattering is the water content. Several studies illustrated how high values of moisture content and dielectric constant are associated to large backscattering values on all the polarimetric channels [164; 155].

Surface roughness is modeled by root-means-square height s (or facets slope statistical parameter β) and one or two scales, depending on its complexity [164; 106]. For smooth surfaces (i.e., low s values), scattering models show low values for both co- and cross-pol values (i.e., specular reflection). In particular, scattering intensities on the two co-pol channels show similar small values, while the cross-pol intensity tends to zero. Rough surfaces (i.e., large s values) with a single roughness scale, such as bare soils, show scattering based on a general Bragg model, with both co-pol and cross-pol non-null values [106]. Sea surface is typically characterized by two roughness scales, associated to capillary and gravity waves [47; 232]. Capillary waves have very small roughness scale, thus scattering, under Kirchoff approximation, presents low cross-pol values and sensible co-pol values. Gravity waves modulate the slope scale of the capillary waves and increase scattering on the co-pol channels only. An additional non-Bragg term on both the co-pol channels is introduced for very rough marine surfaces.

The target acquisition is also characterized by an aspect angle and a local incidence angle. The aspect angle plays an important role in the analysis of dihedral elements (e.g., built-up areas [220]). These targets generally show high scattering on co-pol channels, while cross-pol scattering depends on the target aspect angle and it is minimum for angles close to zero.

The local incidence angle has an impact on the target geometry in terms of both cell resolution and geometrical distortions for non-flat targets. In particular, large shadow and foreshortening effects are associated to large and small angle values, respectively. From

a radiometric perspective, under the assumption of lambertian surface, large values are associated to lower backscattering intensities [218].
The presence of dihedral elements in the sensed resolution cell introduces a deterministic scattering contribution, dependening on the target aspect angle. Such contribution generates high backscattering values on all the polarimetric channels (depending on the aspect angle) and mitigates the effect of the sum of the contributions from the other scattering elements in the resolution cell. This aspect is exploited in the detection of urban areas in SAR imagery [150], [167]. This single date backscattering analysis holds for each SAR image whatever the acquisition time.

3.2.3 Multi-temporal backscattering behavior: change model

Let us now extend the single date analysis to the multi-temporal case. If the scenario preserves the same characteristics in terms of the illustrated physical parameters (i.e., no change occurred), small backscattering variations for both the polarimetric channels, mainly attributable to the noise effects, are detected (i.e., $X_{LR}^{pp}, X_{LR}^{pq} \simeq 0$). On the other hand, if the scenario shows a change in one or more physical properties, relevant backscattering variations are detected on one or both the polarimetric channels, based on the considerations illustrated in the previous subsection. Physical changes generating similar backscattering variations in the two polarimetric channels are considered as being the same change class. In the following, variations in the target physical properties are analyzed and associated to backscattering behaviors in the PCV domain.
Changes in the dielectric constant: changes in the target dielectric constant are typically associated to a variation of the target water content. A positive variation is associated to a direction $\phi = \frac{\pi}{4}$, corresponding to a backscattering increase on both the polarimetric channels (i.e., $X_{LR}^{pp}, X_{LR}^{qq} > 0$); conversely, a decrease of the water content is associated to a decrease of backscattering value on both channels, with a corresponding direction $\phi = \frac{5\pi}{4}$. Positive variations of the water content are seen after rainfall events or water content variations like the ones due to irrigation. Negative variations happen in presence of seasonal aging and loss of biomass of the vegetation [151]. Snow is another example of target that may show significant changes in the dielectric constant due to water content. However, the effects on backscattering are more complex. The increase of the water content in snow is associated to both an increase of the dielectric constant and a variation of the layer penetration depth. This is because of the melting of the dry snow layer, that high backscattering on both the co- and cross-pol channels. Thus, the wetness increase of the snow is associated to a backscattering decrease on both the polarimetric channels (i.e., $X_{LR}^{pp}, X_{LR}^{pq} < 0$) [85; 168].
Change in the surface roughness: let us consider variations in the surface roughness (e.g.,

a bare soil or a water body). In case of soils, where roughness is at centimeter scale (i.e., much smaller than the image geometrical resolution), an increase of the roughness parameter is seen as backscattering increase on both the co-pol and cross-pol channels (i.e., $X_{LR}^{pp}, X_{LR}^{pq} > 0$). This change is associated to a preferred direction $\phi = \frac{\pi}{4}$ and may occur in presence of soil tillage [208]. Opposite variation of the soil roughness show negative scattering variations (i.e., $X_{LR}^{pp}, X_{LR}^{pq} < 0$) and are mapped on a direction $\phi = \frac{5\pi}{4}$. On the other hand, water surface is composed by capillary waves with very small roughness scale, modulated by waves with larger scale. This variation affects scattering mainly on the co-pol channel, with negligible effects on the cross-pol one (i.e., $X_{LR}^{pq} \simeq 0$). Positive and negative roughness variations are mapped into corresponding directions $\phi = 0$ (i.e., $X_{LR}^{pp} > 0$) and $\phi = \pi$ $X_{LR}^{pp} < 0$ of the polar domain, respectively. These changes may occur in presence of a variation of the sea swell or an oil spill, which univocally reduces the surface roughness [179].

Changes in the dihedral elements: they are associated to the change of the dihedral structures in the resolution cell and show a backscattering variation for both the polarimetric channels, with preferred directions $\phi = \frac{\pi}{4}$ or $\phi = \frac{5\pi}{4}$ for a dihedral target appearing or disappearing, respectively. The variation of the cross-pol one is less as the aspect angle decreases and becomes small in presence of targets with negligible aspect angle. As $X_{LR}^{pq} = 0$, the preferred direction for the two changes tend to $\phi = 0$ and $\phi = \pi$, respectively. These changes may occur for arrival of large targets on the sea (e.g., ships) [206] or the growth of large vegetation [107]. Variation of multiple target parameters may occur for complex changes and depends on collateral conditions.

Example of change in multiple target parameters - a flood event: a flood event may occur on either barely or largely vegetated soil. In the case of the barely vegetated soil, under the assumption of smooth water surface, the effect on the backscattering by the increase of the soil dielectric constant is overtaken by the decrease of the surface roughness. This generates a backscattering decrease on both the polarimetric channels (i.e., $X_{LR}^{pp}, X_{LR}^{pq} > 0$), with a corresponding preferred direction $\phi = \frac{5\pi}{4}$. On the other hand, in case of largely vegetated soil, the flooded scene presents some dihedral structures formed by the trees and the water surface. This results in no relevant backscattering variations on the co-polarimetric channel between the two acquisitions (i.e., $X_{LR}^{pp} = 0$) and a backscattering decrease on the cross-pol channels, respectively. The corresponding preferred direction resulting from the two backscattering variations results in $\phi = \frac{3\pi}{2}$. When the assumption of smooth water surface is not fulfilled (i.e., rough water surface), the backscattering variation on the co-pol channel takes into account a further backscattering increase associated to the increase of the surface roughness with respect to the case of smooth water surface.

Example of change in multiple target parameters - changes in built-up areas: the second

example of complex changes is associated to the presence is of built-up areas, which are characterized by dihedral structures with large backscattering. In particular, the construction of built-up areas on a bare soil is characterized by a backscattering increase on both the polarimetric channels (i.e., $X_{LR}^{pp}, X_{LR}^{pq} > 0$), due to the appearance of the dihedral structures. The two backscattering variations result in a preferred direction $\phi = \frac{\pi}{4}$. On the other hand, the construction on areas with either vegetation or debris (e.g., collapsed urban areas) is characterized by the same variation on the co-pol channel (i.e., $X_{LR}^{pp} > 0$) and a stable backscattering on the cross-pol channel (i.e., $X_{LR}^{pq} = 0$), with a preferred direction in $\phi = 0$. Conversely, destruction of built-up areas, as in presence of seismic events, is associated to a decrease of the scattering in the co-pol channel (i.e., $X_{LR}^{pq} < 0$). A relevant decrease on the cross-pol channel is also present when no debris exists on the post-event scene (i.e., $X_{LR}^{pq} < 0$). The behavior can be explained by the high values of cross-pol scattering associated to the vegetation, the debris and the oriented structure [61; 167; 228].

Example of change in multiple target parameters - changes of vegetated areas: the last example is represented by deforestation phenomena (e.g., wildfire or clear-cutting on dense vegetated areas). The effect of such phenomena is strongly dependent on the frequency band. For higher frequencies (i.e., C- or X-band), the radiation has the capability to penetrate the vegetation canopy. The removal of the canopy keeps the trunk vertical structures, which form dihedral elements with the ground. Such changes result in backscattering increase and decrease on the co-pol and cross-pol channels, respectively (i.e., $X_{LR}^{pp} > 0$, $X_{LR}^{pq} < 0$). The change is mapped into a preferred direction $\phi = \frac{7\pi}{4}$. If the trunk structure is cleared as well, the scattering is sensed from the bare soil below the vegetation. Thus, the co-pol scattering shows no relevant backscattering variation (i.e.,$X_{LR}^{pp} \simeq 0$), while the co-pol scattering decreases (i.e.,$X_{LR}^{pq} < 0$) [49; 50]. Such change is associated to a preferred direction $\phi = \frac{3\pi}{2}$. At lower frequencies (i.e., P- or L-band), the scattering return is mainly associated to the trunk structure. In this case, the removal of the tree structure is mapped into a preferred direction $\phi = \frac{3\pi}{2}$, corresponding to backscattering decrease in the co-pol channel and no relevant variation is sensed on the cross-pol one. No relevant scattering changes are sensed from the removal of the canopy. Changes due to the seasonal growth show opposite variations in the canopy and/or the trunk structure. Based on the aforementioned considerations, they are mapped into directions with supplementary angles with respect to those expressed for deforestation change.

A representation of the different changes described above in the PCV domain is illustrated in Fig. 3.1. The figure highlights the PCV capabilities in discriminating changes having different multi-temporal backscattering behavior on the different elements of the PCVs and thus how they assume different directions. Based on the considerations expressed

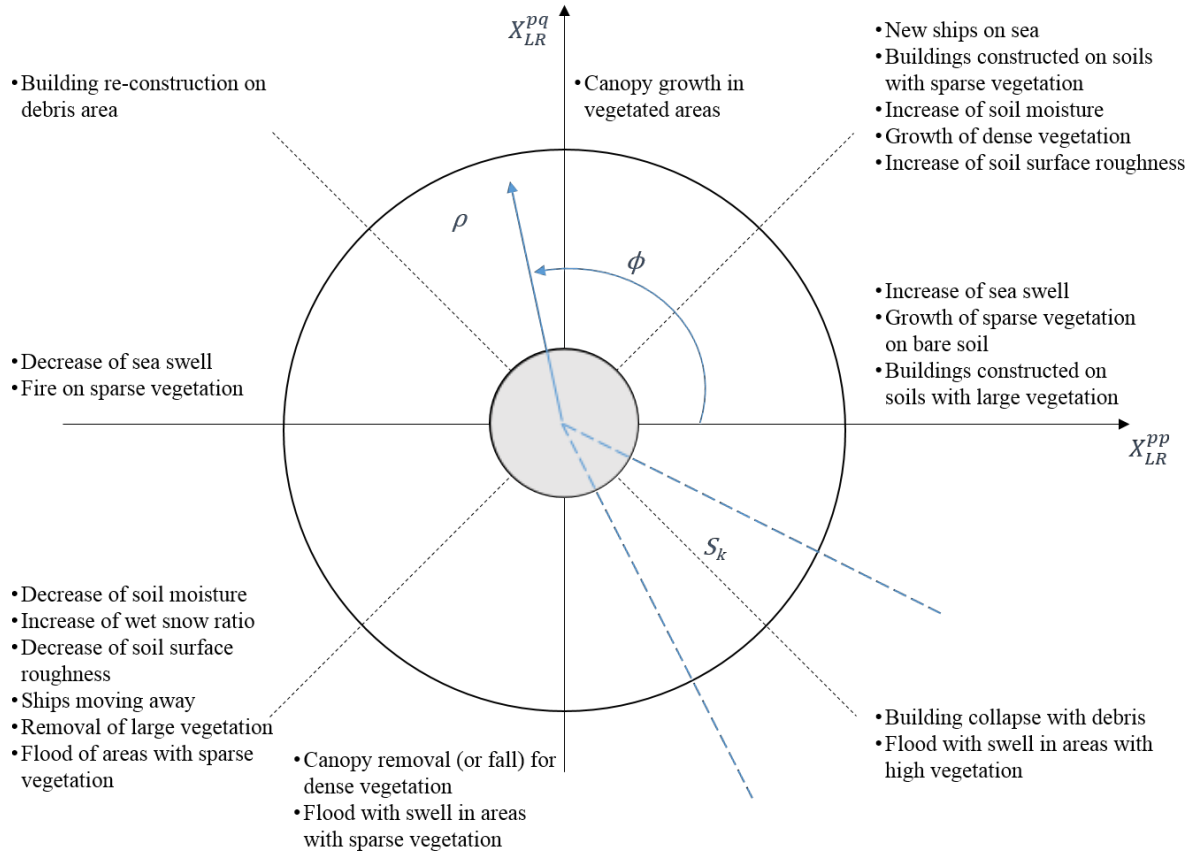

Figure 3.1: Change behavior in the PCV feature space.

above in terms of the physical target parameters, further changes may be characterized in terms of backscattering variation and represented in one of the sectors of the PCV feature space.

3.3 Proposed CD Approach in Dual-Pol SAR images

The model in Sec. 3.2 provides the main properties of the changed and unchanged pixels in the PCV feature space. No-change decision region can be bounded by a threshold value T_ρ, while each of the change classes ω_{ck} can be separated by two thresholds T_{k1}, T_{k2}. The interval defined by T_{k1} and T_{k2} includes the preferred direction associated to the change as described in the previous section and illustrated in Fig. 3.1. Nevertheless, in real SAR data the thresholds should be estimated by taking the noise effect into account and, thus, the behavior of the distribution of the magnitude and direction random variables in the PCV feature space. Moreover, without any prior knowledge, the number of change classes is unknown but typically smaller than the aforementioned 8 possible preferred directions.

Thus, let the expected number of change classes in a specific case be K, with $K \in [1, 8]$. In this section, we propose an automatic multi-class CD approach based on the model presented in Sec. 3.2. The approach is based on two steps : i) a binary CD performed along the magnitude variable, which aims at separating changed from unchanged samples (i.e., classes ω_{nc}, Ω_c); and ii) a multi-class CD performed along the PCV direction variable, which aims at separating $\omega_{ck}, k = 1...K$ from each other. Fig. 3.2 shows the block scheme of the proposed approach.

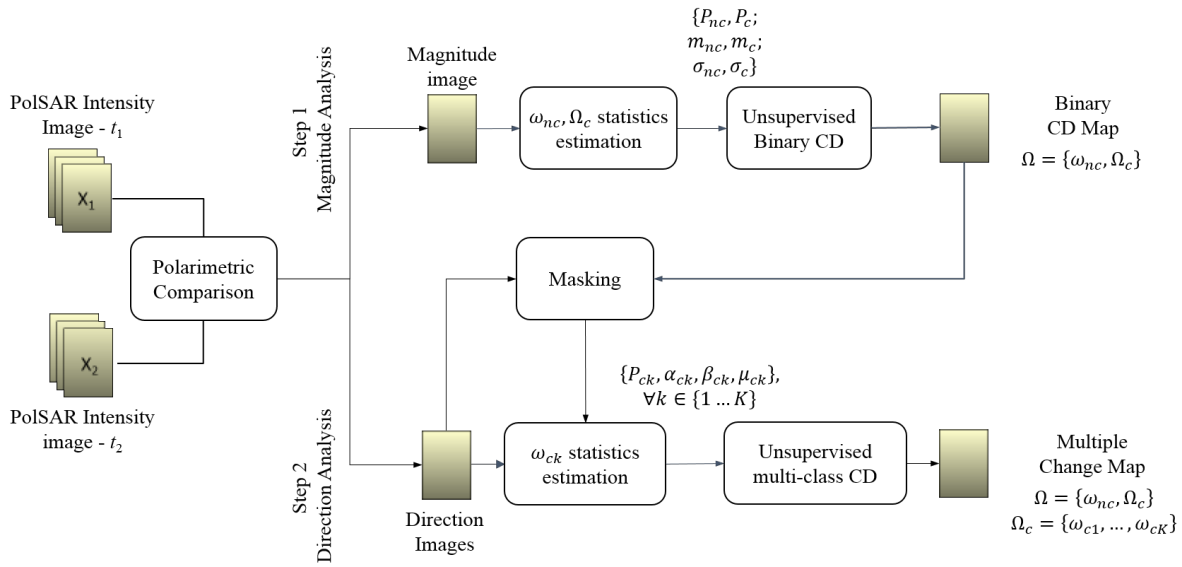

Figure 3.2: Block diagram of the change detection method.

3.3.1 Binary CD along the magnitude

The binary classification in the first step aims at separating the no-change class ω_{nc} from the macro-change class Ω_c. Several approaches have been presented in the literature to this end that consider either a single log-ratio feature [146] or spectral change vectors [145], derived from SAR or multi-spectral images, respectively. Some of them consider distance-based clustering (e.g., K-Means [234] or Fuzzy C-means [60]). Others, are based on the estimation of the threshold for class separation (e.g., Bayesian [171; 146; 158], Otsu [194], Kittler-Illingworth [22]). However, to the best of our knowledge, there is no attempt to use such approaches on polarimetric SAR data. In order to exploit the properties of the PCV magnitude and its statistical distribution for better class discrimination, here we consider the Bayesian approach since it results to be more robust and accurate when dealing with significantly overlapping classes. It requires an explicit estimation of class

probability-density functions. The unsupervised EM algorithm is employed to this end. The magnitude variable carries information about presence/absence of change, thus its probability density function is expressed as a mixture of two components associated to ω_{nc} and Ω_c.

$$p_\rho(\rho) = P(\omega_{nc})p_\rho(\rho|\omega_{nc}) + P(\Omega_c)p_\rho(\rho|\Omega_c) \tag{3.14}$$

being $P(\omega), p_\rho(\rho|\omega)$ the prior probability and the marginal distribution for the class ω, $\omega \in \{\omega_{nc}, \Omega_c\}$, respectively, with $P(\omega_{nc})+P(\Omega_c) = 1$. In order to set a statistical model for the marginal distribution of the magnitude, we consider the log-ratio features composing the magnitude. In the literature, empirical statistical models have been proposed modeling the single-polarimetric log-ratio as a mixture of Gaussian or Generalized Gaussian distributions [22; 171]. The model shows good trade-off between robustness and estimation accuracy. However, our analysis pointed out that the PCV magnitude presents a tailed distribution which is the result of the root square sum of the log-ratio variables. Thus, introduce a more flexible and generalized skewed model, widely employed in the SAR analysis, for the components of the PCV magnitude (i.e., Nakagami [17], Weibull or Generalized Rayleigh [156]). In this work, we assume the PCV magnitude modeled as a mixture of two Nakagami distributions, with priors $P(\omega_{nc}), P(\Omega_c)$ and class-conditional parameters $m_{nc}, \sigma_{nc}, m_c, \sigma_c$ for the no-change and change classes, respectively. The probability density function (pdf) of a single Nakagami distribution for the class ω, with general parameters m, σ, is defined as follows:

$$p(\rho|\omega) = \frac{2m^m}{\Gamma(m)s^m}\rho^{2m-1}e^{-m\rho^2/s} \tag{3.15}$$

By applying the EM algorithm, prior probabilities and parameters for the marginal distributions at $(q+1)$-th step are derived in order to maximize the current estimation of the log-likelihood function:

$$P^{(q+1)}(\omega) = \frac{\sum_{i=1}^{MN} p^{(q)}(\omega|\rho_i)}{MN} \tag{3.16}$$

$$s^{(q+1)}(\omega) = \frac{\sum_{i=1}^{MN} p^{(q)}(\omega|\rho_i)\rho_i^2}{\sum_{z=1}^{MN} p^{(q)}(\omega|\rho_i)} \tag{3.17}$$

$$\sum_{i=1}^{MN} p^{(q)}(\omega|\rho_i)\left[1 - \frac{\rho_i^2}{s^{(q)}} + \log\left(\frac{\rho_i^2}{s^{(q)}}\right) - \psi(m^{(q)}) + \log(m^{(q)})\right] = 0 \tag{3.18}$$

being $P^{(q)}, s^{(q)}, m^{(q)}$ the prior probability, the shape and the spread parameters for the class ω at the qth iteration, $\omega \in \{\omega_{nc}, \Omega_c\}$ and being $\psi(x) = \Gamma'(x)/\Gamma(x)$ the digamma function. The iterative process stops when either a maximum number of iterations is reached

or the log-likelihood value reaches the convergence condition (i.e., the log-likelihood variation between two consecutive steps is below a tolerance value). The EM algorithm presents a strong sensitivity to the initial conditions and does not guarantee the convergence to the global minimum. The most popular strategy to increase robustness is the selection of the initial values by K-means clustering [27]. From the clusters, an initial estimation of the statistical parameters of the two classes is derived. Bayesian decision rule is finally applied for assigning each sample to either ω_{nc} or Ω_c according to ρ value.

$$\omega = \arg\max_{\omega}\{P(\omega)p(\rho|\omega)\}, \omega \in \{\Omega_c, \omega_{nc}\} \tag{3.19}$$

The value which makes the two posterior probabilities equal is the magnitude threshold T_ρ:

$$P(\omega_{nc})p(\rho|\omega_{nc}) = P(\Omega_c)p(\rho|\Omega_c) \tag{3.20}$$

3.3.2 Multi-class CD along the direction

The second step of the proposed approach is the classification of the samples in Ω_c into multi-class changes, for the separation of the change classes $\{\omega_{c1}, ..., \omega_{cK}\}$. This is operated along the direction variable computed over the distribution of changed pixels $p(\phi|\Omega_c)$, which is estimated from the corresponding data histogram. $p(\phi|\Omega_c)$ is modeled as a mixture of K components, each associated to a specific change class ω_{ck}, with marginal distributions $p(\phi|\omega_{ck})$ and prior probabilities $P(\omega_{ck}), k = 1...K, \sum_{k=1}^{K} P(\omega_{ck}) = 1$.

$$p(\phi|\Omega_c) = \sum_{k=1}^{K} P(\omega_{ck})p(\phi|\omega_{ck}) \tag{3.21}$$

To the best of our knowledge, a poor effort has been devoted for deriving the statistical model of a direction feature both in passive and SAR data. In [34], a statistical non-uniform model has been proposed for the direction feature derived with optical passive data. The model is limited to the case of two non-zero mean Gaussian random variables. It shows a periodicity not present in empirical data distribution, due to a dependence on the random variable in terms of a tangent function, and introduces a large complexity that makes the unsupervised mixture estimation not attractive. Further the model derived for optical passive sensor data relies on assumptions that do not hold for PolSAR ones. In order to have a reliable and flexible model for the PCV direction, we propose to model the conditional distribution for each change class as a Generalized Gaussian function, characterized by three parameters: location μ_k, scale α_k and shape β_k.

$$p(\phi|\omega_{ck}) = \frac{\beta_k}{2\alpha_k\Gamma\left(\frac{1}{\beta_k}\right)} e^{-\left[\frac{|\phi-\mu_k|}{\alpha_k}\right]^{\beta_k}} \tag{3.22}$$

In the multi-class CD, no prior knowledge of K is assumed. Here we estimate its value by minimizing the Bayesian Information Criterion (BIC) over the discrete set of values $K^* < 8$. BIC is one of the state-of-the-art criteria for estimating the quality of model fitting to the data. It takes into account both the complexity of the data model (i.e., the number of free parameters) and the likelihood of the model with respect to the data. By considering (3.21) and (3.22), BIC minimization is as follows:

$$K = \arg\min_{K^* \leq 8} BIC(K^*) = \arg\min_{K^* \leq 8} (4K^* - 1)\log(card\{\Omega_c\}) - 2log(\hat{L}(K^*)) \tag{3.23}$$

where $\hat{L}(K^*)$ is the maximum Log-likelihood obtained by estimating a mixture of K^* components. For each possible K^*, the estimation of the statistical parameters is conducted by applying the iterative equations of the EM algorithm.

$$L^{(q)}(K^*) = \sum_{i=1}^{card\{\Omega_c\}} \log\left[\sum_{k=1}^{K^*} P^{(q)}(\omega_{ck}) p^{(q)}(\phi|\omega_{ck})\right] \tag{3.24}$$

$$P^{(q+1)}(\omega_{ck}) = \frac{\sum_{z=1}^{card\{\Omega_c\}} p^{(q)}(\omega_{ck}|\phi_z)}{card\{\Omega_c\}} \tag{3.25}$$

$$\alpha_k^{(q+1)} = \left[\frac{\beta_k^{(q)} \sum_{z=1}^{card\{\Omega_c\}} p^{(q)}(\omega_{ck}|\phi_z) \left|\phi_z - \mu_k^{(q)}\right|^{\beta_k^{(q)}}}{\sum_{z=1}^{card\{\Omega_c\}} p^{(q)}(\omega_{ck}|\phi_z)}\right]^{1/\beta_k^{(q)}} \tag{3.26}$$

$$\sum_{z=1}^{card\{\Omega_c\}} p^{(q)}(\omega_{ck}|\phi_z) \frac{\beta_k^{(q)}}{\left(\alpha_k^{(q)}\right)^{\beta_k^{(q+1)}}} \left|\phi_z - \mu_k^{(q+1)}\right|^{\beta_k^{(q)}-1} \cdot sign\left(\phi_z - \mu_k^{(q+1)}\right) = 0 \tag{3.27}$$

$$\sum_{z=1}^{card\{\Omega_c\}} p^{(q)}(\omega_{ck}|\phi_z) \left[\frac{1}{\beta_k^{(q+1)}} + \frac{\psi\left(\frac{1}{\beta_k^{(q+1)}}\right)}{\left(\beta_k^{(q+1)}\right)^2} - \left(\frac{\left|\phi_z - \mu_k^{(q)}\right|}{\alpha_k^{(q)}}\right)^{\beta_k^{(q+1)}} \log\left(\frac{\left|\phi_z - \mu_k^{(q)}\right|}{\alpha_k^{(q)}}\right)\right] = 0 \tag{3.28}$$

For each K^* value, the estimation process stops when the maximum number of iterations is reached or convergence condition for the likelihood is satisfied. The set of parameters that guarantees the minimum BIC according to the aforementioned definition, provides the best fitting solution and the optimal number of changes K. Starting from the estimated parameters, multi-class CD map is derived by assigning the class ω_{ck}^* to each considered sample z based on the Bayesian decision rule:

$$\omega_{ck}^* = \arg\max_k \{P(\omega_{ck}) p(\phi(z)|\omega_{ck})\} \tag{3.29}$$

From the posterior probabilities, it is possible to estimate the thresholds T^{ϕ}_{k1}, T^{ϕ}_{k2} for the class ω_{ck}, with $k \leq K$. T^{ϕ}_{K2} and T^{ϕ}_{11} are selected as the extrema of the histogram.

$$T^{\phi}_{k1} : P(\omega_{ck})p(\phi|\omega_{ck}) = P(\omega_{c(k-1)})p(\phi|\omega_{c(k-1)}) \tag{3.30}$$

$$T^{\phi}_{k2} : P(\omega_{ck})p(\phi|\omega_{ck}) = P(\omega_{c(k+1)})p(\phi|\omega_{c(k+1)}) \tag{3.31}$$

$$T^{\phi}_{k2} = T^{\phi}_{(k+1)1} \tag{3.32}$$

As for the magnitude, also for the direction variable other strategies can be used for threshold estimation like Otsu [194] and Kittler-Illingworth [22]. In real scenarios, some sectors of the polar domain may not show relevant population. Thus, the thresholds $T^{\phi}_{ki}, k \leq K, i = 1, 2$ will be different from the theoretical values defined in the previous Section.

3.4 Experimental Results

For the validation of the proposed CD approach, three bi-temporal datasets of dual-pol intensity SAR images have been considered, showing different numbers and kinds of change classes. Two datasets, acquired by the Sentinel-1 and UAVSAR sensors over the areas of Chennai (India) and Los Angeles (United States) respectively, show the presence of two ($K = 2$) relevant changes in the scene. The third dataset is more complex. It is acquired by the Sentinel-1 sensor over the area of Oristano (Italy) and is characterized by the presence of three changes ($K = 3$). An overview of the considered acquisitions is reported in Table 3.1.

In order to prove the effectiveness of the PCV information representation, two different thresholding approaches have been tested for both the PCV magnitude and direction. The first one applies Bayesian decision rule to class probability density functions estimated by the EM algorithm. The second one employs Otsu thresholding strategy. On all the datasets, BIC analysis was conducted for estimating the optimal K, by considering the analysis of a mixture of K^* generalized Gaussians, with K^* integer ranging in $[1, 8]$. Since, at best of our knowledge, no method exists for multi-change detection in PolSAR data, we compare the results of the proposed framework with: i) a standard binary CD method based on the Log-likelihood Ratio (LLR) of PolSAR data and on the assumption of Gamma statistical model for single-time intensity [67]; and ii) an unsupervised decision strategy applied to the 2-dimensional (2D) space of PCV. PCV class probability density function is modeled as a mixture of bivariate Gaussian components. Unknown parameters of the mixture are estimated with EM algorithm (EM2DGM). A prior knowledge of the number of classes in the mixture is injected, by assuming K being obtained by

Table 3.1: Overview of the multi-temporal acquisitions for the experimental results.

Dataset	Chennai	Los Angeles	Sardinia
Sensor	Sentinel-1	UAVSAR	Sentinel-1
Band	C	L	C
Polarimetric channels	VV-VH	HH-HV	VV-VH
Resolution	$20 \times 20m$	$3 \times 3m$	$20 \times 20m$
Acquisitions	Oct. 31, 2015 Nov. 12, 2015	Apr. 23, 2009 May 11, 2015	May 21, 2016 July 20, 2016

the proposed method. This favors the reference method in respect of the proposed one (that estimated K in an unsupervised way instead. Accuracy assessment for the considered approaches is performed in terms two popular indices, namely Overall Accuracy (OA) and Kappa coefficient ($Kappa$) [130; 86]. The former coefficient provides an overall measure of the correct classification without taking into account the prior probability of the classes. The second one takes into account the class priors. In the following, a more detailed description and the performance of the proposed approach are reported for each dataset.

3.4.1 Chennai dataset

The Chennai dataset includes two dual-pol SAR GRD-mode images acquired by the Sentinel-1 SAR sensor. Both images have a spatial resolution of 20×20 meters and data on VV co-pol and VH cross-pol channels. They have been acquired over the area of Chennai (India) in October 3, 2015 and November 12, 2015, respectively. During that period, the area has been hit by a flood which interested the rural areas of the region and, in minor part, the suburbs of the city. In order to proceed with the analysis, the two SAR images have been pre-processed, by applying radiometric calibration, co-registration and noise filtering [122].

A portion of 686×963 pixels has been considered for a quantitative analysis. Figures 3.3a and 3.3b show the multi-temporal false-color composition of the backscattering for the VV and VH polarimetric channels, respectively. The multi-temporal false-color composition is constructed such that: i) unchanged samples (showing stable backscattering values over time) appear in grey-scale shades, whereas ii) changed samples (that assume different backscattering values at the two dates) appear with green and magenta shades when

backscattering increased or decreased, respectively. A reference map has been generated starting from ground truth vectorial data from United Nations Institute for Training And Research (UNITAR) [2]. The reference map represents the changes of the water-bodies after the flood event (Fig. 3.7a) only. PCV with X_{LR}^{VV}, X_{LR}^{VH} components has been generated for each pixel. By representing the PCV in the polar coordinate system (Fig. 3.4), we can see that the flooded pixels tend to cluster in a sector with a preferred direction $\phi = \frac{5\pi}{4}$, as the presence of a new water body is associated to a sensible decrease of X_{LR}^{VV}. Regions where the water body disappeared tend to cluster along a preferred direction $\phi = \frac{\pi}{4}$, in agreement with the model in Sec. 3.2.
The EM estimation of the priors and marginal distributions of the classes ω_{nc} and Ω_c results in the PCV magnitude distribution illustrated in Fig. 3.5. Bayesian thresholding for separating ω_{nc} and Ω_c provides $T_\rho = 1.3$ dB. In order to estimate the optimal number of change classes, PCV direction distribution has been modeled as a mixture of K Generalized Gaussian distributions. Fig. 3.6a shows the plot of the BIC criterion with respect to the number of classes. The smallest BIC indicates an optimal value $K = 2$. The result is qualitatively confirmed by the trend of the direction pdf. The EM algorithm has been applied with $K = 2$ for the estimation of the priors and the marginal distribution parameters. Thresholds $T_{12} = T_{21} = -1.2$ radians has been estimated with the Bayesian decision rule. Fig. 3.6b shows the direction normalized histogram and the estimated class distributions. Fig. 3.7b shows the multi-class CD map. Otsu thresholding led to thresholds $T_\rho = 1.74dB$ for magnitude and $T_{12} = T_{21} = 2.06$ radians for the direction, respectively, leading to the map in Fig. 3.7c.
Good performance is achieved by the proposed method, with the correct detection of both the flooded areas around the lake and the strip of land where the water disappeared. A small amount of misclassification errors is related to false alarms occurring on the change class ω_{c2} with preferred direction $\phi = \frac{\pi}{4}$. These errors are associated to backscattering variations located on small urban areas (yellow circle in Fig. 3.7b), probably due to the rain causing the flood. A large amount of errors (in terms of both false alarms and missed detections) is associated to the change class ω_{c1} with preferred direction $\phi = \frac{5\pi}{4}$. False alarms (orange circle in Fig. 3.7b) are due to soil backscattering variations, which may be due to temporal variations of the surface roughness parameters, not reported in the water-body reference map. On the other hand, miss detections for the class ω_{c2} (green circle in Fig. 3.7a) may be partially explained by lower level of accuracy of the water-body boundaries in the pre-event map, which does not show the presence of all the small water regions.

For this data set, Otsu thresholding led to slightly better performance than Bayesian one (i.e., $OA = 0.9463$ and 0.9307 and $Kappa = 0.6910$ and 0.6668, respectively). This

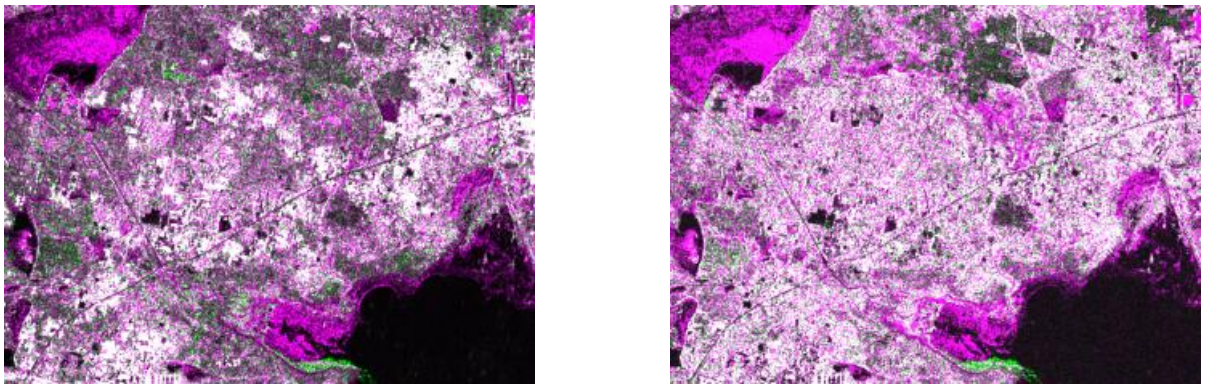

(a) (b)

Figure 3.3: Chennai dataset: multi-temporal backscattering false color composition for (a) VV Channel; (b) VH Channel. R, B: Oct. 2015; G: Nov. 2015. No-change appears in gray shades, backscattering increase and decrease in green and magenta, respectively.

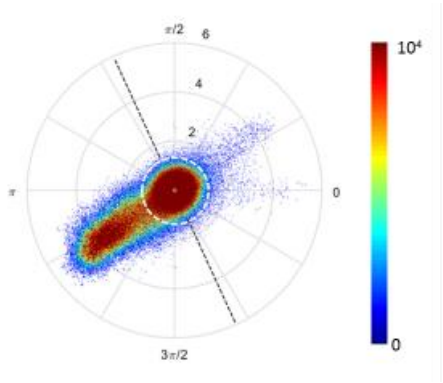

Figure 3.4: Chennai dataset: bivariate polar histogram (white dashed circle - T_ρ, black dashed line - T_{12}).

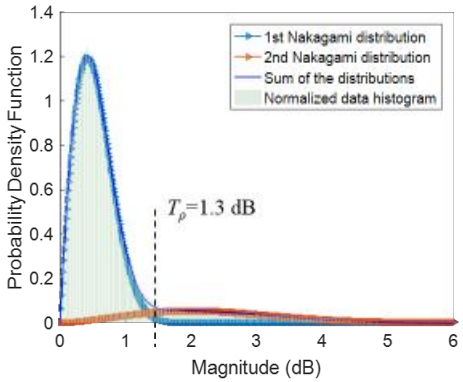

Figure 3.5: Chennai dataset: magnitude mixture model.

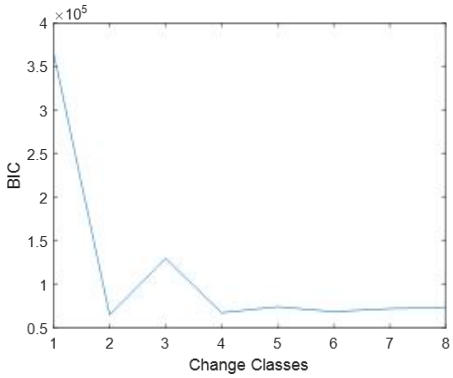

(a)

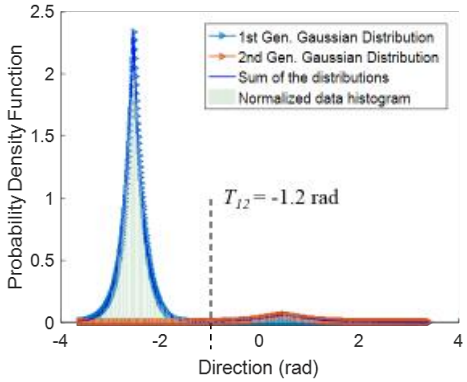

(b)

Figure 3.6: Chennai dataset: (a) BIC analysis with respect K (minimum value is reached for $K = 2$); (b) direction histogram and estimated mixture model for $K = 2$.

Table 3.2: Chennai dataset: confusion matrix, and overall accuracy (OA) for the proposed approach (Otsu Thresholding).

	$\hat{\omega}_{nc}$	$\hat{\omega}_{c1}$	$\hat{\omega}_{c2}$
ω_{nc}	574584	14105	1514
ω_{c1}	20291	47816	20
ω_{c2}	1545	26	717
		OA	0.9432

Table 3.3: Chennai dataset: performance comparison with state-of-the-art methods.

	Multi-class CD			Binary CD
Method	Proposed		EM2DGM	LLR
	Bayesian	Otsu		
OA	0.9307	0.9432	0.8749	0.9305
Kappa	0.6668	0.6910	0.4907	0.5255

may be explained by the pronounced separation of the modes in the histogram of both magnitude and direction variables. The confusion matrix of the former experiment is provided in Table 3.2. The proposed method, with both thresholding options, showed OA similar to that of LLR approach, whereas, the $Kappa$ improvement is of about 14%. More important, the proposed approach provides the capability to distinguish among different kinds of change (see Fig. 3.7d, 3.7c and Fig. 3.7b), whereas LLR does not. The improvement w.r.t. the EM2DGM is of about 20%, even if an advantage given to

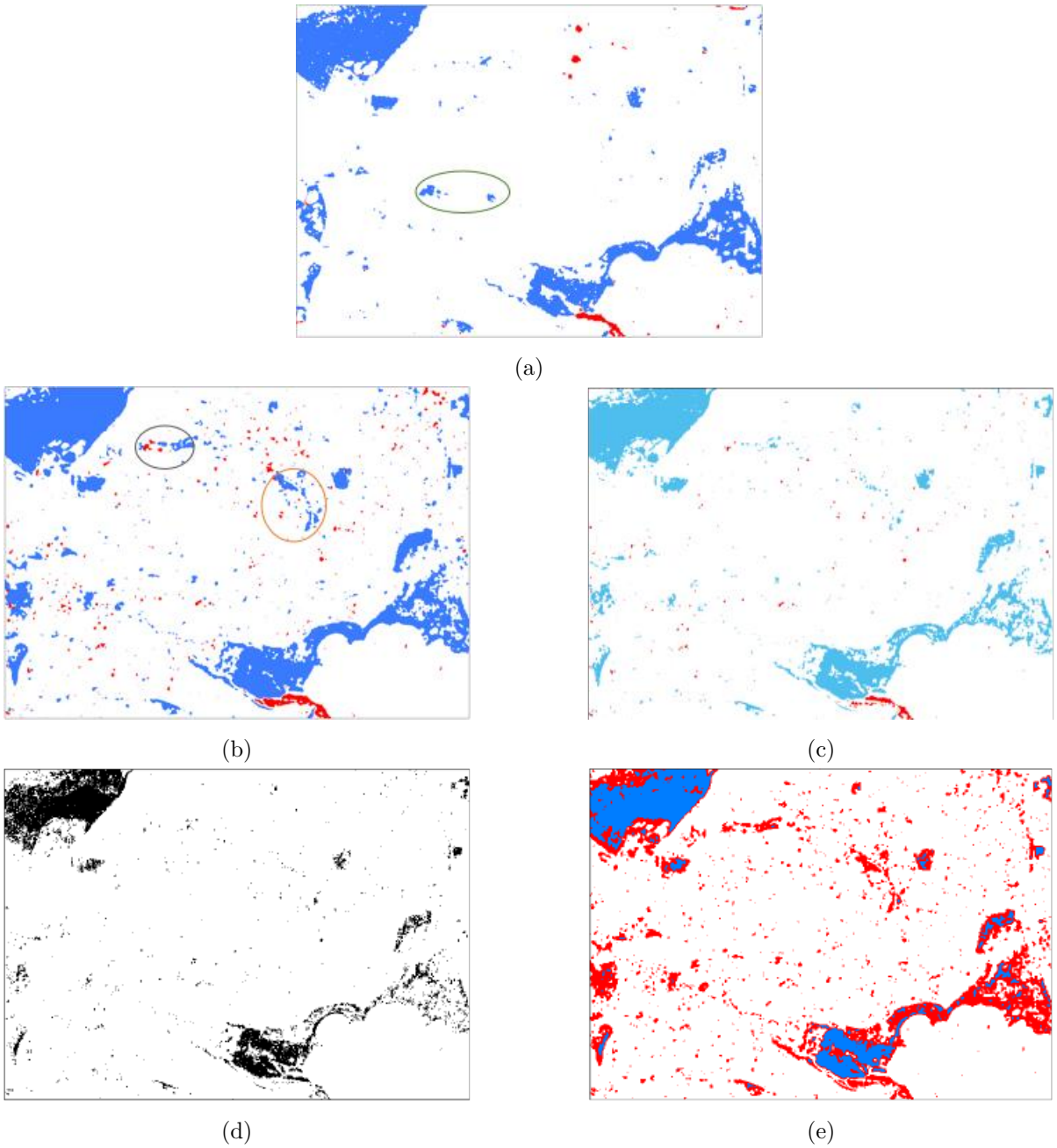

Figure 3.7: Chennai dataset maps: (a) Reference; (b) Proposed (Bayesian thresholding); (c) Proposed (Otsu thresholding); (d) LLR; (e) EM2DGM; (ω_{nc} - white, Ω_c - black, ω_{c1} - blue, ω_{c2} - red).

the ED2DGM by providing as input the known number of change classes, whereas the proposed approach estimates it automatically. A comparison between Fig. 3.7e and 3.7a shows several flooded areas being misclassified, whereas the proposed method (Figs. 3.7b and 3.7c) does not. Table 3.3 summarizes the results.

3.4.2 Los Angeles dataset

The Los Angeles dataset considers two full-pol SAR images, acquired by UAVSAR airborne sensor on the Los Angeles area (United States). The data are full-polarimetric with a spatial resolution of 0.4×1.6 meters. For our analysis, intensity information from the two polarimetric channels HH and HV was considered. The two images have been acquired on April 23, 2009 and May 11, 2015, respectively. The area has been interested by urbanization, with the construction of new buildings and the vegetation clearcut for future settlements. The two PolSAR images have been pre-processed with radiometric calibration, co-registration and multi-looking for speckle noise mitigation. The multi-looked images are characterized by a spatial resolution of 3×3 meters. A crop of 559×400 pixels has been considered. Figures 3.8a and 3.8b show the multi-temporal false-color composition of the backscattering for the HH and HV polarimetric channels, respectively. Due to the lack of ancillary data for the proposed scenario, a reference map has been generated from the Pauli RGB false-color composition of the two images by visual inspection, with the support of ancillary Landsat 5 / Landsat 7 data. The map has been generated at the best of our photo-interpretation abilities (Fig. 3.12a).
Multi-temporal comparison has been applied to the polarimetric images to compute the PCVs. Figure 3.9 shows the bivariate data distribution in the PCV polar coordinate system. The new built-up areas are characterized by positive values for both the PCV components. The change locates in a sector of the feature space with preferred direction $\phi = \frac{\pi}{4}$ (Sec. 3.2). On the other hand, pixels associated to vegetation reduction clearcut have negative values for X_{LR}^{HV}. This corresponds to a sector with preferred direction $\phi = \frac{5\pi}{4}$ in the PCV features space, as expected from the analysis in Sec. 3.2.
Bayesian thresholding of the magnitude resulted in $T_\rho = 2.4$ dB. After binary CD on the magnitude feature, multi-class CD has been applied to changed pixels only. Fig. 3.11a shows the plot of BIC with respect to the number of classes, where the smallest BIC value is associated to $K = 2$. The EM algorithm has been applied with $K = 2$ for the estimation of the priors and marginal distribution parameters. Thresholds $T_{12} = T_{21} = -0.85$ radians have been estimated with the Bayesian decision rule. Figures 3.11b and 3.12b show the direction pdf of the change classes and the multi-class CD map. Otsu thresholding led to thresholds $T_\rho = 2.76dB$ for magnitude and $T_{12} = T_{21} = 2.32$ radians for the direction, respectively, leading to the map in Fig. 3.12c. As for Chennai data set and with

(a) (b)

Figure 3.8: Los Angeles dataset: multi-temporal backscattering false color composition for (a) HH Channel; (b) HV Channel. R, B: Apr. 2009; G: May. 2015; No-change appears in gray shades, backscattering increase and decrease in green and magenta, respectively.

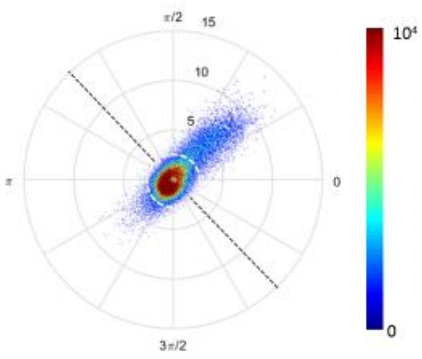

Figure 3.9: Los Angeles dataset: bivariate polar histogram (white dashed circle - T_ρ, black dashed line T_{12}).

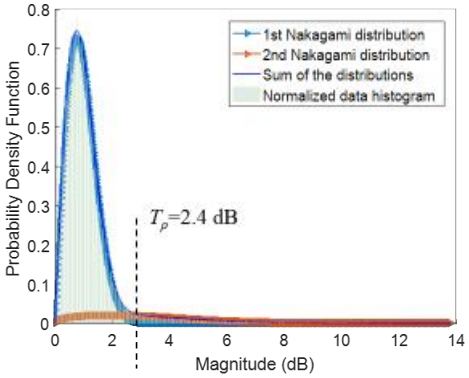

Figure 3.10: Los Angeles dataset: magnitude mixture model.

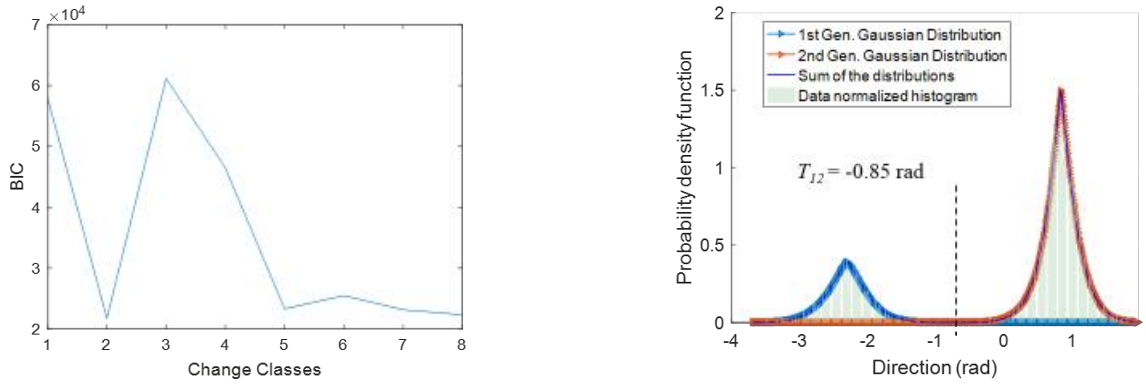

(a) (b)

Figure 3.11: Los Angeles dataset: (a) BIC analysis with respect K (minimum value is reached for $K = 2$); (b) direction histogram and estimated mixture model for $K = 2$.

Table 3.4: Los Angeles dataset: confusion matrix, and overall accuracy (OA) for the proposed approach (Otsu thresholding).

	$\hat{\omega}_{nc}$	$\hat{\omega}_{c1}$	$\hat{\omega}_{c2}$
ω_{nc}	209446	1510	1529
ω_{c1}	570	827	0
ω_{c2}	2344	0	7374
		OA	0.9734

Table 3.5: Los Angeles dataset: performance comparison with state-of-the-art methods.

	Multi-classe CD			Binary CD
Method	Proposed		EM2DGM	LLR
	Bayesian	Otsu		
OA	0.9671	0.9734	0.9257	0.9733
Kappa	0.6961	0.7218	0.4546	0.7178

similar motivations, Otsu thresholding led to slightly better performance than Bayesian one (i.e., $OA = 0.9734$ and 0.9671 and $Kappa = 0.7218$ and 0.6961, respectively). The confusion matrix of the former experiment is provided in Table 3.4. In any case, the proposed approach shows OA improvement of about 4% compared to that of EM2DGM, and similar performance to that of LLR. However, the LLR final result (see Fig. 3.12d) does not show any capability to distinguish among different kinds of change. $Kappa$ has an improvement of more than 24% with respect to EM2DGM, even if an advantage is given

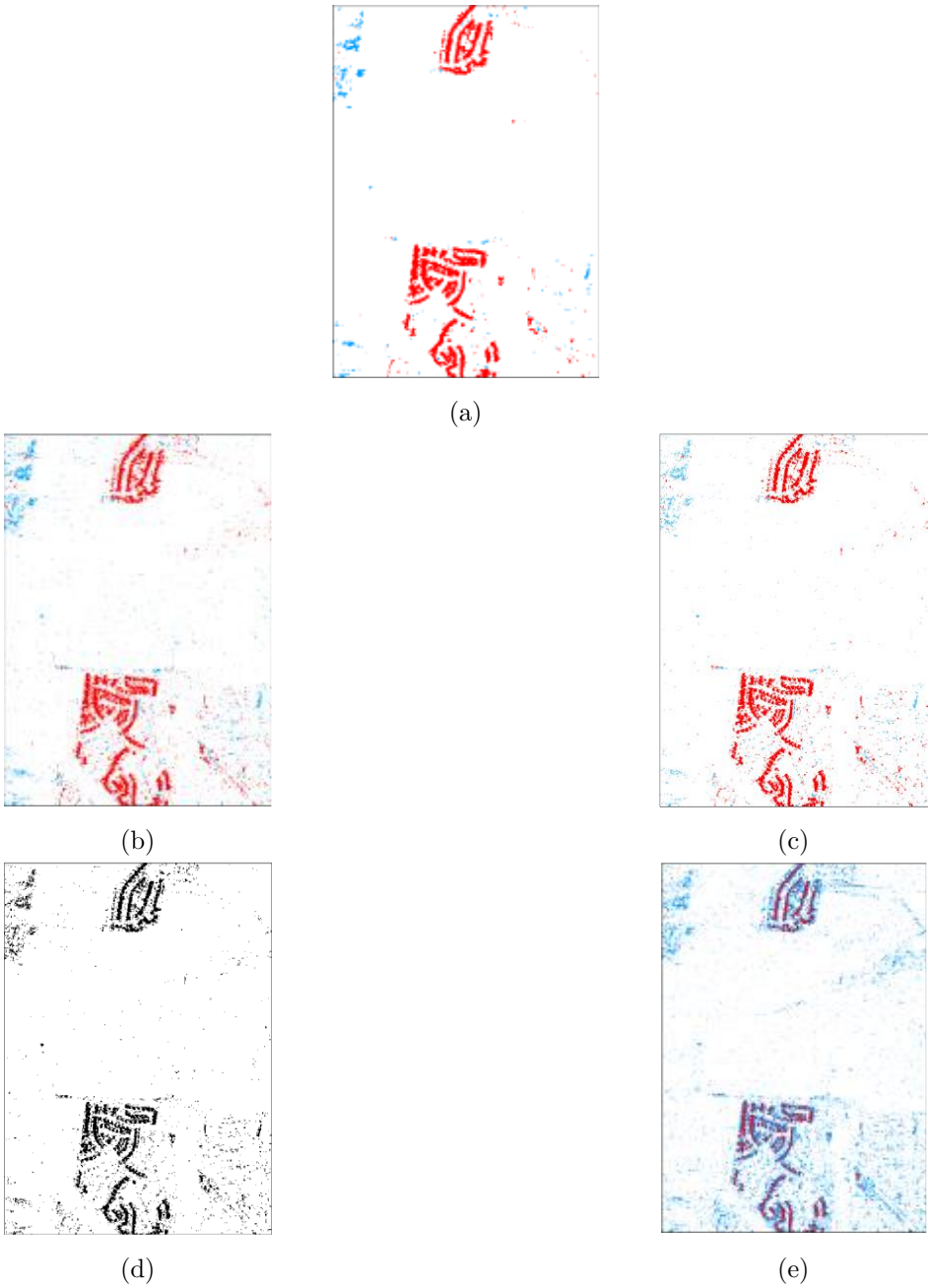

(a) (b) (c) (d) (e)

Figure 3.12: Los Angeles dataset maps: (a) Reference; (b) Proposed (Bayesian thresholding); (c) Proposed (Otsu thresholding); (d) LLR; (e) EM2DGM; (ω_{nc} - white, Ω_c - black, ω_{c1} - blue, ω_{c2} - red).

to the ED2DGM by providing as input the known number of change classes, whereas the proposed approach estimates it automatically. A comparison between Fig.3.12b, 3.12c, 3.12e and the reference map in Fig. 3.12a points out that the proposed method better identifies new built-up areas (red) than the EM2DGM. Table 3.5 summarizes the results.

3.4.3 Sardinia dataset

The Sardinia dataset includes two dual-pol SAR GRD images acquired by the Sentinel-1 SAR sensor, with a spatial resolution of 20 $\times$ 20 meters and two polarimetric channels, namely VV and VH. The two images have size 900 $\times$ 700 pixels and have been acquired on May 21, 2016 and July 20, 2016 over the area of Oristano (Italy). The area has been interested by: i) A relevant change of the surface roughness of local areas of the sea surface and water bodies, with a decrease of the swell [1]; and ii) Two kinds of change in the agricultural fields. Based on the proposed scattering model, a class of change includes the increase of dense vegetation and tillage on bare soils, respectively. The other change class includes opposite changes, due to the vegetation decrease, associated to seasonal harvesting and small fires. From a backscattering perspective, the change on the sea surface is modeled as a variation on the co-polarimetric channel only, while the changes on the vegetation are modeled by backscattering variations on both the channels, as illustrated in Sec.3.2. This dataset shows a larger complexity compared to the two previous ones, due to a large size, the larger number of changes and their complexity. The two PolSAR images have been pre-processed with radiometric calibration, co-registration and filtered. Fig. 3.13a and 3.13b show the multi-temporal false-color composition of the backscattering for the VV and VH polarimetric channels, respectively.

A reference map has been generated by photo-interpretation at the best of our abilities from a pair of Sentinel-2 optical images, acquired on the same region on the May 22, 2016 and July 18, 2016, respectively. A visual inspection was conducted on the co-polarimetric channel data for tracing water regions with changes in the surface roughness. Fig. 3.17a shows the reference map.

PCV with X_{LR}^{VV}, X_{LR}^{VH} components has been generated for each pixel. By representing the PCV in the polar coordinate system (Fig. 3.14) we see that the pixels of vegetation decrease tend to cluster in a sector with a preferred direction $\phi = \frac{5\pi}{4}$, associated to negative values for both X_{LR}^{VH} and X_{LR}^{VV}. Opposite log-ratio values are expected for pixels associated to fields growth, with a corresponding preferred direction $\phi = \frac{\pi}{4}$. Pixels of decrease of the sea swell are expected to fall in the sector with preferred direction $\phi = \pi$, in agreement with the model in Sec. 3.2.

The proposed multi-class CD approach has been applied to the dataset. Fig. 3.15 shows the EM estimated magnitude components. Bayesian thresholding of the magnitude re-

(a) (b)

Figure 3.13: Sardinia dataset: multi-temporal backscattering false color composition for (a): HH Channel; (b) HV Channel. R, B: May. 2016; G: Jul. 2016. No-change appears in gray shades, backscattering increase and decrease in green and magenta, respectively.

sulted in $T_\rho = 0.71$ dB. Multi-class CD has been applied to the set of changed pixels only. Fig. 3.16a shows the plot of the BIC criterion with respect to the number of classes, with a minimum of BIC for an optimal value $K = 3$. The EM algorithm has been applied with $K = 3$ for the estimation of the priors and the marginal distribution parameters. Fig. 3.16b shows the direction pdf and the estimated class distributions. Thresholds $T_{12} = 2.19$ radians, $T_{23} = 2.51$ radians have been estimated with the Bayesian decision rule.

The quantitative performance analysis shows that Bayesian thresholding performs better than Otsu in this case (see Tables 3.6 and 3.7). This is because of smaller separation of the change and no-change classes in the magnitude with respect to the previous experiments. After thresholding, outliers with size of one pixel were removed assuming to be associated to residual noise in the images. Figs. 3.17b and 3.17c show the final CD maps for the two thresholding options. The proposed approach for both the thresholding strategies shows OA values similar to those of LLR (see Fig. 3.17d) and EM2DGM (see Fig. 3.17e). *Kappa* has an improvement of about 18% and 2% with respect to LLR and EM2DGM, respectively. Table 3.7 summarizes the results.

3.5 Conclusion

In this chapter, a novel model for the representation of multi-class changes based in multi-temporal dual-pol SAR data has been proposed. The method relies on the backscattering information in two polarimetric channels, namely a co-polarized and a cross-polarized. The novel concept of PCV feature space has been defined representing a 2-dimensional

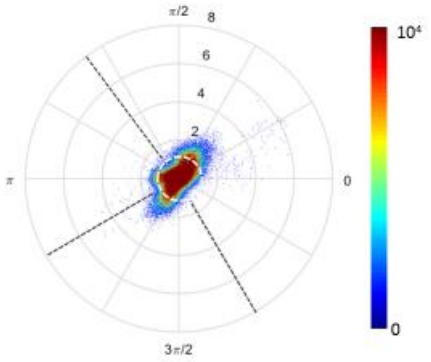

Figure 3.14: Sardinia dataset: bivariate polar histogram (white dashed circle - T_ρ, black dashed lines - T_{12}, T_{23}).

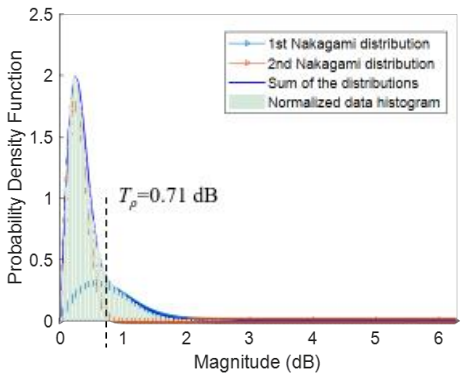

Figure 3.15: Sardinia dataset: magnitude mixture model.

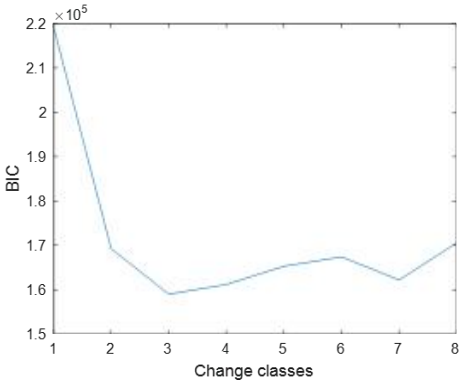

(a)

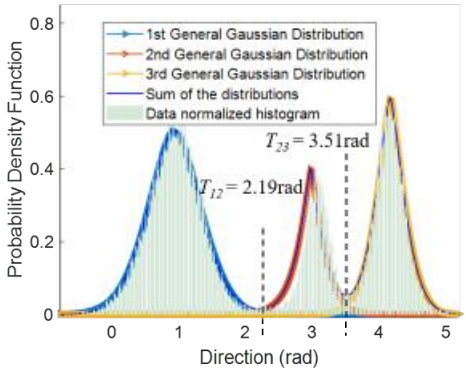

(b)

Figure 3.16: Sardinia dataset: (a) BIC analysis with respect K (minimum value is reached for $K = 3$); (b) direction histogram and estimated mixture model for $K = 3$.

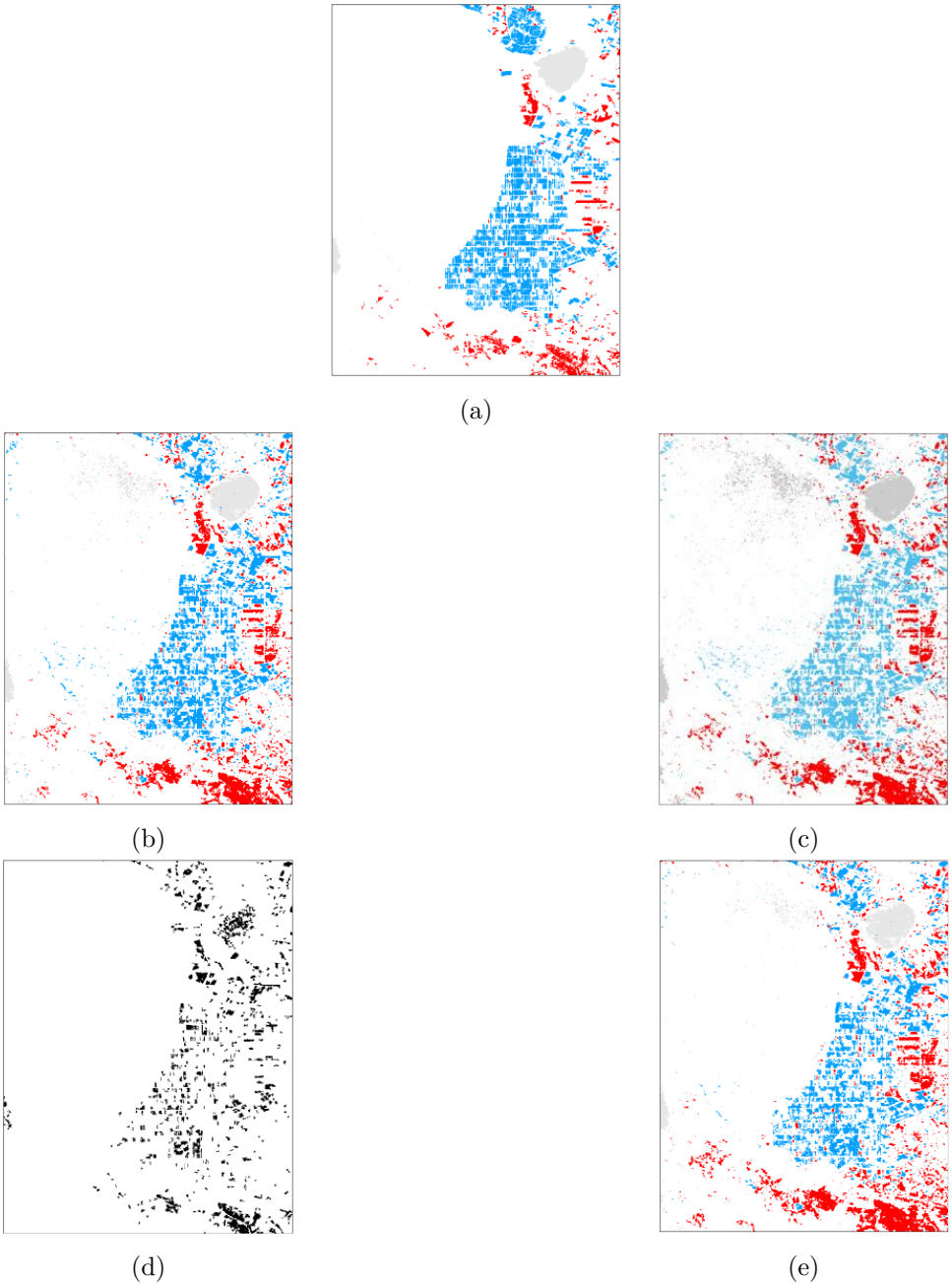

Figure 3.17: Chennai dataset maps: (a) Reference; (b) Proposed (Bayesian thresholding); (c) Proposed (Otsu thresholding); (d) LLR; (e) EM2DGM; (ω_{nc} - white, Ω_c - black, ω_{c1} - blue, ω_{c3} - gray, ω_{c3} - red).

Table 3.6: Sardinia dataset: confusion matrix, and overall accuracy (OA) for the proposed approach (Bayesian thresholding).

	$\hat{\omega}_{nc}$	$\hat{\omega}_{c1}$	$\hat{\omega}_{c2}$	$\hat{\omega}_{c3}$
ω_{nc}	504814	18494	7117	15892
ω_{c1}	20352	33593	993	99
ω_{c2}	551	14	10156	25
ω_{c3}	1285	561	90	15964
			OA	0.8961

Table 3.7: Sardinia dataset: performance comparison with state-of-the-art methods.

	Multi-class CD			Binary CD
Method	Proposed		EM2DGM	LLR
	Bayesian	Otsu		
OA	0.8961	0.8714	0.8918	0.9026
Kappa	0.6084	0.5669	0.5849	0.4307

vector with the polarimetric multi-temporal change information in a polar coordinate system. The backscattering information in the PCV feature space shows loci for both the change and no-change classes expressed in terms of polar coordinates. Physical changes occurring in the scene are mapped in specific sectors in the polar domain according to their backscattering variations in polarimetric channels. Such mapping is based on a general analysis of the backscattering sensitivity of target main parameters (i.e., surface roughness, dielectric constant or presence of dihedral structures). Based on the proposed model, a 2-step unsupervised multi-class CD approach has been derived for separating the no-change and the multi-class changes. This is a unique feature of the proposed method, where state-of-the-art ones perform binary change detection or distinguish among increase and decrease of backscattering, only.

Experimental results proved the reliability of the proposed model and the effectiveness of the CD technique on three datasets. The comparison with multi-dimensional clustering approaches pointed out a better discrimination capability of the no-change class by means of the problem decomposition along the magnitude and direction variables as well as a better multi-class CD performance, because of the explicit use of the scattering information of the physical target properties for modeling changes.

As future developments we plan to overcome the weaknesses of the method by extending it to the use in full-polarimetric multitemporal images and strengthening the analysis

on class statistical distributions. Further, since the intensity of the polarimetric channel represents only part of the information of second-order data statistics (e.g., covariance matrix) or polarimetric decomposition features, we plan to study the use of complex PolSAR information in the multi-temporal analysis for the generation of multi-class CD maps.

Chapter 4

An Unsupervised Approach to Change Detection in Built-Up Areas by Multi-Temporal Full-pol SAR Images

Information from Polarimetric SAR imagery has been used for detecting built-up targets in classification problems, whereas it has been poorly exploited for change detection in multi-temporal images. This contribution proposes a novel unsupervised approach for built-up targets change detection in multi-temporal Polarimetric SAR images. The approach is based on the joint use of total power and average scattering mechanism information for the definition of a novel index that enhances the changes associated to built-up elements. The detection is performed with Bayesian thresholding on the multi-temporal feature to identify both new constructions and demolished built-up elements. Experimental results on multi-temporal UAVSAR images demonstrate that the proposed approach provides high detection accuracy and effectively separates among different types of changes which is not the case with standard methods. [1] [2]

4.1 Introduction

Remote sensing images can be widely employed to analyze urban areas. Possible applications include the analysis of changes that shows a high importance [112] both for urban planning [21] and damage assessment [167]. Among the several available imaging sensors,

[1] Part of this chapter appears in [172]

[2] This work was carried out under the India-Trento Program for Advanced Research (ITPAR), CUP E61I18000170001.

Polarimetric Synthetic Aperture Radar (PolSAR) become highly interesting for Change Detection (CD) in built-up areas applications. PolSAR is a microwave active system measuring the radiation coherently backscattered from targets under multiple combinations of transmitted and received polarization [122]. PolSAR imagery can be acquired in all-day and all-weather conditions and is sensitive to the presence of urban structures. In the literature, PolSAR information has been largely used for image classification. In particular, most of the approaches consider either clustering based on both polarimetric features and statistical distance [72; 84; 201; 48], the use of data statistical models [195; 181; 78] or shallow/deep neural networks [231; 116].

Several approaches to change detection in single polarimetric images exist in the literature [36], while a minor effort has been devoted to the exploitation of the multi-temporal polarimetric information for change detection. Some studies considered hypothesis test based on Log-likelihood ratio for the multi-temporal data [6; 53; 67]. Others considered change detectors based on the optimization of power ratio or difference [149; 176]. Others derived change detectors based on the multi-temporal comparison of features derived from the Covariance matrix or its polarimetric decomposition [167; 171; 132; 104; 172; 43; 223].But all of them deal with the detection of presence/absence of change and do not distinguish among different types of change.

In PolSAR imagery, scattering from distributed targets is represented in terms of second-order statistics, considering multilooked information from the complex scattering coefficients represented in terms of coherency matrix T (or equivalent covariance matrix C). Different decompositions of the matrix T have been proposed, in order to extract target features. Some of them are based on different scattering mechanisms, with three (i.e., double-bounce, surface and volume scattering) or more contributions[123; 167]. Built-up elements in urban areas are ideally characterized by a dominant double-bounce contribution. Nevertheless, the estimation of the parameters is practically affected by the relative orientation angle between the man-made target and the range direction, which provides an overestimation of the volume scattering and thus requires a compensation [167]. Other decompositions are based on the eigenvalues and eigenvectors of T. In [65], eigen-features are used for defining three parameters insensitive to the target orientation angle, namely Entropy (H), Anisotropy (A) and average alpha angle (α). H and A characterize the relative proportion of the three eigenvalues, thus the composition of the scattering contributions and α characterizes the average scattering type associated to the cell. The total scattering power P can be considered as a complementary information to discriminate different targets which may present similar polarimetric behavior (e.g., regions with multiple simultaneous scattering processes) [48].

In this contribution, we aim at defining a novel CD method for built-up areas in PolSAR

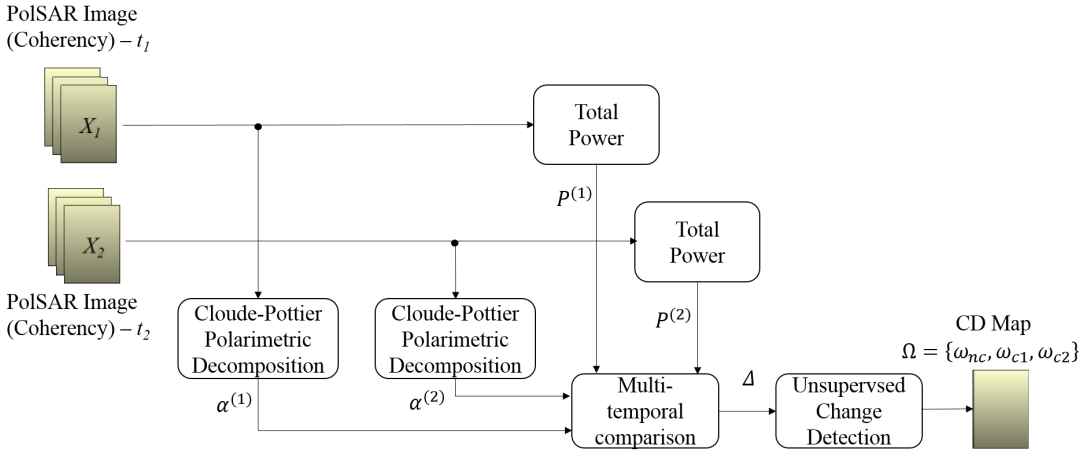

Figure 4.1: Block scheme for the proposed approach.

multi-temporal data. The proposed strategy considers the joint use of both polarimetric α and P from the two single-time PolSAR images for defining a multi-temporal change index sensitive to multi-temporal variation of both the scattering mechanism and the overall power. The proposed index shows the capabilities of detecting the changes in built-up areas by separating them from other types of change which is not the case when using only α information in dense environments [48] and distinguishing among new constructions and destroyed built-up elements. An unsupervised thresholding of the change index based on the Bayesian decision rule provides the final CD map with two change classes (i.e., constructed and demolished built-up elements) and a no-change class.
The chapter is structured into four sections. Section 4.2 describes both the proposed feature space and the automatic CD strategy. Section 4.3 illustrates the dataset and experimental results. Finally, Section 4.4 draws the conclusions of this contribution and provides future developments.

4.2 Proposed CD approach in Full-pol SAR images

Let us consider two full-pol images X_1, X_2 acquired over the same area at times $t_1, t_2, t_1 < t_2$, respectively. The proposed approach aims at deriving a map of change detection showing a class of no-change ω_{nc} and two classes of changes in built-up elements ω_{c1} (i.e., demolished building) and ω_{c2} (i.e., constructed building), respectively. Fig. 4.1 shows the block scheme for the proposed approach.

4.2.1 Definition of the change index

In PolSAR imagery, scattering is represented with complex scattering coefficients S_{pq} with polarizations q and p on the transmitting and the receiving wave [122]. The coefficients are grouped in form of matrix or vector. In the Pauli basis, $k_P = \frac{1}{\sqrt{(2)}}[S_{HH} + S_{VV}; S_{HH} - S_{VV}; 2S_{HV}]$. Natural targets have distributed scatterers and thus a second-order statistics is needed to model them. For Pauli representation, the Coherency matrix T represents the average multi-look scattering. T is defined as follows:

$$T = \frac{1}{L}\sum_{L} k_P k_P^H = \begin{bmatrix} T_{11} & T_{12} & T_{13} \\ T_{21} & T_{22} & T_{23} \\ T_{31} & T_{32} & T_{33} \end{bmatrix} \tag{4.1}$$

being L the number of looks. Polarimetric information of coherency matrix can be represented with few features derived from both matrix eigenvalues and eigenvectors, namely Anisotropy A, Entropy H and average alpha α.

$$A = \frac{\lambda_2 - \lambda_3}{\lambda_2 + \lambda_3} \tag{4.2}$$

$$H = \sum_{i=1}^{3} \frac{\lambda_i}{\sum_{i=1}^{3}\lambda_i} \log\left(\frac{\lambda_i}{\sum_{i=1}^{3}\lambda_i}\right) \tag{4.3}$$

$$\alpha = \sum_{i=1}^{3} \frac{\lambda_i \alpha_i}{\sum_{i=1}^{3}\lambda_i} \tag{4.4}$$

being $v_i = \left[\cos\alpha_i, \sin\alpha_i \cos\beta_i e^{\delta_i}, \sin\alpha_i \sin\beta_i e^{\gamma_i}\right]^T e^{j\phi_i}$ and λ_i, $i = 1, 2, 3$ the eigenvectors and the corresponding eigenvalues for T, $\lambda_1 > \lambda_2 > \lambda_3 \geq 0$. H measures the degree of scattering randomness ranging from 0 (i.e., a single scattering mechanism is present) to 1 (i.e., all the scattering mechanisms have equal power). A measures the importance of the second dominant scattering mechanism in the range 0-1 as well. α characterizes the average scattering type of the target cell. High values are associated to the double-bounce scattering mechanism, while low values are associated to the surface scattering. Intermediate values are associated to the volume scattering [65; 122].
A measure of the total scattered power associated to T is defined by the span P:

$$P = \sum_{i=1}^{3} \lambda_i = trace(T) \tag{4.5}$$

Built-up areas, which are corner reflector structures, are characterized by a large scattering power, which is concentrated typically on the T_{22} and the T_{33} terms. This corresponds

to intermediate or high α values. Instead, vegetation and surface elements (e.g., roads or soils) are characterized by a lower total scattering power, with α assuming low to intermediate values, depending on the characteristics of the target and the density of the scatterers.
Let $\alpha^{(i)}, P^{(i)}$ be the average alpha and the total power associated to $X_i, i = 1, 2$, respectively. The proposed overall change index that accounts for both types of multi-temporal variations is defined as follows:

$$\Delta = \sqrt{\frac{P^{(2)}}{P^{(1)}}}\alpha^{(2)} - \sqrt{\frac{P^{(1)}}{P^{(2)}}}\alpha^{(1)} = \frac{1}{\sqrt{\sum_{i=1}^{3}\lambda_i^{(1)}\sum_{k=1}^{3}\lambda_k^{(2)}}}\left(\sum_{k=1}^{3}\lambda_k^{(2)}\alpha_k^{(2)} - \sum_{i=1}^{3}\lambda_i^{(1)}\alpha_i^{(1)}\right) \tag{4.6}$$

Because of the inclusion of the multi-temporal power information, Δ is defined as a real value. For changes preserving the power, but modifying the average scattering mechanism (i.e., $P^{(1)} = P^{(2)}, \alpha^{(1)} \neq \alpha^{(2)}$), Δ degenerates in the multi-temporal α difference [104; 172], with positive and negative values associated to the increase and decrease of the α, respectively. For changes in the total power preserving the average scattering mechanism (i.e., $P^{(1)} \neq P^{(2)}, \alpha^{(1)} = \alpha^{(2)}$), Δ degenerates in a scaled version of the square root of the span ratio, which is proportional to an amplitude ratio [157].
If we focus on the changes in built-up elements, the creation of a built-up element shows an increase of the overall scattering power P and an increase of α, which are combined in a large positive value for Δ. On the other side, the demolition of a built-up element shows a decrease of the overall scattering power P and a decrease of α, which are combined in a large negative value for Δ. Changes associated to natural elements show small variations in at least P or α, thus Δ shows values close to zero.

4.2.2 Automatic Change Detection of built-up areas

An automatic strategy is applied for the detection of the three classes $\omega_{nc}, \omega_{c1}, \omega_{c2}$, by considering an unsupervised thresholding of Δ based on the Bayesian decision rule. Let δ be the random variable associated to the samples of Δ, with probability density function $p(\delta)$. The analytical derivation of a statistical model for $p(\delta)$ based on statistical properties of the PolSAR data would be a complex task. To the best of our knowledge, some works in the literature proposed statistical models for square root of SAR intensity ratio in case of single polarimetric channel (i.e., Nakagami-ratio or Weibull-ratio pdfs [156]), but no model focused on span for multiple polarimetric channels. Further, no statistical model has been proposed for the single-date α. Since Δ (4.6) depends on P and α, a statistical model for p(δ) cannot be derived (and its derivation is out of the scope of this work). Therefore,

in this work $p(\delta)$ is modeled as a mixture of three Generalized Gaussian distributions, each associated to one class. The Generalized Gaussian mixture presents a good trade-off between the model complexity and the data-fitting capabilities.

$$p(\delta) = \sum P(\omega_i) \frac{\beta_i}{2\gamma_i \Gamma(1/\beta_i)} e^{\{\frac{\delta-\mu_i}{\gamma_i}\}^{\beta_i}}; \omega_i \in \{\omega_{nc}; \omega_{c1}; \omega_{c2}\} \tag{4.7}$$

being $P(\omega_i), \mu_i, \gamma_i, \beta_i$ the prior probability, the location, scale and shape parameters for the class ω_i, respectively. The estimation of the unknown parameters is conducted by applying the EM algorithm. The algorithm iteratively computes the optimal parameter estimates which maximize the data log-likelihood. In particular, for the $(q+1)$-th iteration, the estimates are given by the following equations:

$$P^{(q+1)}(\omega_i) = \frac{\sum_{z=1}^{card\{\Delta\}} p^{(q)}(\omega_i|\delta_z)}{card\{\Delta\}} \tag{4.8}$$

$$\gamma_i^{(q+1)} = \left[\frac{\beta_i^{(q)} \sum_{z=1}^{card\{\Delta\}} p^{(q)}(\omega_i|\delta_z) \left|\delta_z - \mu_i^{(q)}\right|^{\beta_i^{(q)}}}{\sum_{z=1}^{card\{\Delta\}} p^{(q)}(\omega_i|\delta_z)} \right]^{1/\beta_i^{(q)}} \tag{4.9}$$

$$\sum_{z=1}^{card\{\Delta\}} p^{(q)}(\omega_i|\delta_z) \frac{\beta_i^{(q)}}{\left(\gamma_i^{(q)}\right)^{\beta_i^{(q+1)}}} \left|\delta_z - \mu_i^{(q+1)}\right|^{\beta_i^{(q)}-1} \cdot sign\left(\delta_z - \mu_i^{(q+1)}\right) = 0 \tag{4.10}$$

$$\sum_{z=1}^{card\{\Delta\}} p^{(q)}(\omega_i|\delta_z) \left[\frac{1}{\beta_i^{(q+1)}} + \frac{\psi\left(\frac{1}{\beta_i^{(q+1)}}\right)}{\left(\beta_i^{(q+1)}\right)^2} - \left(\frac{\left|\delta_z - \mu_i^{(q)}\right|}{\gamma_i^{(q)}} \right)^{\beta_i^{(q+1)}} \log\left(\frac{\left|\delta_z - \mu_i^{(q)}\right|}{\gamma_i^{(q)}} \right) \right] = 0 \tag{4.11}$$

The iterative process stops when either values converge or the maximum number of iterations is reached. Initialization is conducted by K-means clustering and deriving a Maximum Likelihood Estimation of the parameters for each cluster. At the end, Bayesian decision rule is applied for detecting the class of each sample of $\widehat{\Delta\alpha}$.

$$\omega = \underset{\omega_i \in \{\omega_{nc}; \omega_{c1}; \omega_{c2}\}}{\arg\max} P(\omega_i) \frac{\beta_i}{2\gamma_i \Gamma(1/\beta_i)} e^{\{\frac{\delta-\mu_i}{\gamma_i}\}^{\beta_i}} \tag{4.12}$$

4.2.3 CD of built-up areas in large images

Thresholding assumes that classes are statistically represented in the sample set. This assumption turns out to be seldom satisfied in CD in large input images, where the largest

portion is typically non-changed. This would affect the accuracy of the threshold selection and the detection. In order to overcome this problem, a split-based analysis is applied to the Δ index [33]. The image is divided into N_{spl} non-overlapping splits, each with size $N_{tr} \times N_{tc}$. Let $\Delta_s, s = 1, ..., N_{spl}$ and σ_s^2 be the s-th split and the corresponding Δ variance, respectively. σ_s^2 provides an indication of the classes balance in the split. Large values indicate the presence of more than one class, while small values indicate a dominant class in the split. The set of N_{spl} variance values are evaluated in order to consider those splits with largest variance. The analysis provides as output a union of splits $\widehat{\Delta}$, defined as follows:

$$\widehat{\Delta} = \left\{ \bigcup_s \Delta_s : \sigma_s^2 \geq m_{\sigma^2} + B\sigma_{\sigma^2} \right\} \tag{4.13}$$

being $m_{\sigma^2}, \sigma_{\sigma^2}$ the mean and standard deviation of the N_{spl} variance values and B a scalar coefficient. The sample subset $\widehat{\Delta}$ is used for the robust estimation of the mixture parameters and the Bayesian thresholding.

4.3 Experimental Results

For the validation of the proposed approach, two multi-temporal PolSAR images acquired by UAVSAR sensor over the city of Los Angeles, California (USA) have been considered. The two full polarimetric images have been acquired on April 23, 2009 and May 11, 2015, respectively. The two images have been calibrated, co-registered and multi-looked. The pre-processed products are characterized by a geometrical resolution of 3×3 meters. The Los Angeles area has been interested by a large urbanization phenomenon, with the construction of new built-up areas on bare land and the removal of vegetated areas for possible future settlements.

From the pair of images, the experimental analysis considered two crops: a single-change scenario, with size 559×400 pixels; and multi-change scenario, with size 400×393 pixels. Based on the Pauli false color composition for the two single-time acquisitions, a reference map has been generated for the two crops by visual inspection. Performance has been assessed in terms of Overall Accuracy (OA) and Kappa Coefficient ($Kappa$). In order to prove its effectiveness, the proposed approach has been compared with state-of-the-art polarimetric CD techniques. In particular, a binary CD method based on the Log-Likelihood Ratio (LLR) test [67], and a method based on geodesic distance and PCA-based K-means (PCAK) [180]. Both the methods provide binary CD information, with no discrimination between the classes ω_{c1} and ω_{c2}. A further comparison has been performed with Bayesian thresholding approaches applied to the log-ratio of HH intensity (HHLR-BT [112]) and α difference ($\Delta\alpha$-BT [172]).

(a) (b) (c)

Figure 4.2: Pauli RGB false-color composite for (a) pre-, and (b) post-event scene; (c) Δ. (Single-change scenario).

4.3.1 Single-change Scenario

The first scenario is characterized by the construction of two extended built-up areas on bare land, which is associated to class ω_{c2}. Fig.4.2a and 4.2b show the Pauli False color composition of both pre- and post-event, respectively. For the two images, eigenvalue-based polarimetric decomposition has been applied to T and parameters α, P have been computed. Δ has been generated via multi-temporal comparison of the single-time P and α. Fig. 4.2c shows the image for Δ. EM algorithm and Bayesian thresholding were applied for deriving the CD map. Based on the prior knowledge of the scene, ω_{c1} has been neglected in the thresholding problem. Fig. 4.3a shows the final CD map. A comparison with the reference map (see Fig.4.3b) shows a good accuracy in the detection. A numerical assessment, conducted via the generation of the confusion matrix (reported in Table 4.1), results in $OA = 0.9776$ and $Kappa = 0.7400$.

Table 4.2 shows an overview of the performance comparison with state of the art methods, in particular LLR (see Fig.4.3c), GD-PCAK (see Fig. 4.4b), HHLR-BT (see 4.4a) and $\Delta\alpha$-BT (see 4.4c). From the values, the proposed method has same performance of LLR in terms of OA and slightly lower in terms of $Kappa$ (i.e., 3% of difference). The two methods show overall better performance than the other methods considered, especially for $Kappa$, which show a gap of more than 10%).

4.3.2 Multi-change Scenario

The second dataset presents a more complex scenario with the construction (ω_{c2} class) and the demolition (ω_{c1} class) of built-up areas having variable size. Fig. 4.5a and Fig. 4.5b show the Pauli false color composition associated to pre- and post-event of the multi-

(a) (b) (c)

Figure 4.3: (a) CD map for the proposed approach; (b) Reference map ; (c) CD map for LLR. (Single-change scenario, ω_{nc} - white, ω_{c2} - black)

.

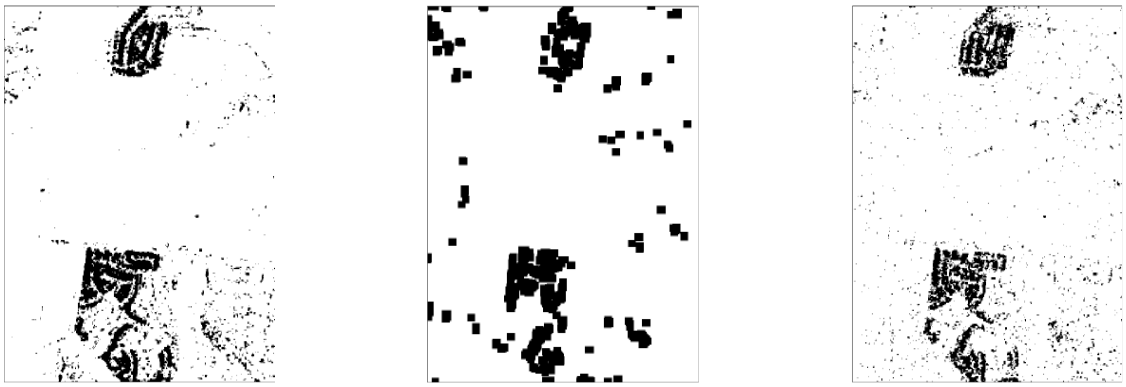

(a) (b) (c)

Figure 4.4: (a) CD map for HHLR-BT; (b) CD map for GD-PCAK; (c) CD map for $\Delta\alpha$-BT. (Single-change scenario, ω_{nc} - white, ω_{c2} - black)

.

Table 4.1: Confusion Matrix for the proposed approach. (Single-change scenario).

	$\hat{\omega}_{nc}$	$\hat{\omega}_{c2}$
ω_{c1}	211034	1328
ω_{c2}	3673	7565
	OA	0.9776
	Kappa	0.7400

Table 4.2: Overview of Performance assessment. (Single-change Scenario).

Method	**OA**	**Kappa**
Proposed	0.9776	0.7400
HHLR-BT	0.9602	0.6799
$\Delta\alpha$-BT	0.9579	0.6194
LLR	0.9787	0.7774
GD+PCAK	0.9224	0.4812

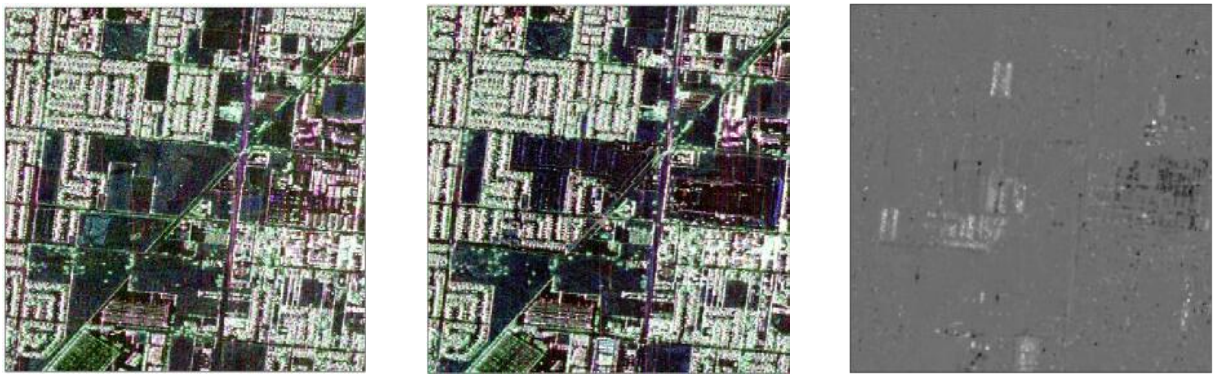

(a) (b) (c)

Figure 4.5: Pauli RGB false-color composite for (a) pre-, and (b) post-event scene; (c) Δ. (Multi-change scenario).

change scenario, respectively. Δ has been computed (see Fig. 4.5c) and EM algorithm and Bayesian thresholding were applied for estimating the classes and deriving the CD map (see Fig. 4.6a).

A quantitative performance assessment of the map accuracy has been conducted with the reference map in Fig. 4.6b, resulting in values $OA = 0.9689$ and $Kappa = 0.6128$. Fig. 4.6c-4.7c show the output map yielded by the comparison methods. Table 4.4 shows

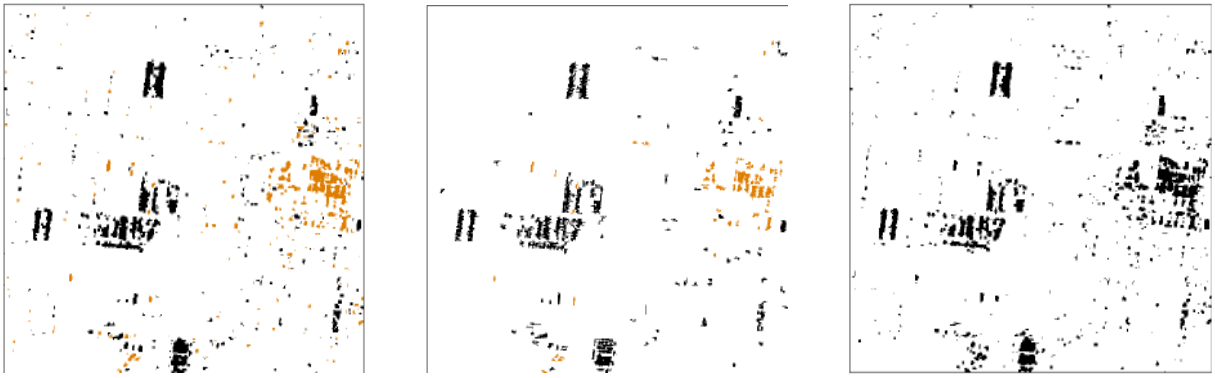

(a) (b) (c)

Figure 4.6: (a) CD map for the proposed approach; (b) Reference map; (c) CD map for LLR. (Multi-change scenario, ω_{nc} - white, ω_{c1} - orange, ω_{c2} - black).

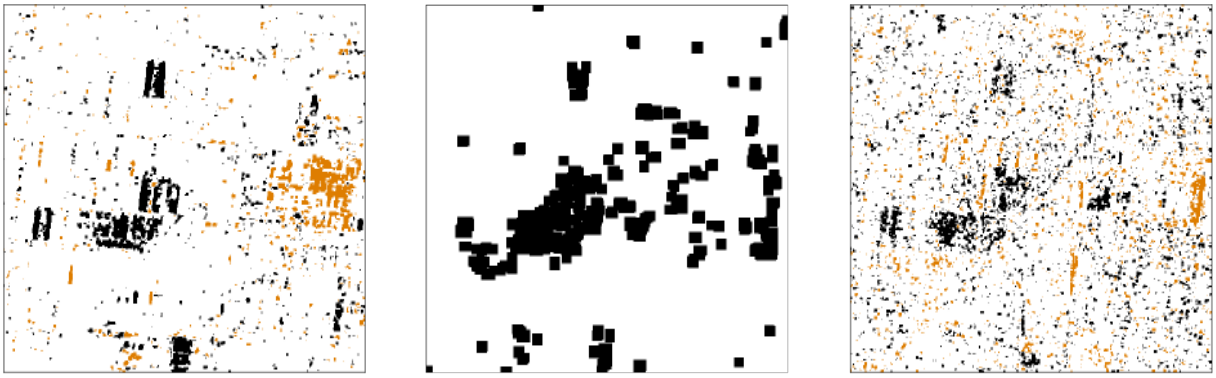

(a) (b) (c)

Figure 4.7: (a) CD map for HHLR-BT; (b) CD map for GD-PCAK; (c) CD map for $\Delta\alpha$-BT. (Multi-change scenario, ω_{nc} - white, ω_{c1} - orange, ω_{c2} - black).

an overview of the performance comparison with state of the art methods. The proposed method shows similar performance in terms of both *Kappa* (i.e., improvement of 1%) and *OA* to that of LLR (see Fig. 4.6c), but it provides discrimination of the change classes ω_{c1}, ω_{c2}, whereas LLR does not. Besides, the proposed approach shows an improvement of more than 3% and 15% of *Kappa* and *OA* with respect to the other approaches. A comparison between Fig. 4.7c and Fig. 4.6a shows how the inclusion of the power information overcomes the issues associated to the definition of α in heterogeneous dense urban areas.

Table 4.3: Confusion Matrix for the proposed approach. (Multi-change scenario).

	$\hat{\omega}_{nc}$	$\hat{\omega}_{c1}$	$\hat{\omega}_{c2}$
ω_{nc}	987	119	0
ω_{c1}	1742	148249	2100
ω_{c2}	3	920	3080
		OA	0.9689
		Kappa	0.6128

Table 4.4: Overview of Performance assessment. (Multi-change scenario).

Method	**OA**	**Kappa**
Proposed	0.9689	0.6128
HHLR-BT	0.9361	0.4609
$\Delta\alpha$-BT	0.8682	0.0990
LLR	0.9691	0.6119
GD+PCAK	0.8551	0.1592

4.4 Conclusion

In this work, we proposed a novel method for change detection of built-up areas by means of multi-temporal PolSAR data. The method is based on the definition on a change index accounting for both the total power and the Cloude-Pottier α angle from the single-time images. An unsupervised thresholding strategy based on the Bayesian decision rule is applied to the proposed index in order to detect constructed and demolished built-up areas in the multi-temporal scene. Experimental results conducted on two datasets of multi-

temporal PolSAR images show the effectiveness of the proposed approach with respect to standard methods in terms of both capability of discriminating opposite changes and accuracy performance.
Future developments aim at studying the statistical distribution of Δ and introducing context information in the detection problem. We also aim at testing the proposed approach on different urban scenarios.

Chapter 5

Wavelet Temporal Analysis of Polarimetric Decomposition Parameters over Alpine Glaciers

The use of PolSAR image time-series introduces a set of multiple observations, with redundant information that can be used for classification and with the possible presence of smooth and abrupt changes. Significant features for representing the multi-temporal information can be derived from the use of multiple polarimetric features and wavelet operators. This contributions presents a novel framework for time series of full-pol SAR images based on the joint use of arithmetical and geometrical wavelet transforms on full-polarimetric decomposition features. The multi-temporal features are exploited for both the separation of multi-temporal natural classes and for the analysis of changes with different temporal evolution. Experimental analysis conducted on a multi-temporal dataset of full-polarimetric SAR images illustrated the effectiveness of the proposed framework for the separation of multi-temporal classes and for the analysis of seasonal changes.

5.1 Introduction

Among the several imaging sensors, Synthetic Aperture Radar (SAR) systems operating on spaceborne and airborne platforms, represent an important technology for the Earth observation. SARs are active imaging systems operating in the microwave spectrum and measuring the coherent scattering from the targets on the scene. These peculiarities make the instrument poorly sensible to cloud coverage and illumination conditions and suitable for the multi-temporal monitoring of the scene. Polarimetric SARs extend the SAR imaging capabilities by considering multiple polarimetric channels (i.e., the polarization of the

transmitted and/or received radiation is variable). The enhanced information can be used for better target discrimination [122].

In the last decade, large datasets of multi-temporal SAR and PolSAR images have been delivered to the scientific community. This led to a large interest in the use of multi-temporal data for robust classification [45; 114; 160; 20], for the detection of changes [37; 46] and for the multi-temporal analysis of natural features (e.g., snow monitoring [159; 188], crop phenology identification [138], soil moisture analysis [118; 166], glacier displacement [12; 11; 221; 153]). A large part of the literature based on multi-temporal Polarimetric SAR data considers the comparison of two SAR images for bi-temporal Change Detection (CD) [37]. Some studies considered hypothesis tests based on the log-likelihood ratio [67; 52; 6], others considered the optimization of contrast measures [148; 149] or the multi-temporal comparison of features derived from polarimetric decompositions in the literature [167; 61]. On the other hand, the use of a PolSAR image time series has been devoted for the analysis of temporal patterns for natural features [118; 221] and the robust image classification for non-changed areas [142]. A minor effort has been put in the detection of both abrupt and gradual changes from a PolSAR time series [135].

In the SAR image analysis, the wavelet transform is an important tool for separating different aspects of the SAR information associated to the low and high frequencies. The wavelet transform has been exploited in the detection of multi-scale changes from multi-temporal SAR images [32; 113; 54; 70] or in the texture analysis [91; 10]. These approaches apply the wavelet transform on the spatial domain, mitigating the noise effects on the image and preserving the detail information. If we consider the use of the wavelet transform along the temporal direction for a multi-temporal pixel set (i.e., the spatial information is globally kept), a novel pixel-based multi-temporal comparison can be defined, such that: i) robust multi-temporal image classes can be identified; and ii) the detection of both abrupt and gradual changes can be performed [12]. Besides, the literature has mainly considered the application of the standard wavelet to features characterized by both different statistical distribution and noise phenomena (i.e., additive Gaussian noise for optical data and Gamma multiplicative noise for SAR intensity data). These differences may affect the performance of the wavelet decomposition. Thus, an alternative wavelet formulation under the assumption of multiplicative noise has been derived in [12], but it has been poorly exploited in the SAR image analysis.

In this chapter, we propose a joint arithmetic and geometrical wavelet framework for the analysis of multi-temporal full-pol SAR data. The joint framework includes the selection of wavelet transforms that are relevant for the sparse description of PolSAR decomposition features. In this framework, multiplicative and additive interacting variables are associated with geometrical and arithmetic wavelets, respectively. Multi-scale [32] and spline

strategies [185] are defined based on the wavelet transform. The information inferred in this framework aims at both i) separating different natural multi-temporal classes; and ii) the detection of changes and the analysis of their temporal evolution. The proposed analysis is applied on a multi-temporal PolSAR dataset acquired from Radarsat-2 on the Argentière glacier in the French Alps, which presents different evolutions between winter and summer seasons over different parts of the glacier.
This chapter is structured into five sections. Section 5.2 we describe the polarimetric features and the wavelet strategies considered for the analysis. Section 5.3 describes the multi-temporal dataset and the experimental setup. Section 5.4 illustrates the experimental results. Finally, in Section 5.5 we trace the conclusions and the future developments of this work.

5.2 Proposed multi-temporal framework for Full-pol SAR images

Let us consider a time-series of N PolSAR images $I_t, t = 1, ..., N$. Polarimetric information of each image is represented with second-order scattering information of Coherency matrix T.

$$T = \frac{1}{L}\sum_{L} k_P k_P^H = \begin{bmatrix} T_{11} & T_{12} & T_{13} \\ T_{21} & T_{22} & T_{23} \\ T_{31} & T_{32} & T_{33} \end{bmatrix} \tag{5.1}$$

being $k = [S_{HH} + S_{VV}, S_{HH} - S_{VV}, 2S_{HV}]/\sqrt{2}$ the complex scattering vector in the Pauli basis. Polarimetric decompositions of the coherency matrix T provide a representation of the information of T in terms of few features, typically based on the eigen-based features or the composition of contributions from elementary targets [220; 64].

5.2.1 Definition of the polarimetric features

In this work, two polarimetric decompositions are taken into account, namely the Cloude/Pottier [65], which results in the three features Anisotropy A, Entropy H and average alpha α, and the Yamaguchi4 [159; 220], which results in the four power scattering terms: double bounce, surface, volume and helix.

$$A = \frac{\lambda_2 - \lambda_3}{\lambda_2 + \lambda_3} \tag{5.2}$$

$$H = \sum_{i=1}^{3} \frac{\lambda_i}{\sum_{i=1}^{3} \lambda_i} \log\left(\frac{\lambda_i}{\sum_{i=1}^{3} \lambda_i}\right) \tag{5.3}$$

$$\alpha = \sum_{i=1}^{3} \frac{\lambda_i \alpha_i}{\sum_{i=1}^{3} \lambda_i} \tag{5.4}$$

$$T = f_s T_{surf} + f_d T_{double} + f_h T_{helix} + f_v T_{volume} \tag{5.5}$$

being $\{f_s, f_v, f_h, f_d\}$, $\{T_{surf}, T_{volume}, T_{helix}, T_{double}\}$ the power coefficients and the coherency matrices associated to the surface, volume, helix and double-bounce mechanism, respectively, and being $v_i = \left[\cos\alpha_i, \sin\alpha_i \cos\beta_i e^{\delta_i}, \sin\alpha_i \sin\beta_i e^{\gamma_i}\right]^T e^{j\phi_i}$ and $\lambda_i, i = 1,2,3$ the eigenvectors and the corresponding eigenvalues for T, $\lambda_1 \geq \lambda_2 \geq \lambda_3 \geq 0$. H describes the degree of scattering randomness, with values ranging from 0 (i.e., single dominant eigenvalue) to 1 (i.e., all eigenvalues with same value). A describes the importance of the second and third eigenvalues and is defined in the range $0-1$. α characterizes the average scattering type of the target, with high and low values associated to double-bounce and surface scattering type, respectively (intermediate values are associated to the volume scattering).

5.2.2 Definition of the geometrical and arithmetical wavelet operators

When considering the pattern analysis along both the spatial and temporal directions, the wavelet analysis has proved to be an effective tool [144]. In this work, we assume wavelet analysis focusing along the temporal direction only. Each temporal wavelet approach yields two sub-bands for each scale level, namely approximation and detail. Classic wavelet analysis (e.g., arithmetical wavelets) assume an additive Gaussian noise affecting the image. For the pixel (x, y), the arithmetical wavelet element is defined as follows:

$$X_t^{(W_{ab},k)}(x,y) = \sum_{l=0}^{L-1} W_b(l) X_{t-l}^{(W_{aA},k-1)}(x,y) \tag{5.6}$$

being $I_t^{(W_{ab},k)}$ the temporal sequence of the wavelet component b at scale k for the feature X, computed with arithmetical wavelet, $W_b(\cdot)$ the wavelet filter response and b an indicator for the approximation (i.e., $b = A$) and detail component (i.e., $b = D$), respectively. On the other hand, geometrical wavelets [12] have been designed for data with multiplicative noise, and they are defined as follows:

$$\begin{aligned} X_t^{(W_{gb},k)}(x,y) &= \exp\left[\sum_{l=0}^{L-1} W_b(l) \log\left(X_{t-l}^{(W_{aA},k-1)}(x,y)\right)\right] \\ &= \prod_{l=0}^{L-1} \left(X_{t-l}^{(W_{aA},k-1)}(x,y)\right)^{W_b(l)} \end{aligned} \tag{5.7}$$

being $X_t^{(W_{gb},k)}$ the temporal sequence of the wavelet component b at scale k for the feature I, computed with geometrical wavelet. Among the several wavelet transforms in the literature (e.g., Symlet, Daubechies), the Haar-1, with coefficients $W_A = [1,1]\sqrt{2}$ and $W_D = [1-1]\sqrt{2}$ for the approximation and detail component respectively, has a particular interest because of its easy representation and properties. Image difference and image ratio can be represented as the application of the arithmetical and geometrical Haar-1 wavelet along the temporal direction, respectively. In this work, the selection of the use of arithmetical or geometrical wavelet is based on the statistical similarity between the feature probability density function (pdf) and the Gaussian or the Gamma distribution. The similarity is measured with one of the statistical distance measures (e.g., Kullback-Leibler distance or Hellinger distance [28]). Without loss of generality, let us consider the case of the arithmetical wavelet for the multi-temporal polarimetric feature $I_t(x,y)$. A similar analysis can be derived for the geometrical case by considering the log-scale transform expressed in Eq. 5.7. Based on $W_{b(l)}$, three decomposition strategies are considered for the analysis: i) single-scale stationary wavelet transform, using L-size filters; ii) L-size spline stationary wavelet transform, using $(2L-1)$-size filters (SSW); and iii) discrete wavelet transform using L-size filters (MDW). The first approach considers the direct application of the definitions in Eq. 5.6 and 5.7 (see Fig. 5.1). Both the stationary-wavelet strategies do not apply decimation, so they may work for an arbitrary N. The multi-scale approach considers decimation step and requires N to be a power of 2. For different values of N, the temporal series is padded with element replicas, i.e., the final element. Details for the second and third approaches are given in the following subsections.

5.2.3 L-size Spline Stationary Wavelet transform (SSW)

In this approach, the L coefficients of the wavelet are considered for building a larger filter with size $2L-1$. The coefficients are defined based on the self convolution of the impulsive response of the filter. For the Haar-1 wavelet, the coefficients result in $W_A^{spl1} = \frac{1}{\sqrt{6}}[1,2,1,]$, $W_D^{spl1} = \frac{1}{\sqrt{6}}[1,-2,1,]$ for the approximation and the detail component, respectively (see Fig. 5.2). A single level of scale (i.e., $k=1$) is considered for this approach.

$$X_t^{(SSW_{a,1})} = \{X_t^{(SSW_{aA,1})}, X_t^{(SSW_{aD,1})}\} \tag{5.8}$$

$$X_t^{(SSW_{aA,1})} = W_A^{spl1} * \left[X_{(t-2)}, X_{(t-1)a}, X_{ta}\right] = \frac{1}{\sqrt{6}}\left(X_{(t-2)a} + 2X_{(t-1)a} + X_{ta}\right) \tag{5.9}$$

$$X_t^{(SSW_{aD,1})} = W_D^{spl1} * \left[X_{(t-2)}, X_{(t-1)a}, X_{ta}\right] = \frac{1}{\sqrt{6}}\left(X_{(t-2)a} - 2X_{(t-1)a} + X_{ta}\right) \tag{5.10}$$

being $X_t^{(SSW_{ab})}$ the component b obtained by arithmetic SSW transform on the feature X. One one hand, the approximation term corresponds to a weighted averaging of a set of

three consecutive terms, with the central pixel having more importance than the others. On the other hand, the detail term describes a difference of differences computed on subsequent values, thus it corresponds to a second derivative term, describing the change velocity.

5.2.4 Multiscale Discrete Wavelet transform with L-size filters (MDW)

In this approach, a multiscale analysis of the sequence is performed, with the iterative application of the wavelet filters on the approximation term $X_t^{(MDW_{aA,k-1})}$, which generates $X_t^{(MDW_{a,k})}$.

$$X_t^{(MDW_{a,k})} = \{X_t^{(MDW_{aA,k})}, X_t^{(MDW_{aD,k})}\} \tag{5.11}$$

For each feature X, the approach generates an approximation component $\{X_t^{(MDW_{aA,N})}$ at scale $N-1$ and set of detail components $X_t^{(MDW_{aD,0})}, ..., X_t^{(MDW_{aD,N})}\}$, being N the maximum scale of the analysis. For Discrete Wavelet transform, the filtering of the signal is followed by a sub-sampling step by a factor 2 and temporal wavelet sequences are halved at each scale level (see Fig. 5.3). For a Haar-1 wavelet, wavelet coefficients for the scale k are defined as follows.

$$X_t^{(MDW_{aA,k+1})} = \frac{1}{\sqrt{2}}\left(X_{2t-1}^{(MDW_{aA,k})} + X_{2t}^{(MDW_{aA,k})}\right) \tag{5.12}$$

$$X_t^{(MDW_{aD,k+1})} = \frac{1}{\sqrt{2}}\left(X_{2t-1}^{(MDW_{aA,k})} - X_{2t}^{(MDW_{aA,k})}\right) \tag{5.13}$$

5.3 Data processing

In order to prove the effectiveness of the proposed information representation for a time series of polarimetric images, a multi-temporal dataset of full-pol images with size 1024×1024 was considered. The dataset has been acquired by Radarsat-2 mission in the area of the Argentière glacier (France). It is composed by 7 full-polarimetric images acquired from January 29 to June 22, 2009, each with a geometrical resolution of 8 meters and incidence angle of 32°. The crop scene is a mountainside region, affected by seasonal changes associated to the variation of the snow content in the glacier area, and some minor abrupt changes, associated to avalanches.

For a quantitative assessment of the analysis, six local regions of interest were selected on the multi-temporal stack. Fig. 5.4a, 5.4b show the Pauli false color composite for the polarimetric images at times t_1, t_7, respectively and the regions of interest. In particular, the regions are associated to:

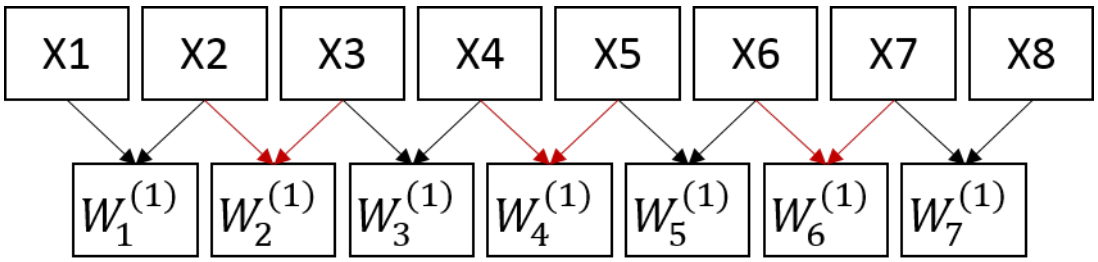

Figure 5.1: Example of Stationary wavelet based on Haar-1 family.

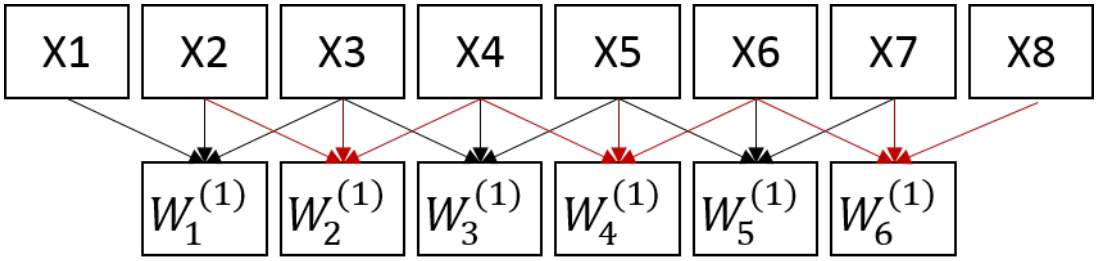

Figure 5.2: Example of Spline stationary wavelet of 3 elements based on Haar-1 family.

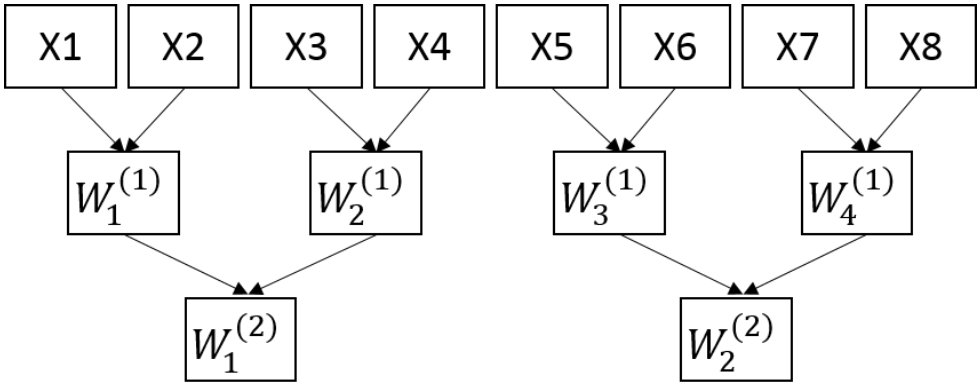

Figure 5.3: Example of multi-scale wavelet analysis based on Haar-1 family (2 levels).

- R1: area covered by an avalanche, which occurred between images 4 and 6;
- R2: accumulation area on the upper part of the Argentière glacier;
- R3-R4: northern/southern part of the Rognon glacier (heights $\sim 3300, 3600$ meters above sea level, respectively);
- R5-R6: ablation parts of Argentière glacier ($\sim 2400 - 2600$ meters above sea level, respectively).

Preliminary processing was conducted on the image set, with the radiometric calibration, the generation of the coherency matrix T and image despeckling for each image, respectively. The despeckling filter was selected as Refined Lee with size 7×7 [124; 122].

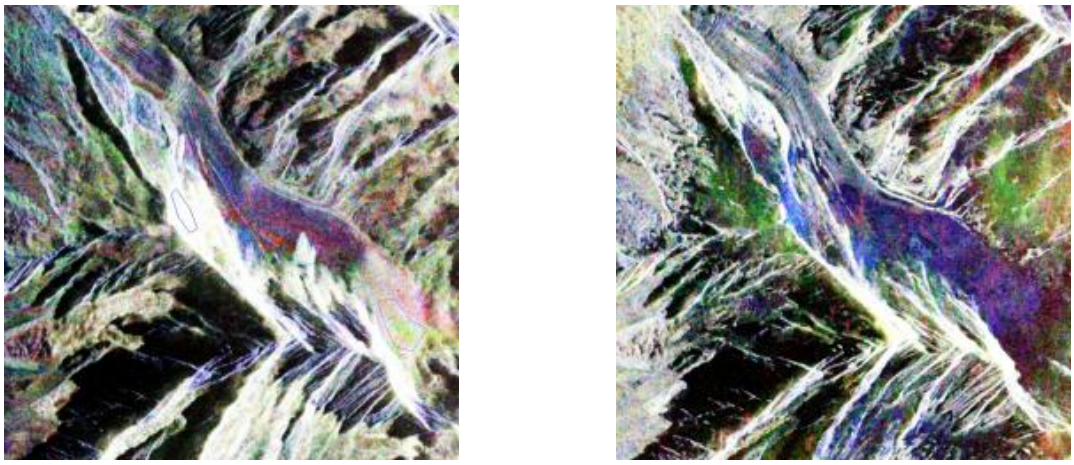

(a) (b)

Figure 5.4: Pauli false color composition for times t_1 (a) and t_7 (b); R1 - Cyan; R2 - Magenta; R3 - Green; R4 - Blue; R5 - Yellow; R6 - Red.

Polarimetric decomposition features have been derived based on the matrix T, namely H, A, α for the eigen-based decomposition and P_s, P_v, P_v, P_d for the power scattering-based decomposition, respectively. For a robust estimation, decomposition features were averaged on a local window with size 5×5, chosen as tradeoff between the scene homogeneity and the preservation of local edges.
The selection of either Geometrical and arithmetical framework was conducted for each of the polarimetric feature. Based on the optimal framework, the three strategies SW, SSW and MDW were tested on the set. In particular, the temporal set of each polarimetric feature X used in the MDW strategy was padded with image X_7.
A quantitative analysis was conducted on the set of regions of interest R1,..R6. A separation of the different natural multi-temporal classes was performed on the wavelet approx-

imation component, while the detection of the changes and the analysis of their temporal evolution was performed on the wavelet detail component. For the analysis of the approximation components, an Overall Class Separation Indicator $OCSI$ for the 6 classes was measured in order to define the optimal combination of wavelet strategy and polarimetric features for the class discrimination.

$$OCSI(w,X) = \sum_{c_1=1}^{6} \sum_{c_2 \neq c_1}^{6} \sum_{t} \frac{|\mu_{wXt}^{(c_1)} - \mu_{wXt}^{(c_2)}|}{\sqrt{\left(\sigma_{wXt}^{(c_1)}\right)^2 + \left(\sigma_{wXt}^{(c_2)}\right)^2}} \tag{5.14}$$

being $\mu_{wXt}^{c}, \sigma_{wXt}^{c}$ the mean and the standard deviation values computed on the region of interest c of the t-th image of the $w - X$ approximation component, respectively. The $OCSI$ is a cumulative temporal measure of the distance between the mean of pair of classes, scaled with the two corresponding standard deviations. The measure is averaged on all the pairs for the six classes. Best class separation is obtained by selecting the combination $w - X$ that maximizes the $OCSI$. In the analysis of the wavelet detail components, two parameters were defined, namely a dynamicity parameter δ, describing the total change occurring in the time series, and the change rate R_C evaluating the smoothness degree of the change.

$$\delta(w,X) = \sum_{c=1}^{6} \sum_{t} \left(\frac{\mu_{wXt}^{(c)}}{\sigma_{wXt}^{(c)}} \right) \tag{5.15}$$

$$R_C(w,X) = \sum_{c=1}^{6} \frac{\max_t \left(\frac{\mu_{wXt}^{(c)}}{\sigma_{wXt}^{(c)}} \right)}{\sum_t \left(\frac{\mu_{wXt}^{(c)}}{\sigma_{wXt}^{(c)}} \right)} \tag{5.16}$$

δ indicates an absolute measure of the total variation occurred. Large values of δ indicate presence of intense change activity in the time series, while small values tend to be associated to no-change regions. The change rate R_C is defined in the range $0 - 1$ and measures the part of the total change occurring in the time series associated to a single event. Thus it detects the presence of abrupt changes, occurring for large R_C Large values of δ correspond to pixels with large variability in the period of the time series and vice versa. R_C is defined in the range $(0 - 1)$. Small and large values are associated to smooth and abrupt changes, respectively.

5.4 Experimental results

For each feature, the use of either arithmetical or geometrical wavelet has been based on the prevalence of either additive or multiplicative noise, respectively. On one hand,

Table 5.1: Kullback-Leibler distance for the empirical distributions of eigenvalue-eigenvector decomposition features with Gaussian and Gamma ditribution.

Kullback-Leibler distance		
	Gaussian	**Gamma**
H	0.0380	0.0498
A	0.0108	0.0270
alpha	0.0309	0.0466

power scattering features are expected to be characterized by a dominant multiplicative noise, thus geometrical wavelet is considered as more suitable for it [12; 11]. On the other hand, eigen-based features present a complex model. Nonetheless, the features are related to the ratio of eigenvalues of T, which tend to follow a Gamma distribution [137] under simplifying assumptions, and their statistical distribution tend to a non-skewed Gaussian-like distribution. These considerations are confirmed by the KLD values of the eigen-based features with respect to the Gamma and Gaussian distributions (see Table 5.1). This favors the use of arithmetical wavelet in the analysis.
With the selected type of wavelet transform, both the SSW and MDW strategies have been analyzed for the two sets of polarimetric features. A single scale level (i.e., $k = 1$) has been considered for the MDW, because of the number of polarimetric images in the time series. A set of features $\{w - X\}, w \in \{\text{SW, SSW, MDW}\}, X \in \{f_s, f_d, f_v, f_h, \alpha, H, A\}$ has been derived from the temporal wavelet analysis with the three strategies. Given the use of $k = 1$, the features derived from the MDW correspond to a subset of those derived with the SW. The approximation and the detail components for the features $w - X$ were separately analyzed. The two analyses are presented in the following subsections.

5.4.1 Separation of multi-temporal classes

Fig. 5.5a-5.5f, 5.6a-5.6f, 5.7a-5.7h, and 5.8a-5.8h show the initial and the final images of the approximation component obtained with the temporal SW and SSW strategies for the two set of polarimetric features (i.e., (t_1, t_2),(t_6, t_7) and (t_1, t_2, t_3),(t_5, t_6, t_7) time sequences for the SW and the SSW, respectively). The SSW-H shows a decrease of entropy along the glacier strip and the area of the avalanche (see Fig. 5.6a, 5.6d). This variation may be probably determined by a seasonal increase of the wet snow content and the consequent increase of the surface scattering and the decrease of the other scattering mechanisms [159]. The accumulation region presents an increase for both the SSW-H and SSW-α components. Similar trend has been seen for the SSW-f_v (see Fig. 5.8c, 5.6d).

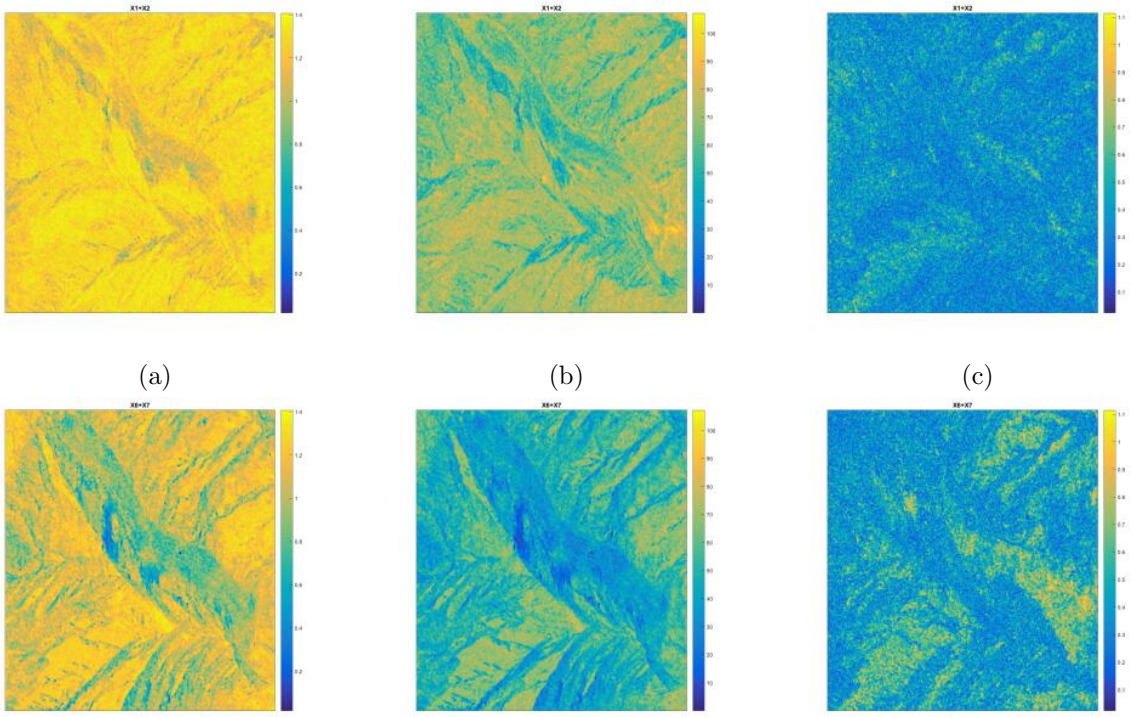

Figure 5.5: Images from the approximation component of SW-H, SW-α and SW-A, for t_1, t_2 (a,b,c) and t_6, t_7 (d,e,f), respectively.

These are probably related to the presence of fresh snow gradually accumulated during the season, which increase the volume scattering contribution and the two polarimetric eigen-features.

Moreover, a temporal increase of the image contrast with respect to the rocky mountainside facing the sensor, which shows no relevant changes, is registered by the SSW component (Fig. 5.6a-5.6f and 5.8a-5.8h). Different temporal trends are seen for R2,R3 and R5. Similar considerations are traced from the analysis of SW-based (and, thus, the MDW) features. However, compared to the SW, the SSW approximation components present a larger information stability, because of the different terms in the definition (5.9).

A local analysis has been conducted with the approximation components on the six regions of interest. Fig. 5.9a-5.9d show an example of the time trend on the different classes for the SW-H, SW-α, SW-f_h and SW-f_v, respectively. Class separation performance has been evaluated with $OCSI$. Table 5.2 reports the values obtained. Best performance are obtained with the use of SSW strategy and features from the power-based polarimetric decomposition, in particular with f_v and f_h.

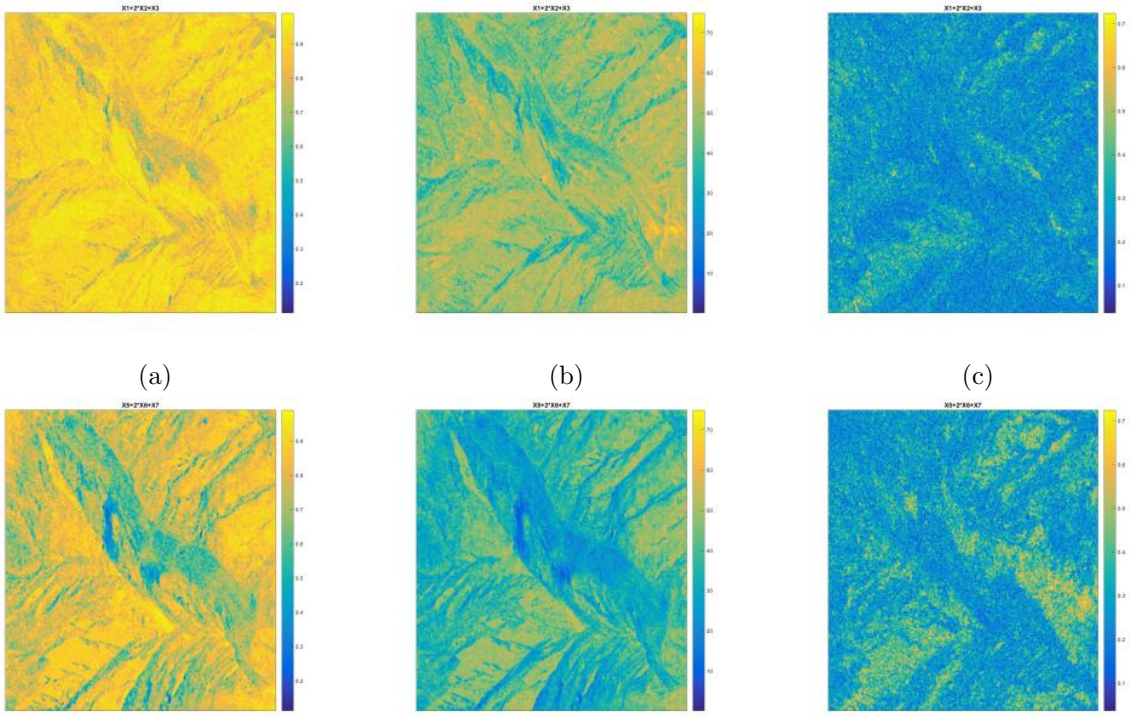

Figure 5.6: Images from the approximation component of SSW-H, SSW-α and SSW-A, for t_1, t_2, t_3 (a,b,c) and t_5, t_6, t_7 (d,e,f), respectively.

5.4.2 Change Detection and Evolution Analysis

Fig. 5.10a-5.10f, 5.11a-5.11f, 5.12a-5.12h, and 5.13a-5.13h shows the initial and the final images of the detail components with the temporal SW and SSW strategy, respectively. The detail components in the SW represent the change information, while those of the SSW map the change velocity, as they involve second-order variation. Positive and negative values in SW are associated to decrease and increase of the feature in the considered image pair, respectively. Because of the definition in 5.10, positive and negative values in the SSW are associated to the presence of a local minimum or maximum in the image triplet, respectively.

The SW components mapping the temporal pair t_1, t_2 do not show values sensibly different from zero (Fig. 5.10a-5.10c), while values different from zero are marked in the components of the pair t_6, t_7 (Fig. 5.10d-5.10f). This draws the changes as becoming more sensible with the temporal evolution. The detail components from SW-H and SW-α present positive and negative values on part of the upper part of the glacier and the accumulation region, respectively. Compared to the other eigen-based features, the SW-

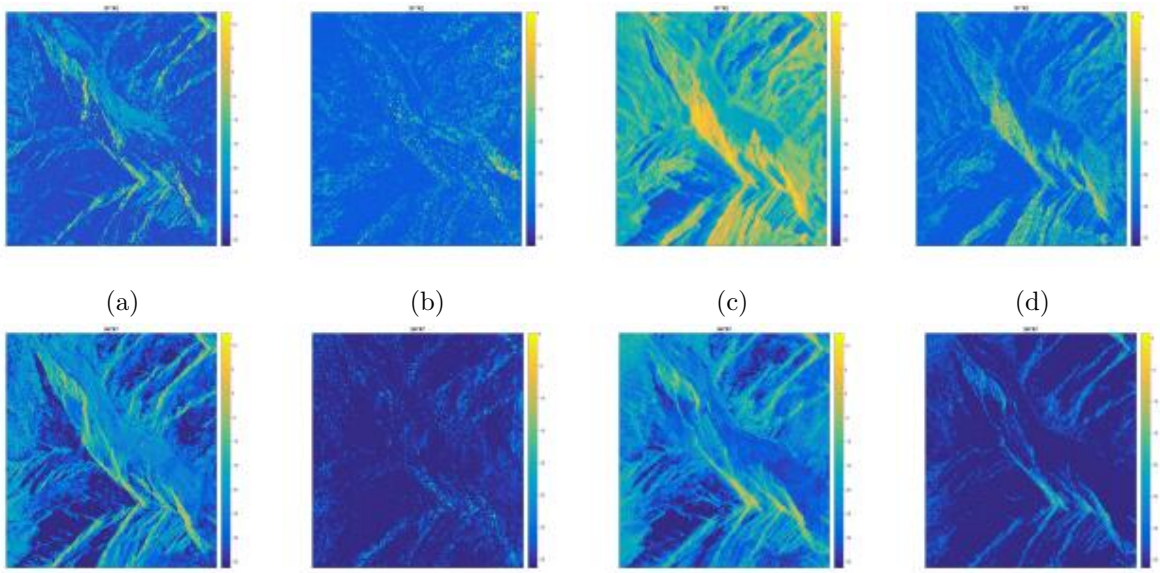

(a) (b) (c) (d)

(e) (f) (g) (h)

Figure 5.7: Images from the approximation component of SW-f_s, SW-f_d, SW-f_v and SW-f_h, for t_1, t_2 (a,b,c,d) and t_6, t_7 (e,f,g,h), respectively.

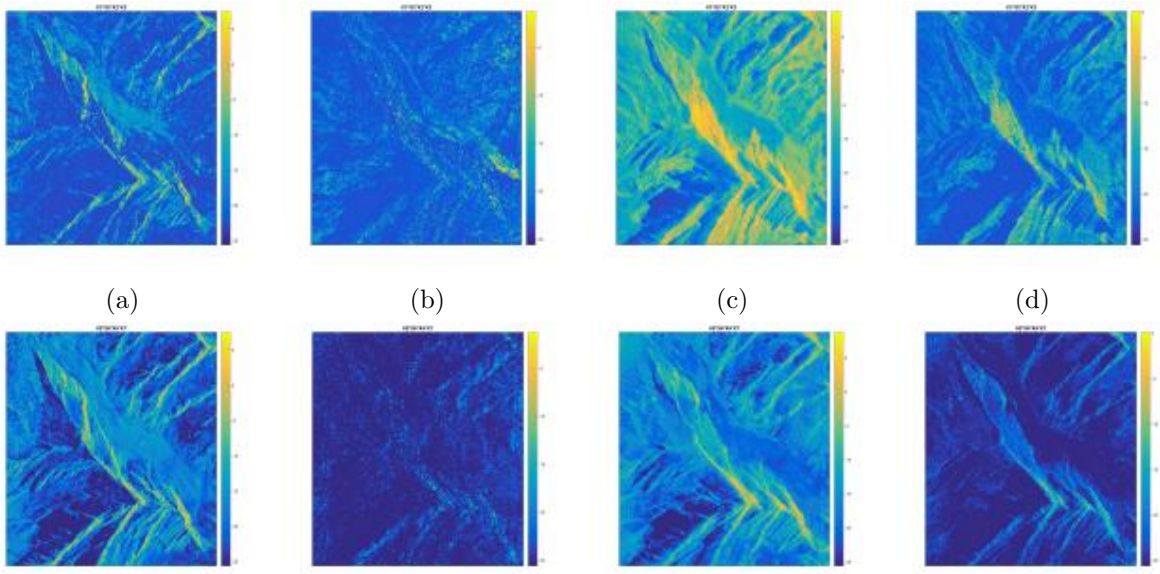

(a) (b) (c) (d)

(e) (f) (g) (h)

Figure 5.8: Images from the approximation component of SSW-f_s, SSW-f_d, SSW-f_v and SSW-f_h, for t_1, t_2, t_3 (a,b,c,d) and t_5, t_6, t_7 (e,f,g,h), respectively.

A component presents a larger variability, because of a large sensitivity on the window

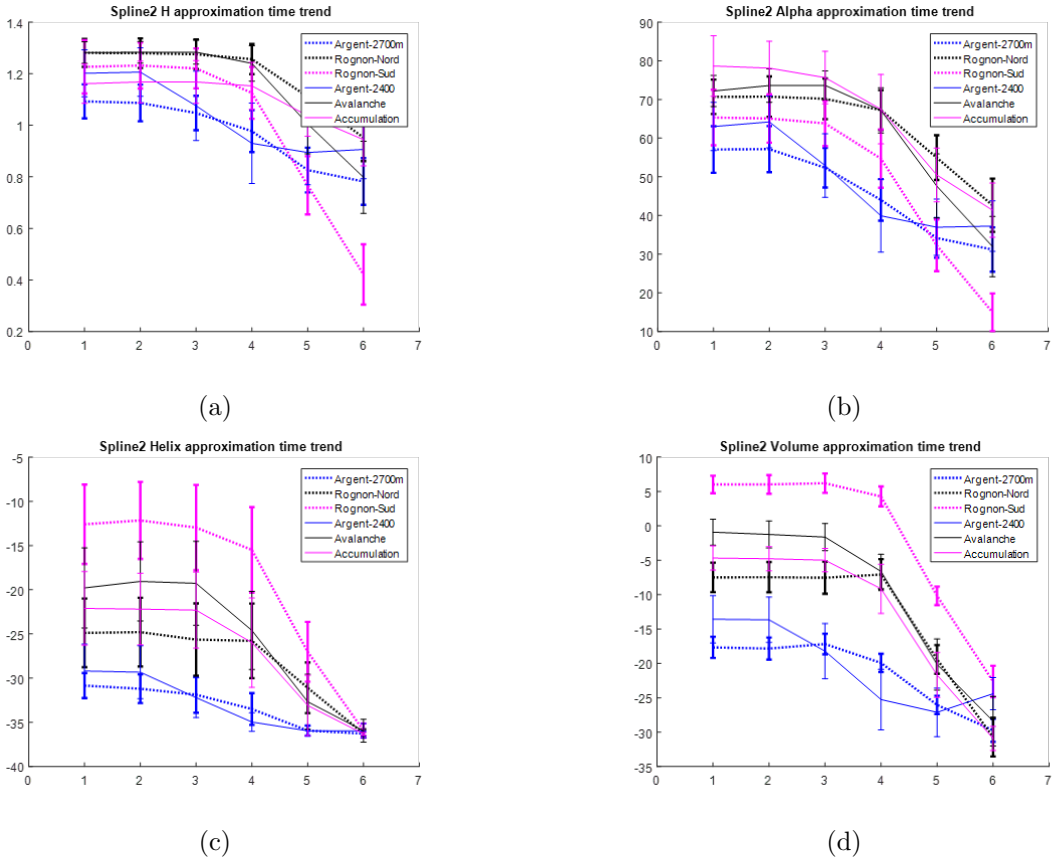

Figure 5.9: Temporal trend for the approximation component of: SW-H (a); SW-α (b); SW-f_h (c); SW-f_v (d).

Table 5.2: Performance analysis for overall class separation indicator, for different polarimetric features and wavelet strategies.

Overall Class Separation Indicator	**SW**	**SSW**	**MDW**
H	101.1425	87.7184	67.0577
A	37.3631	30.8456	25.4238
α	115.5167	102.6236	74.0808
Aggregate (Eigen-based)	84.6741	73.7292	55.5208
f_d	24.0888	20.5587	15.1726
f_h	114.4109	122.2092	68.6441
f_s	30.5785	78.1185	62.2078
f_v	284.6874	253.6868	171.4954
Aggregate (Power-based)	129.4414	118.6433	79.38

size used for the polarimetric decomposition. Poor information is also detected from the SW-f_d (Fig. 5.12b,5.12f) and SW-f_h (Fig. 5.12d,5.12h), while sensible value are detected for the SW-f_v (Fig. 5.12c,5.12g).
A local analysis has been conducted with the detail components on the six regions of interest. Fig. 5.14a-5.14d show an example of the time trend on the different classes for the SW-H, SW-α, SW-f_h and SW-f_v, respectively. For a quantitative analysis, δ and R_C have been compared for the different strategies and an overview of the results has been reported in Table 5.3 and Table 5.4, respectively. Largest values are seen for SW-f_h, SW-f_v and SW-α. This indicates a large total change occurred in the helix and volume scattering. Smaller values are detected for the other combinations of polarimetric features and wavelet strategies. Looking at the values R_C larger values are detected for f_h with both SSW and SW, indicating a more abrupt change in the helix power, compared to the others feature.

5.5 Conclusion

In this work, we analyzed the sensitivity of features based on the polarimetric decomposition and the temporal wavelet analysis for class discrimination and change detection. The

Table 5.3: Performance analysis for δ, for different polarimetric features and wavelet strategies.

Dynamicity	**SW**	**SSW**	**MDW**
H	3.4835	2.7232	2.2891
A	1.1174	0.9527	0.7635
α	4.4582	3.0593	2.7089
Aggregate (Eigen-based)	3.0197	2.2451	1.9205
f_d	2.2224	1.4850	1.2574
f_h	8.0742	5.1397	3.8863
f_s	2.4793	1.8746	0.7537
f_v	7.2983	6.9903	4.7206
Aggregate (Power-based)	5.0186	3.8724	2.6545

Table 5.4: Performance analysis for R_C, for different polarimetric features and wavelet strategies.

Change Rate	**SW**	**SSW**	**MDW**
H	0.5976	0.4709	0.8755
A	0.4974	0.4359	0.7167
α	0.4663	0.4210	0.7601
Aggregate (Eigen-based)	0.5204	0.4426	0.7841
f_d	0.3917	0.5709	0.6901
f_h	0.5546	0.6227	0.8994
f_s	0.3930	0.3824	0.5540
f_v	0.5784	0.4855	0.8752
Aggregate (Power-based)	0.4794	0.5154	0.7547

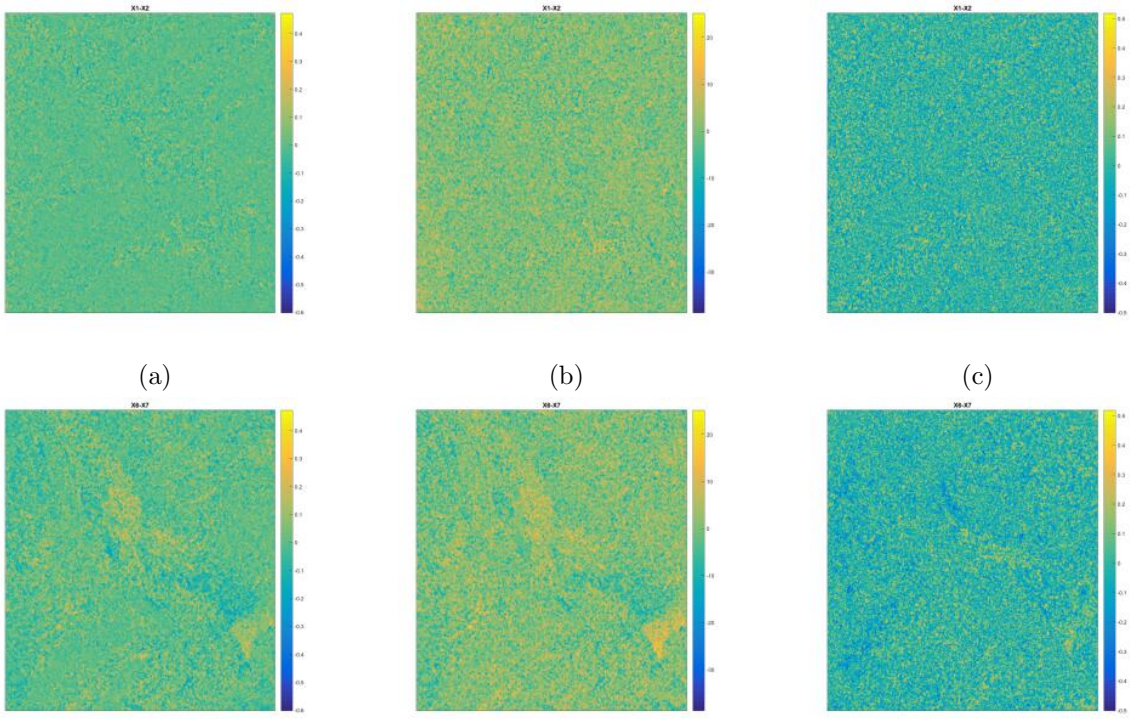

Figure 5.10: Images from the detail component of SW-H, SW-α and SW-A, for t_1, t_2 (a,b,c) and t_6, t_7 (d,e,f), respectively.

analysis considered a temporal series of full-polarimetric SAR images. Features derived from the state-of-the-art polarimetric decompositions and with the application of different wavelet strategies (i.e., SW, SSW, MDW) were considered for the analysis. Based on the characteristics of the single-time polarimetric feature, arithmetical and geometrical wavelet were alternatively selected in the analysis. The experimental analysis was conducted on a multi-temporal dataset describing the snow seasonal activities on the Argentière glacier area. Two experiments focused on the use of approximation and detail components for separation of multi-temporal classes and for detection of changes, respectively. Both the experiments analyzed multiple combinations of wavelet strategies and polarimetric features. They resulted in a robust performance for the volume and helix scattering power terms with the SW approach. Future developments consider the combination of features obtained from the application of different wavelet families (e.g., Symlet, Daubechies) in the temporal domain and the introduction of possible wavelet analysis in the spatial domain. They also aims introducing the proposed wavelet-based features in an unsupervised CD strategy.

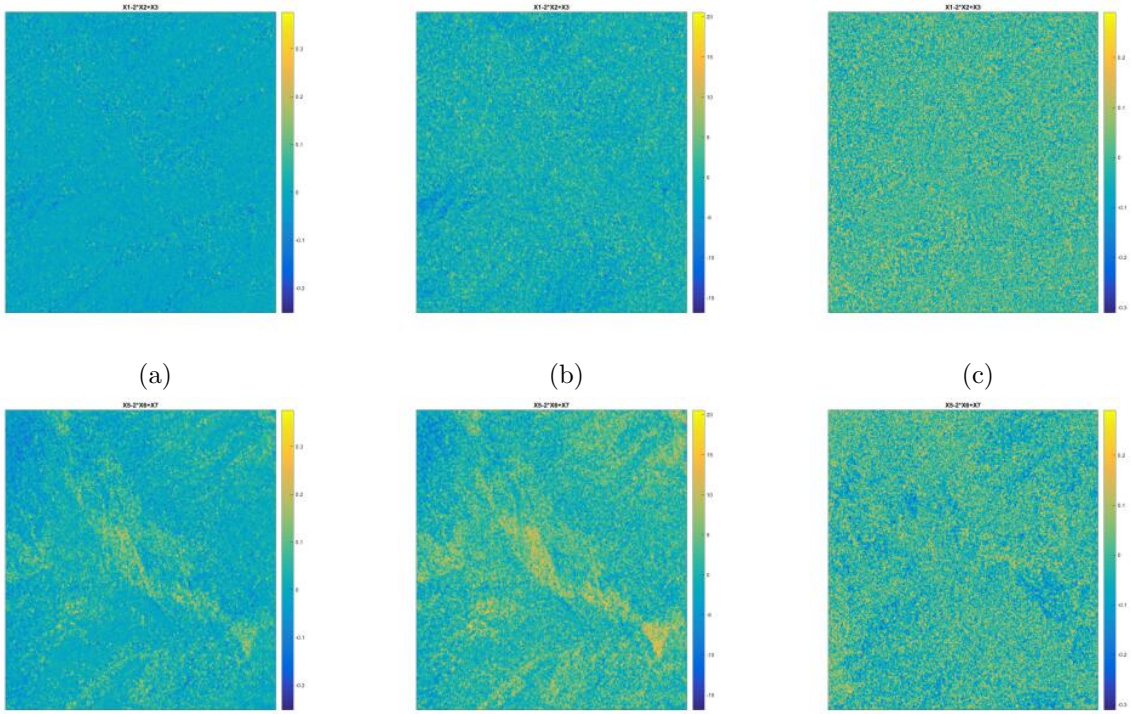

(a) (b) (c)

(d) (e) (f)

Figure 5.11: Images from the detail component of SSW-H, SSW-α and SSW-A, for t_1, t_2, t_3 (a,b,c) and t_5, t_6, t_7 (e,f,g), respectively.

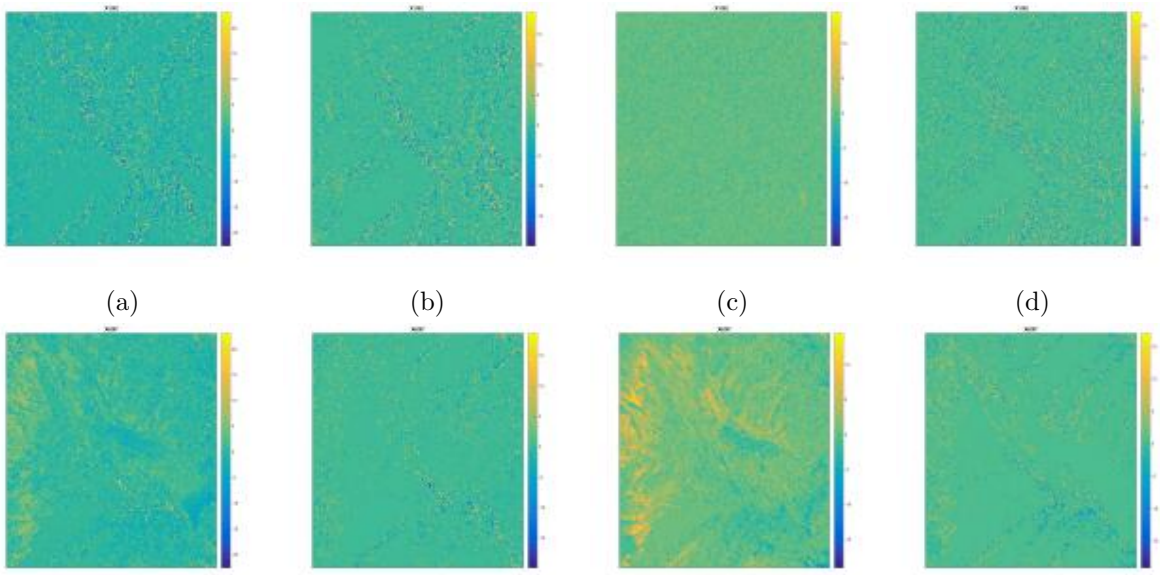

(a) (b) (c) (d)

(e) (f) (g) (h)

Figure 5.12: Images from the detail component of SW-f_s, SW-f_d, SW-f_v and SW-f_h, for t_1, t_2 (a,b,c,d) and t_6, t_7 (e,f,g,h), respectively.

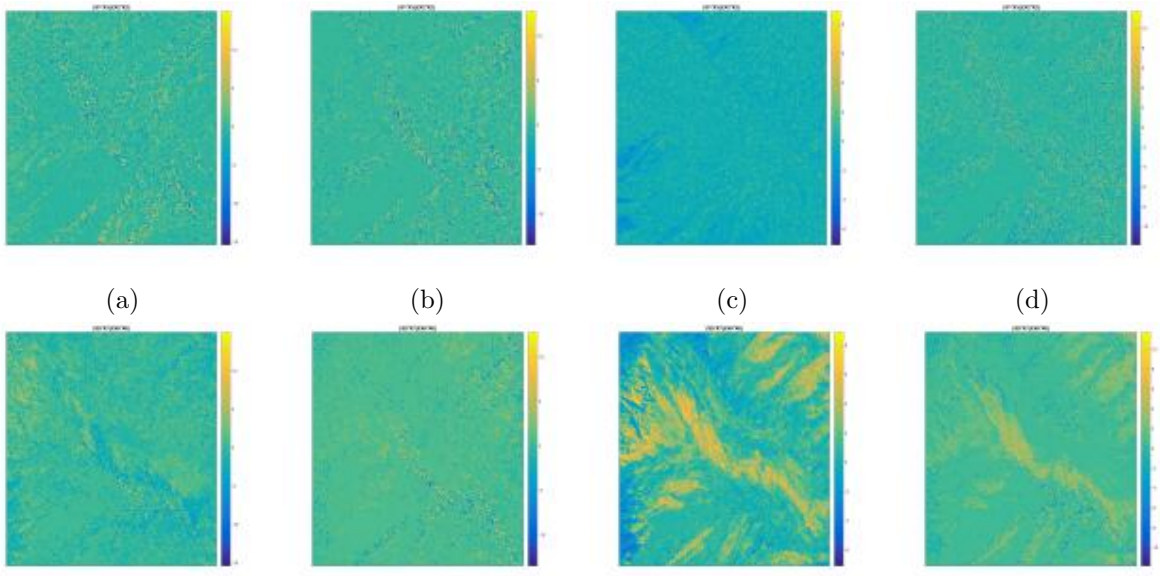

(a) (b) (c) (d)

(e) (f) (g) (h)

Figure 5.13: Images from the detail component of SSW-f_s, SSW-f_d, SSW-f_v and SSW-f_h, for t_1, t_2, t_3 (a,b,c,d) and t_5, t_6, t_7 (e,f,g,h), respectively.

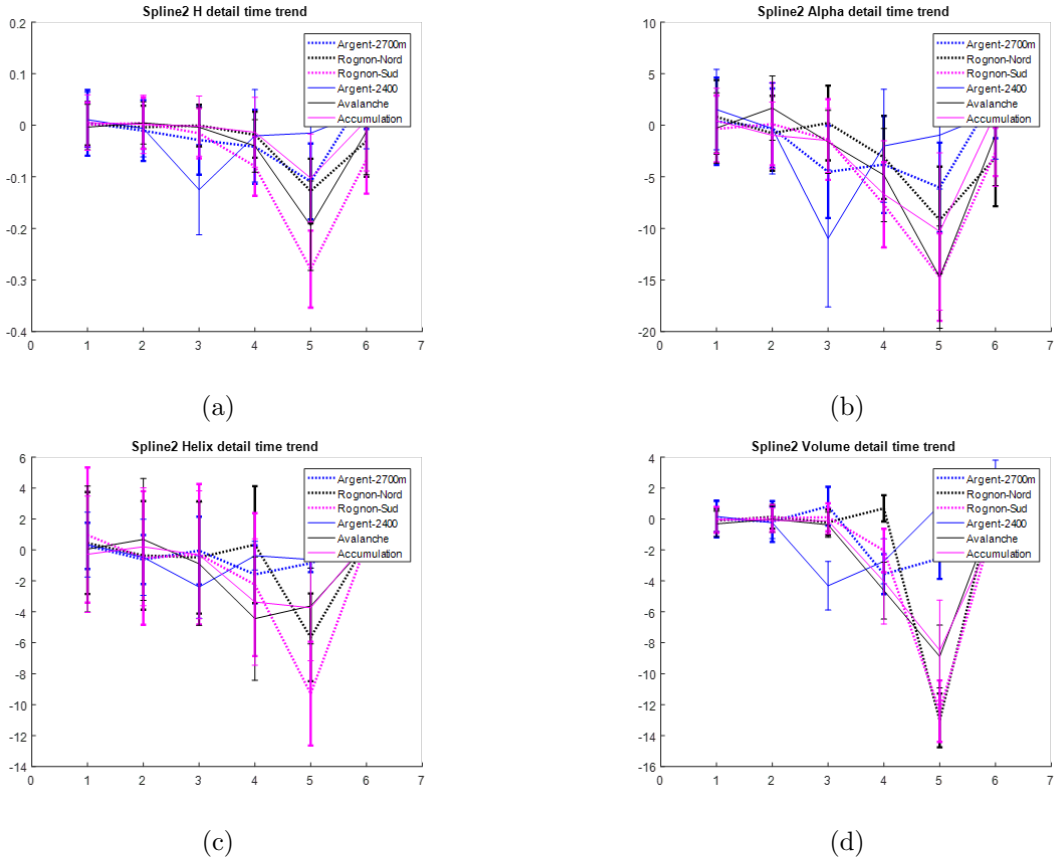

Figure 5.14: Temporal trend for the approximation component of: SW-H (a); SW-α (b); SW-f_h (c); SW-f_v (d).

Chapter 6

An Unsupervised Approach to Change Detection in Built-Up Areas by Multi-Temporal Full-pol SAR Images

Multi-temporal Synthetic Aperture Radar (SAR) data represent a precious supporting tool for quantifying changes in urban areas. Some SAR systems have acquisition capabilities at Very High Resolution (VHR), which allows the analysis at single-building scale. In this contribution, we aim at proposing a geometrical model for partially destroyed buildings, based on empirical observations, and derive the corresponding multi-temporal backscattering signature, by applying the ray-tracing method. We also integrate the model into an unsupervised automatic approach for the detection of both fully and partially destroyed buildings. The strategy considers a hierarchical structure of the changes. Experimental results conducted on two multi-temporal VHR SAR datasets show a large robustness of the approach and a good accuracy in the detection of the multiple classes of change in buildings. [1]

6.1 Introduction

Remote sensing imagery from Synthetic Aperture Radar (SAR) has proved a relevant role in multi-temporal analysis for Change Detection (CD), with multiple applications. Some of them focus on long-time phenomena [59; 66] and require image time series; others focus on sharp changes [33; 75; 94; 17] with a bi-temporal analysis. These applications may

[1] Part of this chapter appears in [170].

assume an evident importance in presence of urban areas and in case of abrupt events, natural hazards (e.g., flood [98] or earthquake [42]. SAR imagery maps scattering information and is affected by both geometrical distortions and speckle noise, which make the interpretation a complex task. However, SAR shows a low sensitivity to both weather and sunlight conditions, which makes it suitable for multi-temporal applications where some of the optical sensors may not perform well [143], as it guarantees acquisitions with a small temporal baseline.

Let us consider SAR systems acquiring scattering information with no polarimetric content (i.e., a single polarimetric channel). Among them, SAR systems can be characterized in terms of the different geometrical resolution. Many sensors present a geometrical resolution in the order of decades of meters (i.e., Medium Resolution, MR). However, some SAR missions, such as the in-operation TerraSAR-X or the forthcoming Cosmo-SkyMed Second Generation , have been equipped with enhanced imaging capabilities, showing a resolution down to the meter scale (i.e., Very High Resolution, VHR). Therefore, if the MR SAR imagery leads the analysis to a city block scale, VHR SAR imagery improves the analysis capabilities down to the building scale [150; 15; 44].

In the VHR SAR imagery, the scale highlights building structure elements with homogeneous regions based on the off-nadir SAR acquisition geometry [105]. However, the fine resolution increase the heterogeneity in the image, as the reduced number of scatterers in the resolution cell makes the speckle noise not fully developed [143].

Several works in the literature addressed the problem of CD in urban areas with VHR SAR data. They include the supervised analysis of backscattering patterns in the post-event SAR image [14; 99], the joint analysis of VHR SAR and optical data [44; 131; 63], the use of ancillary information coming from GIS layers with SAR data [9; 94] and the multi-temporal analysis of VHR SAR data in an unsupervised manner [146; 21; 98; 210; 113; 17; 154; 136]. In the latter case, the data complexity makes the pixel- and region-based approaches used for MR data not completely reliable for the CD analysis, thus an analysis based on a higher semantic level was conducted in [177; 146]. This analysis requires the definition of an object backscattering model for associating a label of changed buildings to changes in the scattering properties. Several models have been presented in the literature. Some of the building models aim at preserving the radiometric information, by means of an accurate backscattering analysis based on both the physical properties of the surfaces and the scattering propagation [88]. Others are devoted to the preservation of the geometrical accuracy, by using the ray-tracing method, which is based on optical rays for scattering propagation [13; 83; 41].

Because of the size of the change, a large interest in the literature has been devoted to the detection of building changes with size comparable to the typical size of the building [146].

These are namely the changes from no building to a complete standing building (i.e., *new building*), and the change from a complete standing building to no-building (i.e., *fully destroyed building*). In spite of the effort for the detection of completely changed buildings, a minor effort has been spent in tackling the detection of building changes with size smaller than the entire building size, mainly considering visual inspection of the operator with signatures from SAR simulators or geometrical models [119; 170; 15; 217]. These changes normally occur in presence of damaged buildings keeping part of the structure intact (i.e., *partially damaged buildings*). Nevertheless, these changes have the same relevance as the ones associated to entire buildings and, if considered, together may provide enhanced information for rescue and emergency services.

In this chapter, we aim at proposing a model for multi-temporal backscattering analysis over partially damaged buildings. In particular, the model is based on geometrical assumptions on the shape of both the building and the damage. A backscattering analysis based on the ray-tracing method in single time is conducted on the target (i.e., the partially destroyed building), by varying the possible geometrical conditions and/or the acquisition geometry. The multi-temporal backscattering signature of the target is hence derived by applying one of the standard SAR comparison operators. Compared to the multi-temporal model for the fully destroyed building, the multi-temporal model for partially destroyed buildings show a more complex pattern, with multiple homogeneous regions. Furthermore, the set of regions in the pattern is partially affected by the geometrical parameters of the damage. In order to identify an expected typical behavior for the multi-temporal model, a sensitivity analysis is conducted by varying the geometrical parameters and common elements of the multi-temporal backscattering patterns are inferred and evaluated.

We also aim at integrating the novel model for the partially damaged building in an automatic unsupervised CD strategy for the detection of both fully and partially destroyed buildings. The strategy exploits a hierarchical rationale, based on the different expected size of the changes, for separately identifying the fully and partially destroyed buildings. A map of backscattering changes is derived by comparing the multi-temporal VHR SAR images and applying Bayesian thresholding. Both the kinds of building changes are individuated from the backscattering variation by considering the possible candidates, based on the expected change size. For each candidate, spatial properties of the pattern are evaluated based on the expected multi-temporal scattering model. These properties are evaluated through fuzzy membership functions in order to measure the goodness of the building candidate.

This chapter is structured as follows. Sec. 6.2 presents the single-time scattering behavior for the building for different conditions (i.e., standing, fully and partially destroyed). In

Sec.6.3 the single-time patterns are compared for describing the multi-temporal scattering behavior associated to both the fully- and partially-destroyed building. In Sec. 6.4 the proposed automatic strategy for the detection of the different building classes from multi-temporal VHR SAR data is described. In 6.5 experimental results are illustrated. Finally, in 6.6 conclusions and final remarks for future developments are traced.

6.2 Building scattering model in single-time VHR SAR images

In this section, a single-time scattering model is presented for the building under different damage conditions. We recall models for both standing and fully destroyed buildings from the literature [83; 146]. Based on the same paradigm, a novel geometrical model for a partially-destroyed building and corresponding scattering pattern is derived. Let us consider a flat-roof building with rectangular shape. Let H, W, L be its height and planar dimensions, respectively. Let θ be the incidence angle of the sensor. For typical radar imaging missions, θ is a value in $[20°, 55°]$. The building is considered as generally rotated with respect to the range-azimuth plane, with orientation angle ϕ defined between the segment W and the range direction. ϕ ranges in the interval $[-\pi, \pi]$. The scattering model is based on some simplifying assumptions about the problem geometry and the application of the ray-tracing method. The first assumption considers no perturbations from external elements on the building scattering signature (i.e., isolated building). The second assumption considers a structure with fixed height along one or both planar dimensions. The ray-tracing method considers building slices along ground range and scattering propagation with linear trajectories. The scattering terms are grouped into surface scattering and additive multi-bounce contributions, associated to either the surface targets or the corner reflectors, respectively. The building scattering analysis is conducted by first assuming the case of $\phi = 0$. The assumption is later removed and the analysis for the general case $\phi \neq 0$ is conducted. Each scattering analysis separately focuses on the surface scattering and additive multiple bounce contributions.

6.2.1 Standing Building

Let us assume that the building is aligned to the range direction (i.e., $\phi = 0$). In the analysis of the backscattering signature, we apply the ray-tracing method and consider building slices (green rectangles in Fig. 6.1a) along the range direction. Each slice is characterized by a width W and a height profile h assuming value H on the building. For $\phi = 0$, L_R coincides with the planar dimension in range (i.e., $L_R = W$) and all the slices show the same behavior.

Surface scattering: The scattering contributions are considered from different building

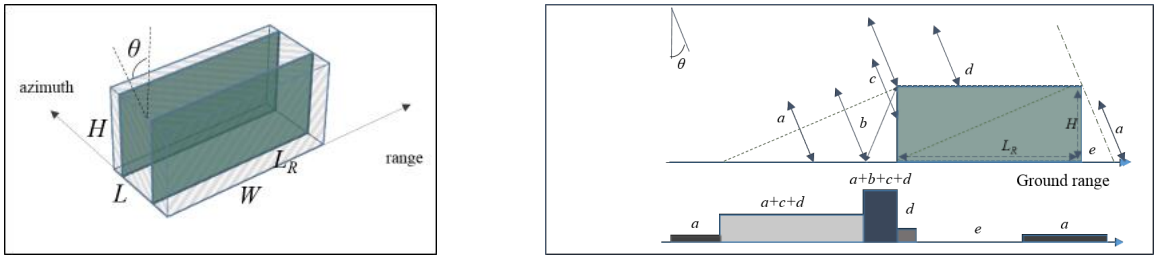

(a) (b)

Figure 6.1: Standing building: (a) acquisition geometry and building slices for $\phi = 0$; (b) backscattering signature for a single slice, $L_R \geq L_{RT}$. Scattering terms: a (ground), b (double bounce), c (wall), d (roof), e (shadow).

elements, namely the ground (a), the vertical wall (c) and the roof (d). The SAR system senses the target with incidence angle θ and this introduces layover and shadow effects for the contributions, with terms $a+c+d$ and e, respectively. Fig. 6.1b gives an example of the global backscattering signature for the single building slice. Two signatures for the surface scattering are possible, depending on the value of L_R compared to a threshold L_{RT} [44; 146; 83]. L_{RT} is defined in terms of the building height (H) and the incidence angle (θ), as follows:

$$L_{RT} = H \cot \theta \tag{6.1}$$

For $L_R \geq L_{RT}$ the layover and the shadow regions are separated by a region of scattering from the roof d. For $L < L_{RT}$, a second layover region exists, with value $a + c$. Table 6.1 indicates the sequence of surface scattering regions seen from near- to far-range for the two cases.

Table 6.1: Homogeneous surface-scattering regions for standing building scenario

Case	*Geometrical condition*	*Surface scattering contributions (near- to far-range)*
1	$L_R \geq L_{RT}$	$a + c + d; d; e$
2	$L_R < L_{RT}$	$a + c + d; a + c; e$

Multi-bounce contributions: A double-bounce contribution b_{wg} is created by the corner reflector formed by the standing wall (w) and the ground (g). This contribution is reflected to the sensor with angle θ [200]. For the sake of simplicity, we assume the effect of the orientation angle on the multiple bounce contributions negligible [87]. In order to model the amplitude of the different pattern regions, terms a, c and d are modeled by assuming

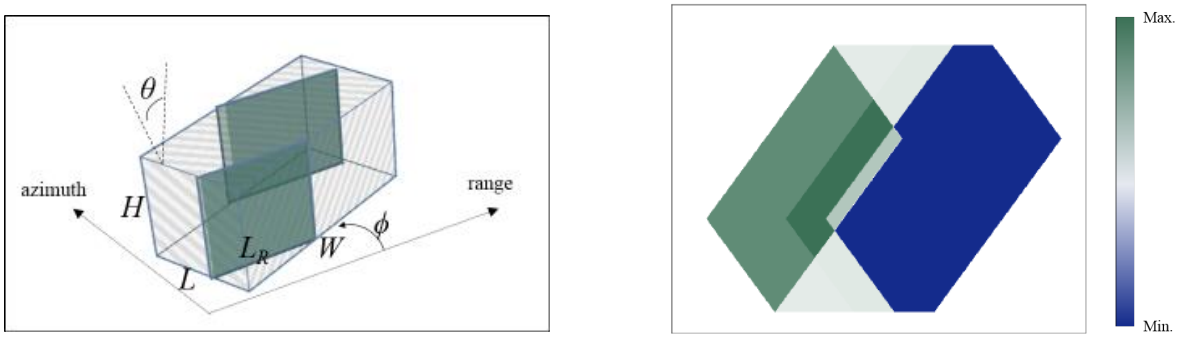

(a) (b)

Figure 6.2: Standing building with $\phi \neq 0$: (a) acquisition geometry and building slices; (b) example of backscattering pattern for a standing building, with $W > H\cot\theta$, $\phi = \pi/4$, ($K_a = 0.2, K_c = K_d = 5$).

Lambert law for the radiation, as follows:

$$s = K_s \cos^2(\hat{\theta}), s \in \{a, c, d\} \tag{6.2}$$

being $\hat{\theta}$ the angle between the surface normal and the scattering direction (i.e., $\hat{\theta} = \theta$ for a, d and $\hat{\theta} = \pi/2 - \theta$ for c terms, respectively). On the other hand, a simple model for b_{wg} has been considered, by assuming fixed surface albedo for both wall and ground surfaces.

$$b_{wg} = K_a K_c \cos^2\theta \sin^2\theta \tag{6.3}$$

Let us now remove the assumption of $\phi = 0$ and consider a general value of ϕ. For a general ϕ value, each slice has width L_R and a height profile with value H on the building, and zero outside. L_R depends on the azimuth position, the building size and building orientation. Figure 6.2a illustrates the acquisition geometry and the slices (green rectangles) for an oriented building. Slices with $L_R \geq L_{RT}$ present a backscattering signature as described in Case 1 of Table 6.1. Conversely, those with $L_R < L_{RT}$ present a backscattering signature as described in Case 2 of Table 6.1. Additive double-bounce contribution b_{wg} is introduced in the scattering signature by the corner reflector on each slice [146]. By considering all the slices and superimposing surface scattering and multiple-bounce contributions, a two-dimensional backscattering pattern is derived for the standing building. Fig. 6.2b shows an example of the two-dimensional backscattering pattern for $\phi = \pi/4$.

6.2.2 Fully Destroyed Building

For every orientation angle, the fully destroyed building presents a backscattering signature with surface scattering contributions from the ground (a) and the uncovered bare

soil (f), with similar values. No multiple-bounce contributions are present. Thus, the backscattering signature can be considered as almost constant over range and azimuth [146].

6.2.3 Partially Destroyed Building

Let us assume the same building described in Sec.6.2.1. Different kinds of partial damage can be defined, each affecting a limited parts of the structure. In this work, the analysis is focused on the fall of one of the satellite facing facades in near range [170]. Since the facades in far range are occluded because the geometrical distortions of SAR images, damages located in the far range need images acquired in complementary acquisition direction. For the sake of simplicity, the geometrical model is assumed to have constant height along the direction determined by L. The fallen part of the building is defined by height H, slope α and range and azimuth dimensions $\Delta W, L$, respectively. The fall produced a debris with surface slope α with respect to the nadir and range and azimuth dimensions $(H - \Delta H_H)\tan\alpha, L$, respectively. Moving to far range, the debris is followed by the undamaged part of the building, with height H and range and azimuth dimensions $W - \Delta W, L$, respectively. Under the simplifying assumption that volume is preserved while the building is falling down, the three parameters $\{\alpha, \Delta H_H, \Delta W\}$ satisfy the following equation:

$$\Delta W = \frac{(H - \Delta H_H)^2}{2H}\tan(\alpha) \tag{6.4}$$

Each slice of the building is characterized by a width parameters L_R and ΔL_R for the original undamaged building and the damaged part, respectively, and a height profile h. For $\phi = 0$, $L_R = W, \Delta L_R = \Delta W$, while h keeps the same height profile for all the slices (green rectangles in Fig. 6.3a), namely a ramp rising from 0 to $H - \Delta H_H$, with constant slope $\pi/2 - \alpha$, on the damaged part and a constant value H on the non-damaged part, respectively. Each slice show the same scattering behavior.

Surface scattering: Because of the off-nadir acquisition angle θ, the missing layover from the fallen part shifts the signature to far-range. The scattering contributions are considered from both building and debris elements, namely ground (a), the vertical part of the wall (c_w), the debris surface (c_d) and the roof (d). Fig. 6.3b illustrates an example of the surface scattering for the single slice of a partially-destroyed building for $\phi = 0$. The slice signature is characterized by the presence of layover and shadow effects, with regions $a + c_w + d$, e respectively. The two regions are separated by two scattering regions depending on the the value of L_R compared to thresholds L_{RT1}, L_{RT2}. L_{RT1}, L_{RT2}, defined in terms of the incidence angle θ and damage parameters $\alpha, \Delta L_R, \Delta H_H$, as follows.

$$L_{RT1} = \Delta L_R + \Delta H_H \cot\theta \tag{6.5}$$

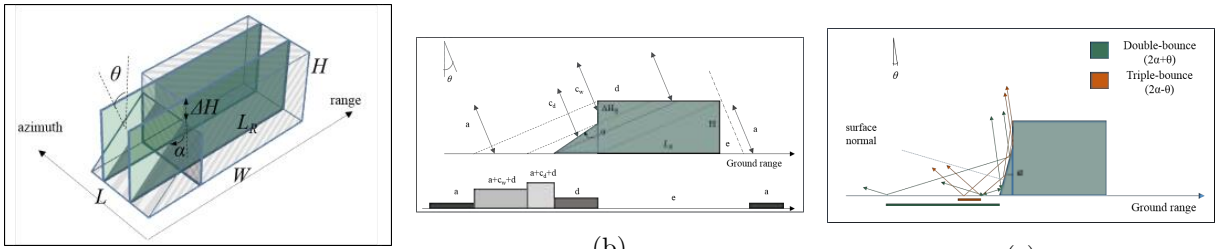

(a) (b) (c)

Figure 6.3: Partially destroyed building: (a) Acquisition geometry and building slices for $\phi = 0$; (b) Backscattering signature with surface scattering contributions for a single slice based on the ray-tracing method, $L_R \geq L_{RT2}$. Scattering terms: a (ground), c_w (wall), c_d (debris), d (roof), e (shadow).

$$L_{RT2} = \Delta L_R + H \cot\theta - (H - \Delta H_H) \tan\alpha \tag{6.6}$$

For $L_R \geq L_{RT2}$ the two regions are separated by a layover region $a + c_d + d$ and a region of scattering from the roof d. On the other hand, if $L < L_{RT1}$, the two regions are separated by two layover regions with values $a + c_w$ and $a + c_d$, respectively. Intermediate cases (i.e., $L_{RT1} \leq L_R < L_{RT2}$) consider two layover regions with values $a + c_d + d$ and $a + c_d$. The geometrical conditions and the corresponding backscattering regions for a single slice are summarized in Table 6.2.

Table 6.2: Surface scattering contributions for partially-destroyed building.

Case	*Geometrical condition*	*Surface scattering contributions (near- to far-range)*
1	$L_R \geq L_{RT2}$	$a; a + c_w + d; a + c_d + d; d; e$
2	$L_{RT1} \leq L_R < L_{RT2}$	$a; a + c_w + d; a + c_d + d; a + c_d; e$
3	$L_R < L_{RT1}$	$a; a + c_w + d; a + c_w; a + c_d; e$

Multi-bounce contributions: The presence of the debris surface both reduces the double-bounce region associated to the corner reflector and introduces two possible multi-bounce contributions, derived according to geometrical considerations [200]. These contributions may either exist or not depending on the parameters $\theta, \alpha, H, \Delta H_h$. The first one is the double bounce b_{dg} (green color in Fig. 6.3c) related to the interaction of the debris (d) and the ground (g), which is reflected to the sensor with an angle $2\alpha + \theta$. The second contribution is the triple bounce b_{wdg} (orange color in Fig. 6.3c) related to the interaction among the vertical part of the wall, the debris and the ground, which is reflected to the sensor with an angle $2\alpha - \theta$. Both angles are assumed in the interval $(0; \pi/2)$. A negligible

effect of the orientation angle ϕ on all the multiple-bounce contributions is assumed. The possible cases are summarized in Table 6.3. Terms a, c_d, c_w and d are modeled by assuming

Table 6.3: Multi-bounce contributions for partially-destroyed building.

Case	*Geometrical condition*	*Multi-bounce contributions (near- to far-range)*
1	$\theta \geq \alpha$	Double bounce from vertical wall (θ);
		Double bounce from debris ($2\alpha + \theta$);
2	$\begin{cases} \theta < \alpha \\ H \tan\theta \geq (H - \Delta H_H) \tan\alpha \end{cases}$	Double bounce from vertical wall (θ)
		Double bounce from debris ($2\alpha + \theta$);
		Triple bounce ($2\alpha - \theta$).
3	$\begin{cases} \theta < \alpha \\ H \tan\theta < (H - \Delta H_H) \tan\alpha \end{cases}$	Double bounce from debris ($2\alpha + \theta$);
		Triple bounce ($2\alpha - \theta$).

Lambert law for the radiation.

$$s = K_s \cos^2(\hat{\theta}), s \in \{a, c_d, c_w, d\} \tag{6.7}$$

being $\hat{\theta}$ the angle between the surface normal and the incidence direction (i.e., $\hat{\theta} = \theta$ for a, d, $\hat{\theta} = \pi/2 - \theta$ for c_w and $\hat{\theta} = \pi/2 - \theta - \alpha$). Because of the similar material, debris and the wall are assumed to have similar dielectric properties and coefficients K_{c_d}, K_{c_w} (i.e., $K_{c_d} \simeq K_{c_w} = K_c$). On the other hand, the amplitude of the multi-bounce contributions is modeled by assuming constant surface albedo for the involved surface elements, as follows.

$$b_{dg} = K_a K_c \cos^2(2\alpha + \theta) \sin^2(\alpha + \theta) \tag{6.8}$$

$$b_{wdg} = K_a K_c^2 \cos^2(2\alpha - \theta) \sin^2(\alpha - \theta) \tag{6.9}$$

By considering all the slices and superimposing surface scattering and multiple-bounce contributions, a two-dimensional scattering pattern is derived for the partially-damaged building.

Let us now remove the assumption and consider a general angle $\phi \neq 0$. To constrain the damage to the satellite-facing facade, ϕ is limited to the interval $[-\pi/2, \pi/2]$. Other values refer to a building with damages on one of the occluded facades. Without loss of generality, we focus the analysis for positive ϕ values. The patterns for the corresponding negative values can be easily derived by flipping the pattern with respect to the ground range. The building slices are now characterized by width L_R and height profile h, depending on the azimuth position, the geometrical parameters and the orientation angle. Furthermore, the

debris on the slices is characterized by a slope angle $\pi/2 - \beta$ with respect to the vertical direction that depends on the value of ϕ.

$$\beta = \arctan(\cot\alpha \cos\phi) \tag{6.10}$$

In particular, four kinds of height profile can be associated to h for the general case, namely profile A, B, C and D. Each of the height profiles can be described together with its backscattering analysis, derived by applying the ray-tracing:

- *profile A* (yellow in Fig. 6.4): the slice only includes the debris. h assumes values rising from 0 to $W \cot\beta$ with constant slope $\pi/2 - \beta$. The corresponding backscattering signature is composed by contributions a and c_d, respectively. Layover of the two contributions occurs for $\beta < \pi/2 - \theta$ values.

- *profile B* (dark green in Fig. 6.4): depending on the value of ϕ, the profile has two possible behaviors. For small values of ϕ (i.e., $\phi \leq \phi_0$), the slice includes both the debris and the undamaged part. h assumes values rising from 0 to $H - \Delta H$ with constant slope $\pi/2 - \beta$ associated to the near-range debris and constant value H on the far-range undamaged part of the building. In this case, the backscattering signature is characterized by surface scattering and multiple bounce contributions as described in the analysis for $\phi = 0$, with a surface slope β for the slice.
  Conversely, for large values of ϕ (i.e., $\phi > \phi_0$), the slice only includes the debris and height profile assumes values rising from a positive value h_0 to $h_0 + L_R \cot\beta$ with constant slope $\pi/2 - \beta$ being $h_0 \in [0, H - \Delta H_H - L_R \cot\beta]$. The corresponding backscattering signature is similar to that in Table 6.1, with a region of layover $a + c_d + c_w$ and a region of shadow e. Two possible multi-bounce contributions, with

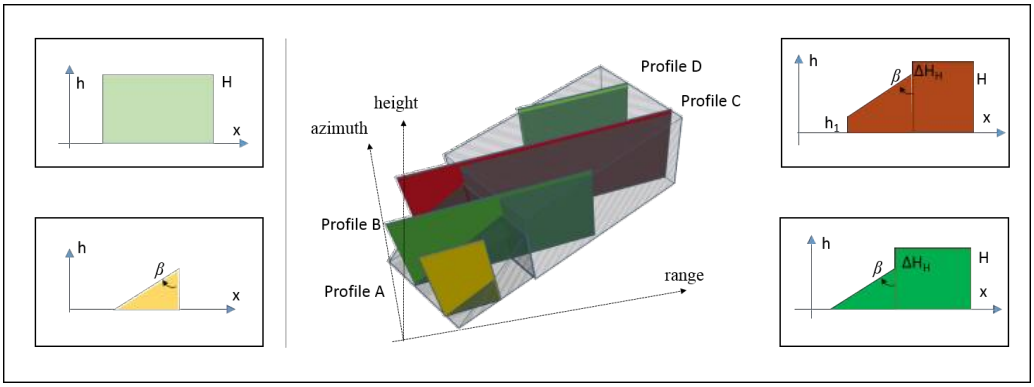

Figure 6.4: Example of acquisition geometry of partially destroyed building for $\phi \neq 0$ and building slices. Aspect angle effect generates four profiles, namely A (yellow), B (dark green), C (red) and D (light green).

angles θ and $2\alpha+\theta$, are associated to the corner reflector of h_0 and the debris slope, respectively. ϕ_0 is derived based on geometrical considerations, as follows.

$$\phi_0 = \arcsin\left[\frac{L_A\cos\phi}{(H-\Delta H_H)\tan\alpha\sin\phi}\right] \tag{6.11}$$

- *profile C* (red in Fig. 6.4): the slice includes both the debris and the undamaged part and the height profile assumes values rising from h_1 to $H-\Delta H$ with constant slope $\pi/2-\beta$ associated to the near-range debris and a constant value H on the far-range undamaged part of the building, $h_1 \in [H-\Delta H_H - L_R\cot\beta; H-\Delta H_H]$. For the corresponding backscattering signature, same considerations traced above for $\phi=0$ hold. Two further contributions are associated to the positive value h_1, namely a decrease of the size along range of the regions associated to the c_w contribution and a double bounce region associated to the part of the debris with height h_1.

- *profile D* (light green in Fig. 6.4): the slice includes only the undamaged part. The backscattering signature is derived based on the considerations for the standing building slices in Sec. 6.2.1.

By considering all the slices and superimposing surface scattering and multiple-bounce contributions, a two-dimensional backscattering pattern is derived for the partially-destroyed building. Fig.6.5 shows an example of two-dimensional backscattering pattern for $\phi = \pi/4$, with damage parameters $\alpha=\pi/6, \Delta H_H = H/4$.

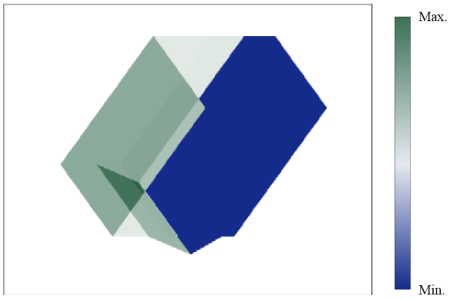

Figure 6.5: Example of backscattering pattern for a partially destroyed building for $\phi = \pi/4, \Delta H_H = H/4, \alpha=\pi/6$ ($K_a=0.2, K_c=K_d=5$).

6.3 Building scattering model in multi-temporal VHR SAR images

Based on the single-time scattering models derived in Sec. 6.2, a multi-temporal analysis for the building damage assessment is conducted by comparing the patterns in pre- and

post-event. The expected behavior for the multi-temporal pattern can be characterized by defining peculiar geometrical features on the change regions of the multi-temporal scattering pattern. Two possible damage situations are considered. The first situation considers the complete destruction of building, by comparing patterns for standing and fully destroyed building associated to pre- and post-event, respectively. The second situation is associated to the partial destruction of the building, with patterns for standing and partially destroyed building associated to pre- and post-event, respectively. The multi-temporal comparison highlights presence of areas with scattering increase (ω_I), decrease (ω_D) or no change (ω_{nc}) of scattering.

6.3.1 Fully destroyed buildings

For a fully destroyed building, the multi-temporal comparison generates a pattern with a large increase region R_I and multiple adjacent decrease regions (Fig. 6.6a). The increase region is associated to the disappearance of the building shadow in far range. The decrease regions are associated to the disappearance of the different scattering contributions associated to the building structure in near range. For sake of simplicity in the multi-temporal analysis, adjacent decrease regions are grouped into a single region R_D. The opposite situation, describing the appearance of a new building, can be described in the multi-temporal analysis an increase region in near-range and decrease region in the far-range, respectively. R_D is characterized by area S_D and length l_D along the azimuth

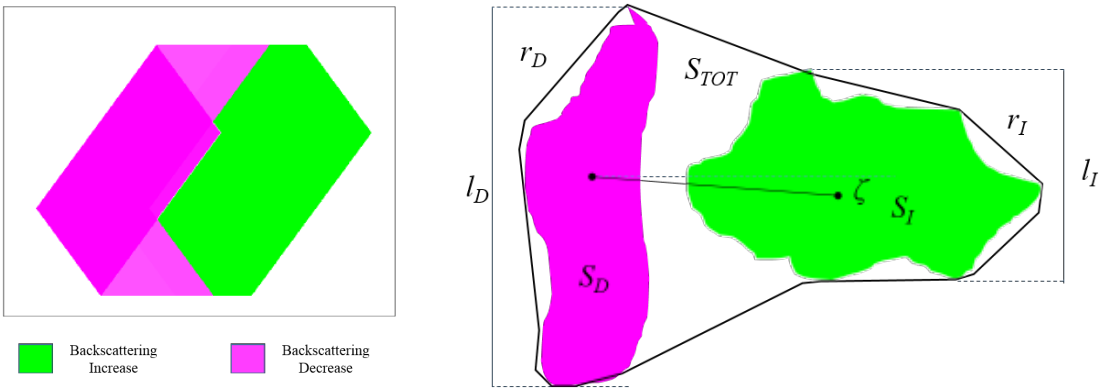

(a) (b)

Figure 6.6: Multi-temporal pattern for fully destroyed buildings, for (a) $\phi = 0$; (b) $\phi = \pi/4$. R,B: pre-event image; G: post-event image. Backscattering increase and decrease are represented in green and magenta, respectively. Representation of the geometrical features associated to the pair of regions R_I (in green) and R_D (in magenta) for the multi-temporal scattering pattern.

direction. Corresponding values S_I, l_I are defined for the increase region R_I. An area

measure S_{TOT} is then defined for the convex hull of the two regions. Based on these spatial parameters, four spatial features can be defined for the pair of regions R_I, R_D, in order to describe the multi-temporal pattern for the fully destroyed building (see Fig. 6.6b).

- area ratio r_a : minimum ratio between the areas S_I and S_D.

$$r_a = \min\{\frac{S_I}{S_D}, \frac{S_D}{S_I}\} \tag{6.12}$$

- azimuth length ratio r_l : minimum ratio between the lengths l_I and l_D.

$$r_l = \min\{\frac{l_I}{l_D}, \frac{l_D}{l_I}\} \tag{6.13}$$

- orientation ζ : clock-wise angle (taken in absolute value) between the range direction and the line connecting the centroids of the two regions.

- total change ratio r_t : ratio between the sum of the areas S_D, S_I and the convex hull area S_{TOT}.

$$r_t = \frac{S_D + S_I}{S_{TOT}} \tag{6.14}$$

From the literature, we expect that the ratio values tend to one (i.e., $r_a, r_l, r_f \simeq 1$), while orientation tend to zero ($\zeta \simeq 0$) [146].

6.3.2 Partially destroyed building

For a partially-destroyed building, the multi-temporal pattern presents a sequence of regions along the range direction more complex than that of fully destroyed building and depends on both the orientation angle ϕ and the damage parameters $\Delta H_H, \alpha$. A general characterization of the pattern is thus conducted with a sensitivity analysis, by considering $\theta > \pi/4$ and $L_R > H \cot\theta$. We assume that K_c, K_d are similar and much larger than K_a (i.e., $K_c \simeq K_d, K_a \ll K_d$). $\Delta H_H, \alpha$ are the free parameters ranging in $[\pi/12, \pi/3]$ and $[H/4, 3H/4]$, respectively. Very large values for parameters $\Delta H_H, \alpha$ are associated to geometries which are not likely to occur in real scenarios and thus excluded. The orientation angle varies in $[0, \pi/3]$. Higher values make the damaged facade tend to be oriented along the azimuth direction, thus the multi-temporal pattern tend to come close to profile D, with constant height on the slice.
Fig. 6.7 shows multi-temporal backscattering patterns of the partially damaged building, derived for two damage options and two different orientation angles. For the sake of simplicity in the analysis, both adjacent increase and decrease regions are grouped into

a single region. From near- to far-range, the multi-temporal pattern is composed by a sequence of regions $R_{dec1}, R_{nc1}, R_{dec3}, R_{nc2}, R_{inc}, R_{dec2}, R_{inc2}$ characterizing the damaged part; and a large no-change region, associated to the part of the building not affected by the damage. This no-change region is placed in far-range, with geometry dependent on the building orientation. Most of the change regions tend to be oriented according to ϕ (i.e., uniform along azimuth for $\phi = 0$). Conversely, R_{inc2} is elongated in the range direction, with size decreasing for ϕ tending to zero. Decrease regions $R_{dec1}, R_{dec3}, R_{dec2}$ are associated to the fall of the debris both reducing the near-range layover region and widening the far-range region associated to d. No-change regions R_{nc1}, R_{nc2} are associated to the part of the facade footprint showing no variations in the total scattering. Increase region R_{inc1} is associated to the scattering from the debris $c_d > c_w$. Increase region R_{inc2}, is due to the reduction of the shadow on building slices of the debris after the fall. For profile A, the slices have a far-range height $W \cot \beta < H$ smaller than that of the pre-event.

For large values of ΔH_H, the width along ground range for all the decrease and increase regions tends to be small, while that for the no-change regions tends to be large. Large ΔH_H corresponds to small ΔW for (6.4), so that the damage tend to be limited and the slice tends to behave as the standing building one. Large α corresponds to large ΔW for (6.4). This widen the region with scattering d and makes R_{inc1} large. On the other hand, large α makes slices following profile A with a small height, and thus a small shadow region. In the multi-temporal pattern, this makes R_{inc2} large along the range direction. Changes in the region sequence can be seen in presence of a strong triple-bounce contribution in the backscattering pattern of the partially-destroyed building, generating a local increase of backscattering. Nevertheless, the presence of this term is dependent on both α and ϕ, as described above. The multi-temporal patterns in the sensitivity analysis are used for deriving a multi-temporal backscattering prototype of the partially-destroyed building. In this work, patterns with similar characteristics have been considered by assuming the condition $\alpha < \pi/4$. A geometrical analysis of the regions has been conducted for this pattern, by focusing on two significant regions, namely the decrease region R_{dec2}, associated to the reduced size of the layover region, and the increase region R_{inc1}, associated to the layover with stronger scattering given by c_d. Change regions may be concave. Thus, the convex skull, defined as the largest convex polygon inscribed in the considered region [216], was selected for both R_{dec2}, R_{inc1}.

Let $\tilde{R}_I$, $\tilde{R}_D$ be the convex skull approximation for R_{inc1} and R_{dec2}, respectively. Similarly to what defined in Sec. 6.3.1, $\tilde{R}_I$ is characterized by area $\tilde{S}_I$, and length $\tilde{l}_I$, along the azimuth direction. Corresponding values $\tilde{S}_D$, $\tilde{l}_D$ are defined for the region $\tilde{R}_D$. Let $\tilde{S}_{TOT}$ be the area of the convex hull of the pair $\tilde{R}_I, \tilde{R}_D$. Based on these spatial parameters, four

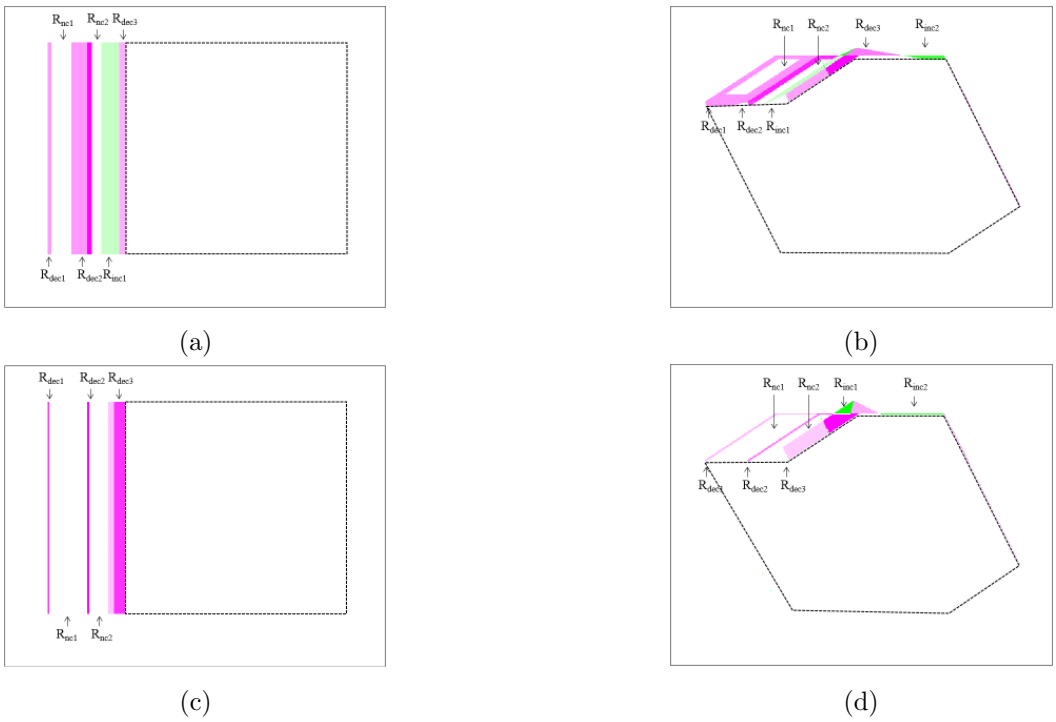

Figure 6.7: LR Patterns for partially destroyed buildings with different values set for parameters $\{\alpha, \Delta H_H, \phi\}$: (a) $\{\pi/12, H/4, 0\}$; (b) $\{\pi/12, H/4, \pi/3\}$; (c) $\{\pi/4, 3H/4, 0\}$; (d) $\{\pi/4, 3H/4, \pi/6\}$. Areas of backscattering decrease and increase are represented in magenta and green, respectively.

spatial features are defined for describing the multi-temporal pattern for the partially-destroyed building:

- area fill ratio $\tilde{r}_a$: ratio between the areas $\tilde{S}_I$ and $\tilde{S}_D$.

$$\tilde{r}_a = \frac{\tilde{S}_I}{\tilde{S}_D} \tag{6.15}$$

- azimuth lengh ratio $\tilde{r}_l$: minimum ratio between the lengths $\tilde{l}_I$ and $\tilde{l}_D$.

$$\tilde{r}_l = \min\{\frac{\tilde{l}_I}{\tilde{l}_D}, \frac{\tilde{l}_D}{\tilde{l}_I}\} \tag{6.16}$$

- orientation $\tilde{\zeta}$: clock-wise angle between the range direction and the line connecting the centroids of $\tilde{R}_I, \tilde{R}_D$.

- total change ratio $\tilde{r}_t$: ratio between the sum of the areas $\tilde{S}_I, \tilde{S}_D$ and the convex hull area $\tilde{S}_{TOT}$.

$$r_A = \frac{\tilde{S}_I + \tilde{S}_D}{\tilde{S}_{TOT}} \tag{6.17}$$

6.4 Proposed approach for unsupervised building Change Detection in VHR SAR images

In this section, an automatic hierarchical strategy for the unsupervised detection of building changes with different semantic meaning is proposed. Let X_1, X_2 be the two input VHR SAR images, with size $M \times N$, acquired before and after the change event, respectively. The strategy aims at deriving a multi-class CD map with 5 classes $\{\omega_0, \omega_1, \omega_2, \omega_3, \omega_4\}$. The classes are described as follows: 1) area with no change in backscattering (ω_0); 2) new building (ω_1); 3) fully destroyed building (ω_2); 4) partially-destroyed building (ω_3); 5) change in backscattering not associated to buildings (ω_4). The novelty of the proposed strategy lies in both integrating the proposed scattering model for partially-destroyed buildings in an automatic building CD strategy and considering a change hierarchy associated to the different spatial scale (see Fig. 6.8) to formulate the CD problem. Classes are reported as $\{\omega_1, \omega_2\}$ for for the first hierarchical level and $\{\omega_0, \omega_3, \omega_4\}$ for the second one. Fig. 6.9 illustrates the general block scheme of the proposed approach. The scheme namely presents: a processing stage for the multi-temporal comparison and the generation of a backscattering CD Map; Fully-destroyed building detection (FDBD) on the first hierarchical level, for identifying classes ω_1, ω_2; a changed-building mask generation for removing ω_1, ω_2 from the analysis at second level; Partially-destroyed building detection (PDBD) on the first hierarchical level, for identifying classes $\omega_0, \omega_3, \omega_4$; fusion of the

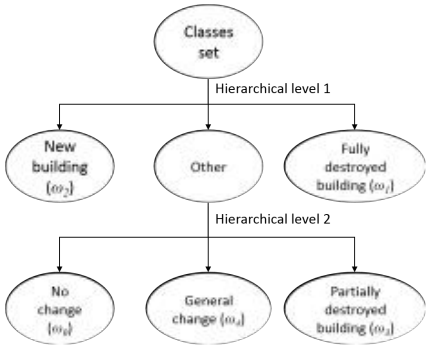

Figure 6.8: Hierarchical representation of the Building CD problem.

building CD maps. Each Building detection step includes a step for the selection of the best building candidates and another step for the analysis of their geometrical features based on a fuzzy-logic set. The parameters used in the fuzzy set are tuned based on the model of the building and its robustness to noise and clutter. On both levels, the building CD performs building candidate selection and a spatial analysis of the candidates.

6.4.1 Multi-temporal comparison and Backscattering CD

Multi-temporal comparison of X_1, X_2 is conducted by means of the log-ratio operator. The log-ratio image X_{LR} is defined as follows:

$$X_{LR} = \log \frac{X_2}{X_1} \tag{6.18}$$

Log-ratio operator is frequently used as a pixel-based index in SAR CD analysis, as it both mitigates the speckle effect on the multi-temporal information and highlights both

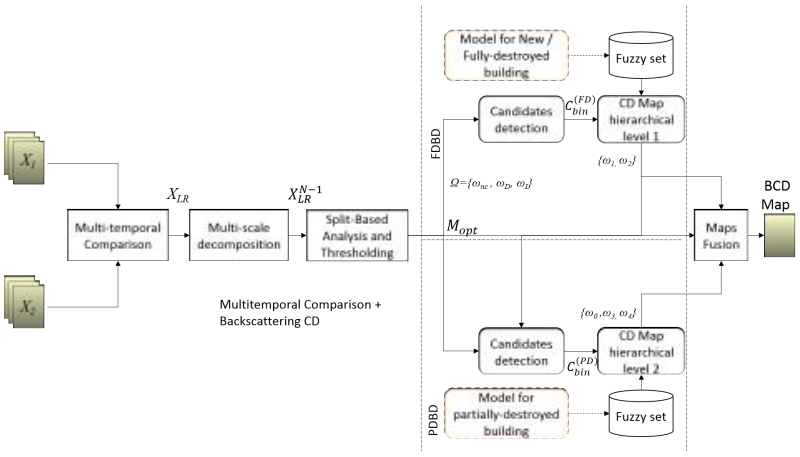

Figure 6.9: Block scheme of the proposed approach.

the increase and decrease of backscattering, which assume positive and negative values in X_{LR}, respectively [146; 234; 184; 127; 23]. Despite the large mitigation of the speckle effect, a residual noise contribution may still impact on the CD analysis. A multi-scale decomposition step is applied to X_{LR} in order to overcome these issues [32; 146; 5; 3]. The output of the decomposition process is a set of images $X_{LR}^n, n = 0, ..., N-1$. Images with large n, have high robustness to noise but small level of detail and vice versa. In the wavelet decomposition, X_{LR} is assumed as X_{LR}^0 (i.e., $X_{LR}^0 = X_{LR}$). For this, 2D Discrete Stationary Wavelet Transform (2D-SWT) is selected as as multi-scale operator, following [5; 146]. At scale level $N-1$, changes on small elements are neglected, while the large ones are detected as homogeneous change areas. The optimal value N is chosen based on the minimum building footprint size, in order to preserve the edge information while mitigating the residual speckle effect.
Let X_{LR}^{opt} be the decomposition at the optimal scale level (i.e., $X_{LR}^{opt} = X_{LR}^{N-1}$). An unsupervised thresholding is performed on the X_{LR}^{opt}, in order to derive a backscattering CD map with classes $\omega_I, \omega_D, \omega_{nc}$. The thresholding considers a split-based analysis [33] in order to have populations for ω_I, ω_D comparable to that for ω_{nc}. The analysis divides the image X_{LR}^{opt} into splits with size $S_R \times S_A$ and considers pixel variance as a change content measure. A subset of splits with largest variance is defined for the threshold selection, based on a split selection parameter B. S_A, S_R are chosen based on the average building size on the scene, while B is tuned based on the application. Small B values correspond to a larger proportion of the total change information and vice versa.
A Bayesian thresholding is applied on the set of selected splits, by assuming that samples of the set be modeled as a mixture of three Gaussian distributions. Unknown prior probabilities and marginal distribution parameters are estimated with EM algorithm [23]. The estimated thresholds are then extended to the whole image and backscattering CD map M_{opt} is obtained.

6.4.2 Hierarchical level 1: Fully-destroyed building detection (FDBD)

Starting from M_{opt}, building change detection is performed on each hierarchical level by detecting the changed building candidates and then performing spatial analysis on each of them in order to detect classes. Changed building candidates are generally associated to areas with large density of changed pixels. The candidate detection is performed via a set of moving windows applied on the scattering CD map, following the approach in [146]. In order to capture most of the possible orientations for the changed building candidates, five possible windows $W_\beta, \beta = 1, ..., 5$ with constant area and different geometry are considered in the analysis. The spatial analysis of the candidates is conducted by evaluating the geometry of the change regions (as defined in both Sec. 6.3.1 and Sec. 6.3.2) with a

fuzzy inference system, in order to detect building classes.
For the first level, the changed building candidates are detected by using a sliding window with size parameters z_1, z_2 on M_{opt}. Scanning from left to right, the total number of changed pixels inside the window is computed. Fig. 6.10 shows the set of the possible moving windows applied in the candidates detection. In particular, W_β includes four rectangular windows with size $z_1 \times z_2$ and different orientation angles (i.e., $\{\pi/2, \pi/4, 0, -\pi/4\}$) and a square window of size $\sqrt{z_1 z_2} \times \sqrt{z_1 z_2}$. As the detection at the first hierarchical level is devoted to completely changed building candidates, the values of z_1, z_2 are selected based on the average building footprint size on the site. Let $W_\beta(i,j), \beta = 1, ..., 5$ be one

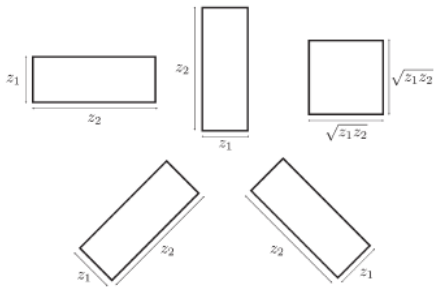

Figure 6.10: Set of moving windows used for the candidate detection with dimensions z_1, z_2.

of the possible moving windows centered on the pixel (i,j), with size parameters $z_1 \times z_2$. Let $M^{(FD)}_{W_\beta(i,j)} = M_{opt} | M_{opt} \subset W_\beta(i,j)$ be the set of pixels of M_{opt} in $W_\beta(i,j)$, indicating the amount of pixels belonging to ω_D or ω_I. A candidate index $C^{(FD)}(i,j)$ for the pixel (i,j) can be defined as the maximum value of the set, indicating the amount of the change information detected in the set of windows.

$$C^{(FD)}(i,j) = \max_{\beta=1,...,5} card(M^{(FD)}_{W_\beta(i,j)} \in \omega_D \wedge M^{(1)}_{W_\beta(i,j)} \in \omega_I) \tag{6.19}$$

where $card(\cdot)$ represents the cardinality of the set. Finally, a binary map of the candidates $C^{(1)}_{bin}$ is derived by thresholding $C^{(FD)}$ with threshold value $T^{(FD)}_C$. The set of candidates is extracted from $C^{(FD)}_{bin}$ by considering the connected components of the changed regions and by applying the flood-fill algorithm with an eight-connected neighborhood [18; 146]. The threshold is chosen based on the size of the moving window (i.e., $T^{(FD)}_C = t z_1 z_2, 0 < t \leq 1$). A bounding box is traced for each of the candidates and all possible region pairs with an increase and a decrease region are considered for a spatial analysis. Without loss of generalization, let us assume that one region of decrease and one region of increase exist inside the single candidate box. If more regions of increase or decrease exist, spatial analysis is conducted on each possible pair and the one providing the best candidate score is assumed as most reliable. The spatial analysis of the region pair is conducted with a fuzzy inference

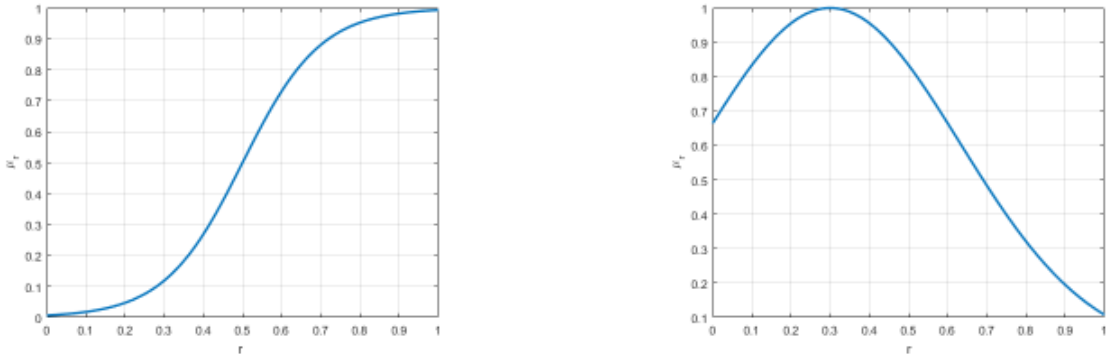

(a) (b)

Figure 6.11: Examples of membership function: a) Sigmoid function with $s = 10, t = 0.5$; and b) Gaussian function with $\mu = 0.35, \sigma^2 = 0.332$.

system based on the geometrical parameters of the pair [186]. The analysis focus on the set r_l, r_a, r_f, ζ. As described in Sec. 6.3.1, reliable values of r_a, r_f, r_l are expected to be close to 1, as there is no sensible prevalence of the values of either R_I or R_D. On the other hand, reliable values of ζ are expected to be close to zero [146]. Thus for the evaluation, Sigmoid membership functions $\Sigma_l(r_l, a_l, c_l), \Sigma_a(r_a, a_a, c_a), \Sigma_f(r_f, a_f, c_f)$ and $\Sigma_\zeta(|\zeta|, a_\zeta, c_\zeta)$ are chosen for the features r_l, r_a, r_f and ζ, respectively. Sigmoid membership function $\Sigma(r, s, t)$ (Fig.6.11a) is described by parameters s and t associated to the slope and the center of the function, respectively, as follows:

$$\Sigma(r, s, t) = \frac{1}{1 + e^{-s(r-t)}} \tag{6.20}$$

Parameters are set as $s_a, t_a, s_f, t_f, s_l, t_l > 0$ for the ratio-based membership functions, while $a_\zeta < 0, c_\zeta > 0$ for the orientation. For each pair of candidate regions, the aggregate membership $\eta_{FD} = \Sigma_l \Sigma_a \Sigma_\zeta \Sigma_f$ is computed for global evaluation. The candidates with Σ greater than a membership threshold $T_\eta^{(FD)}$ are labeled either ω_1, ω_2, depending on whether R_D appears in near range and R_I in far range or vice versa [146]. The objects detected as ω_1, ω_2 are masked out from the map M_{opt}, resulting in a map $M_{opt}^{(mask)}$.

6.4.3 Hierarchical level 2: Partially-destroyed building detection (PDBD)

The analysis of the PDBD is structured with the same paradigm of the FDBD, because of the geometrical properties of the multi-temporal model for the partially destroyed building (Sec. 6.3.2), but it takes into account important modifications due to the different size and spatial properties of the change regions. For the second hierarchical level, the changed building candidates are detected from $M_{opt}^{(mask)}$ by using a sliding window with size

parameters z_1, z_2, scanning from left to right and counting the total number of changed pixels inside the window. The windows keep the same set of orientation values as in Fig. 6.10. The detection provides a candidate index $C^{(PD)}$ indicating the amount of the change information in the set of windows. A binary map of the candidates $C_{bin}^{(PD)}$ is derived by thresholding $C^{(PD)}$ with threshold value $T_C^{(PD)}$, chosen based on the size of the moving window (i.e., $T_C^{(PD)} = tz_1z_2, 0 < t \leq 1$). The set of candidates is extracted from $C_{bin}^{(PD)}$ by considering the connected components, similarly to what done in FDBD.
In order to avoid the detection of a large number of small candidates, window size parameters are kept similar to those considered in the first hierarchical level, while threshold value is selected smaller. A bounding box is traced for each candidate and a spatial analysis is conducted on region pairs $\tilde{R}_I$, $\tilde{R}_D$. For the case of partially destroyed building, the spatial analysis focuses the set $\tilde{r}_l, \tilde{r}_a, \tilde{r}_f, \tilde{\zeta}$. For the evaluation, Sigmoid membership function $\Sigma_l(\tilde{r}_l, b_l, d_l)$, defined in (6.20), and Gaussian membership functions $\gamma_a(\tilde{r}_a, \mu_a, \sigma_a), \gamma_f(\tilde{r}_f, \mu_f, \sigma_f), \gamma_\zeta(\tilde{\zeta}, \mu_\zeta, \sigma_\zeta)$ are chosen for the features $\tilde{r}_l$, $\tilde{r}_a$, $\tilde{r}_f$ and $\tilde{\zeta}$, respectively. Gaussian membership function $\gamma(r, \mu, \sigma)$ (Fig.6.11b) is described by parameters μ and σ associated to mean and standard deviation of the function, respectively, as follows.

$$\gamma(r, \mu, \sigma) = e^{\frac{-(r-\mu)^2}{2\sigma^2}} \tag{6.21}$$

All the parameters of the four membership functions are set with real positive values. For each pair, the aggregate membership $\eta_{(PD)} = \gamma_a\gamma_\zeta\gamma_f\Sigma_l$ is computed. The candidates both presenting a pair of regions with decrease and increase in near and far range, respectively, and having a value γ greater than a membership threshold T_η^{PD} are classified as partially destroyed buildings (ω_3).

6.4.4 CD Map Fusion

An overall building CD map is obtained by combining information from M_{opt} and the output maps from both FDBD and PDBD. Regions of no-change in backscattering are labeled as ω_0. Regions of ω_I, ω_D not associated to any of the building models (i.e., $\omega_1, \omega_2, \omega_3$ classes) are labeled as general change (ω_4). Remaining regions of no backscattering variations are labeled as no-change (ω_0). The overall building CD map represents $\omega \in \{\omega_0, \omega_1, \omega_2, \omega_3, \omega_4\}$.

6.5 Experimental Results

In order to validate the proposed approach, two datasets of multi-temporal VHR SAR images with size 1024×1024 pixels have been considered. The two datasets describe two residential areas in the city of L'Aquila (Italy), that has been interested by a strong

earthquake, which caused the collapse of several buildings and relevant damages to many others, together with the death of several civilians. The first dataset is a residential modern area outside the inner city, for which most of the buildings can reasonably assumed as isolated from the neighbors. The second dataset is near a medieval residential area in the inner city, in which part of the scene presents buildings that are very close each other. This aspect makes the building change detection more complex. For both the multi-temporal datasets, pre-event and post-event VHR SAR images have been acquired by the Cosmo-SkyMed constellation in Spotlight mode on April 5th, 2009 and September 12th, 2009 respectively. Both images are in HH polarization, have incidence angle $\theta = 53°$ and a spatial resolution of 1 meter. Radiometric calibration, geo-referencing and co-registration were performed.

For the validation, a reference map of the fully and partially destroyed buildings in the area has been derived based on a post-event damage survey conducted on site. The survey provided a building damage map with EMS98 scale [202]. Because of the damage grade and the spatial resolution of the data, the attention was focused on grades 4 (partially destroyed) and 5 (fully destroyed) of the EMS scale. The analysis has been refined to the best of our abilities by a visual inspection of an ortho-photo of the crop acquired after the seismic event and by taking into account the SAR geometry of acquisition. For buildings with lacking information of the EMS damage, the visual inspection has been the only factor for the generation of the reference. For the validation of the proposed approach, detection accuracy has been evaluated at building level, evaluating the correct detections and mis-classifications for the classes ω_1, ω_2 and ω_3. In the following, a more detailed description of the scene and the performance of the proposed approach are reported for the two crops.

6.5.1 Crop 1: Modern Residential Area

The first crop has a size of 1024×1024 pixels and represents the southern part of inner city. Fig.6.12a shows a multi-temporal false color composition of the two SAR images of Crop 1, where areas of backscattering increase and decrease appear in magenta and green, respectively. Fig.6.12b shows the post-event ortho-photo, with red an yellow polygons indicating fully and the partially destroyed buildings, respectively. A total of 200 buildings were counted. Among these, 8 buildings were classified as fully destroyed (ω_1), 6 as partially destroyed (ω_3) and 0 as new (ω_2).

The proposed approach computed the log-ratio feature X_{LR} and performed multi-scale analysis has been conducted on X_{LR}, generating the sequence $\{X_{LR}^0, ..., X_{LR}^{N-1}\}$. The optimal scale level N has been selected considering the average building size and the noise level of the SAR images. It has been demonstrated that the value $N = 4$ preserves radar

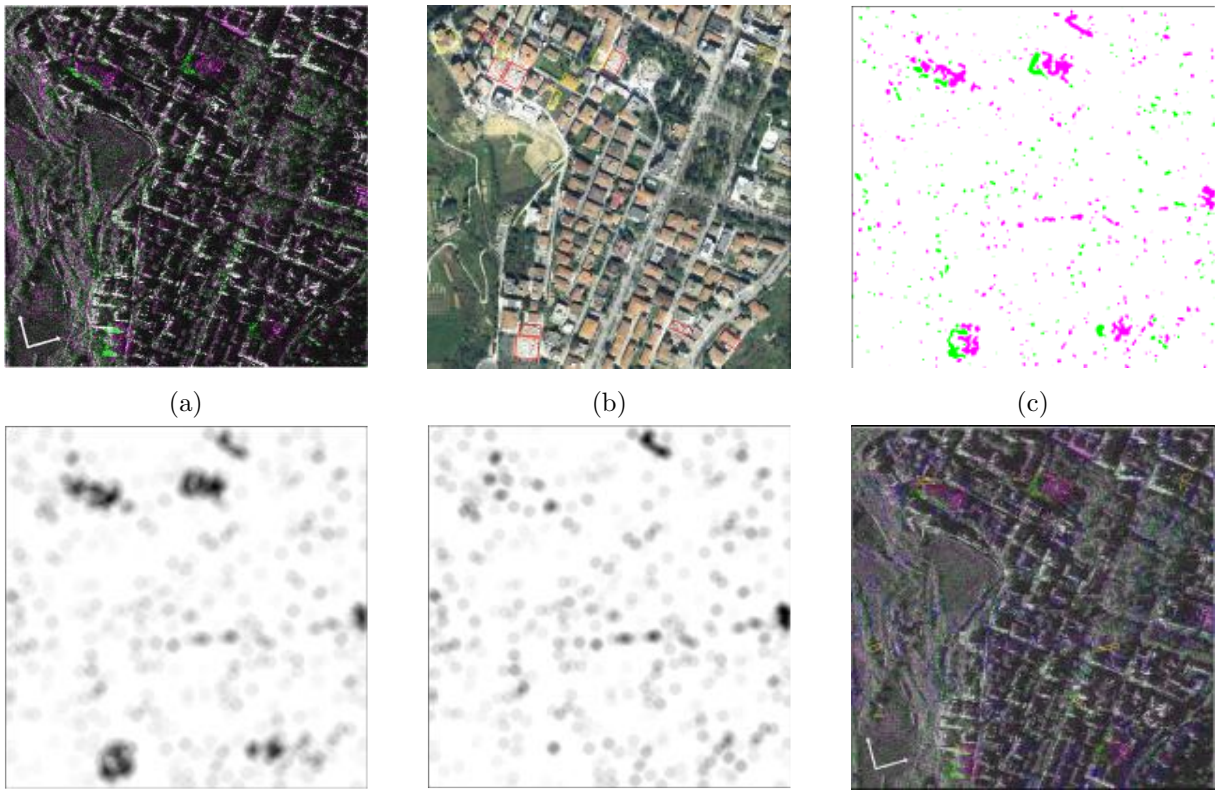

Figure 6.12: Crop 1: a) Multi-temporal false color composition of SAR images (R,B: September 2009, G: April 2009); b) Optical post-event image; c) Backscattering CD Map M_{opt}, with increase and decrease represented in magenta and green, respectively; d) Candidate gray-scale map $C^{(1)}$; e) Candidate gray-scale map $C^{(2)}$; f) Multi-class building CD map overlapped with multi-temporal false color composition of the SAR images (ω_1 (red), ω_3 (yellow), ω_4 (blue)).

footprint of buildings with size larger than 8 meters, which is reasonable for the proposed scenario [146]. The impulse response of the filters in the 2D-SWT have been chosen from the Daubechies family with order 4. The split-based analysis has been conducted on X_{LR}^{N-1} for deriving the backscattering CD map M_{opt}. The split size has been selected by taking into account the average size of the building radar footprint along the range and azimuth directions. This resulted in $S_R = 120$ and $S_A = 40$ pixels, respectively. The selection of the splits with highest change content has been conducted by selecting $B = 3$. Previous works demonstrated how the split-based approach has robust performance with respect to the split size in range of values $[20; 60]$ and $[80; 170]$ for S_A and S_R, respectively [146]. On the samples of the split subset, no-change and change classes have been separated by estimating the statistical unknown parameters with the EM algorithm and applying the Bayesian thresholding. Fig.6.12c shows the map M_{opt}, in which backscattering increase and decrease are represented in green and magenta, respectively.
FDBD has been conducted on the map, starting with the analysis based on the sliding window for the extraction of the building candidates. FDBD detects the presence of fully destroyed buildings, thus the window size has been selected comparable to the minimum building footprint, with values $z_1 = 40, z_2 = 20$ respectively [146]. Fig.6.12d shows the output map generated by the sliding window. Threshold scale value $t = 0.2$ was selected in order to limit the outliers in the candidate analysis. This resulted in a total of 52 building candidates. For each of the building candidates, the proposed fuzzy rules have been applied. Aggregate membership η_{FD} has been derived and thresholded for detecting new and fully destroyed buildings. The threshold was selected by considering a limit case of 0.6 for the membership function of the single rules, resulting in a aggregate value $T_\eta^{(FD)} = 0.125$ for η_{FD}. The value is compatible with the considerations asserted in [146]. After the masking of the detected buildings on M_{opt}, PDBD has been conducted on the masked map. In order to avoid a large number of small regions, the window size has been selected with same size of that in FDBD. The threshold for the candidates detection in this step has been selected smaller than that required for the FDBD (i.e., $t = 0.0725$). The analysis yielded a set of 139 candidates. The proposed fuzzy rules have been applied on the candidates. Aggregate membership η_{PD} has been derived and thresholded. An overview of the parameters considered in the analysis is reported in Table 6.4. The maps obtained with the application of the two fuzzy sets have been fused in the final multi-class building CD map (see Fig.6.12f).

Table 6.5 reports the quantitative assessment for crop 1. With the proposed approach, 7 out of 8 buildings were correctly labeled as ω_1 (see Fig. 6.13a), while 4 out of 6 as ω_2. Both the miss detections correspond to two buildings of classes ω_1 and ω_3 that are both

Table 6.4: Parameters used in the experiments: (a) common parameters; (b) FDBD and PDBD specific parameters.

Parameter	**Value**
N	4
S_R	120
S_A	40
B	3
z_1	40
z_2	20

(a)

FDBD		**PDBD**	
Parameter	**Value**	**Parameter**	**Value**
t	0.2	t	0.0725
T_η^{FD}	0.125	T_η^{PD}	0.125
a_a	10	μ_a	3.6
c_a	0.3	σ_a	1.55
a_l	10	b_l	10
c_l	0.5	d_l	0.15
a_ζ	-10	μ_ζ	$\pi/8$
c_ζ	$\pi/3$	σ_ζ	0.4
a_f	30	μ_f	0.45
c_f	0.5	σ_f	0.12

(b)

labeled as ω_4. The three miss detections correspond to a fully and partially destroyed building labeled as general change and a partially destroyed building labeled as no change, respectively. A total of 5 false alarms was reported for building misclassified as ω_3. It is worth noting that the five false alarms are buildings not following the model of partially destroyed building, but still characterized dy a damage level EMS4 in the survey [202]. From a qualitative analysis, the miss detection of the fully collapsed building (ω_1) may be probably explained by the influence of the surrounding buildings and vegetation the multi-temporal building footprint (see 6.13b and 6.13c). Most of the false alarms can be associ-

Table 6.5: Crop 1: Detection assessment of the proposed approach for L'Aquila dataset.

Building Detection Assessment		
Correct Detections		
Fully Destroyed (ω_1)	7	
Partially Destroyed (ω_3)	4	
Missed Detections		
Fully Destroyed	detected as Partially Destroyed (ω_3)	0
	detected as general change (ω_4)	1
	detected as no change (ω_0)	0
Partially Destroyed	detected as Fully Destroyed (ω_1)	0
	detected as general change (ω_4)	1
	detected as no change (ω_0)	1

ated to the presence of vegetated areas close to the buildings, creating a multi-temporal behavior for the scattering not clearly predictable nor considered in the backscattering model (see Fig.6.13d) [217].

6.5.2 Crop 2: Medieval Residential Area

Fig.6.14a shows the multi-temporal false color composition of the two SAR images for Crop 2, with green and magenta mapping the backscattering increase and decrease, respectively. Fig. 6.14b shows the corresponding post-event ortho-photo. From the ortho-photo, 165 buildings were counted. Among these, 3 were classified as fully destroyed, 4 as partially destroyed and 0 as new. The approach considered the generation of the log-ratio X_{LR} and the use of the wavelet-based multi-scale analysis for generating the robust multi-temporal feature X_{LR}^N. $N = 3$ was selected as optimal scale value. Split-based CD analysis was conducted on X_{LR}^N for generating the backscattering CD map (see 6.14c). For the FDBD, a sliding window with size $z_1 = 40, z_2 = 20$ was selected for the candidate detection (see Fig 6.14d). Fig 6.14d shows the output map generated by the sliding window in the FDBD. The thresholded map provided as set of 85 possible candidates. The set of fuzzy rules was applied on the building candidates and the aggregate membership was thresholded. An overview of the parameters selected in the fuzzy analysis is presented in Table 6.4. With the masking of the elements in ω_1, ω_2, the PDBD analysis was conducted. Same parameters were kept for the sliding window. A threshold scale value $t = 0.1$ was selected slightly higher in order to have a robust detection in presence

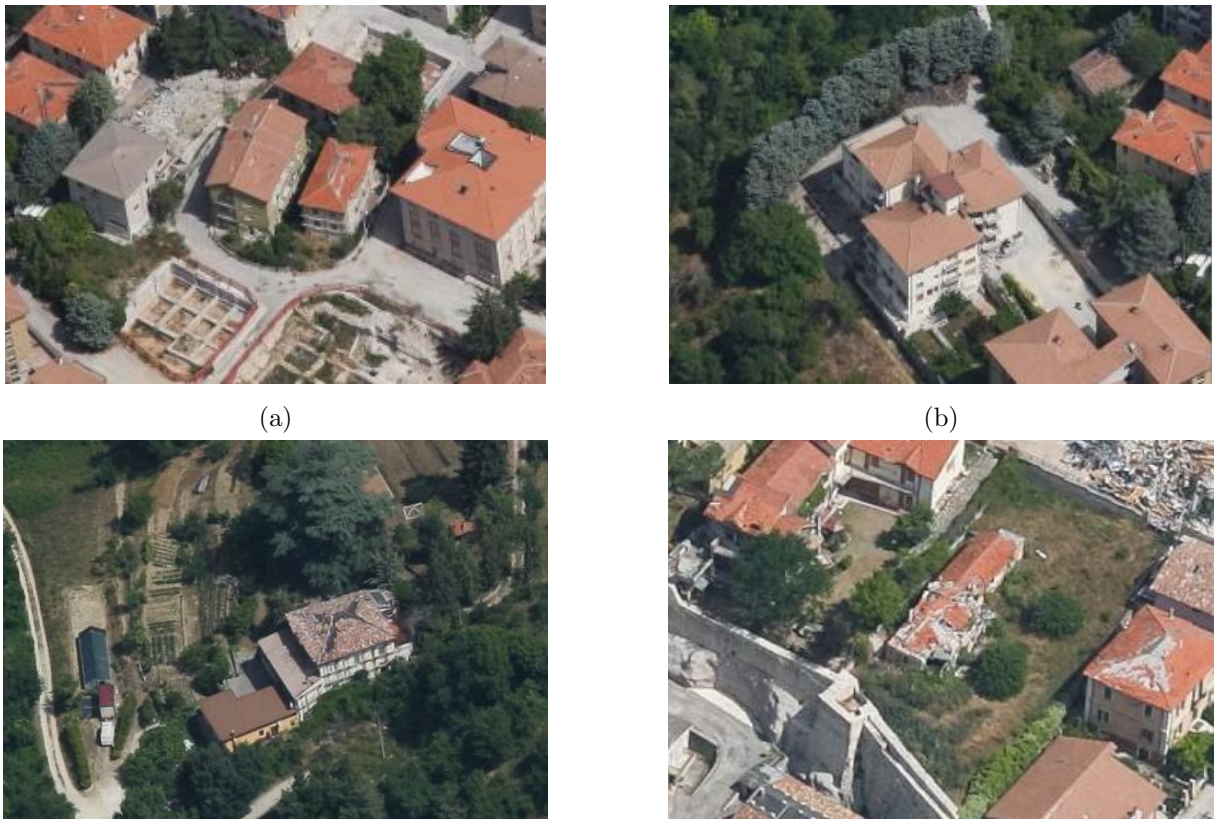

(a) (b)

(c) (d)

Figure 6.13: Crop 1: Examples for buildings detected by the proposed approach: a) miss (above) and correct (below) detection for Fully Destroyed building class; b) correct detection for Partially Destroyed Building class; c) false alarm for Partially Destroyed Building class; d) miss detection for Partially Destroyed Building class.

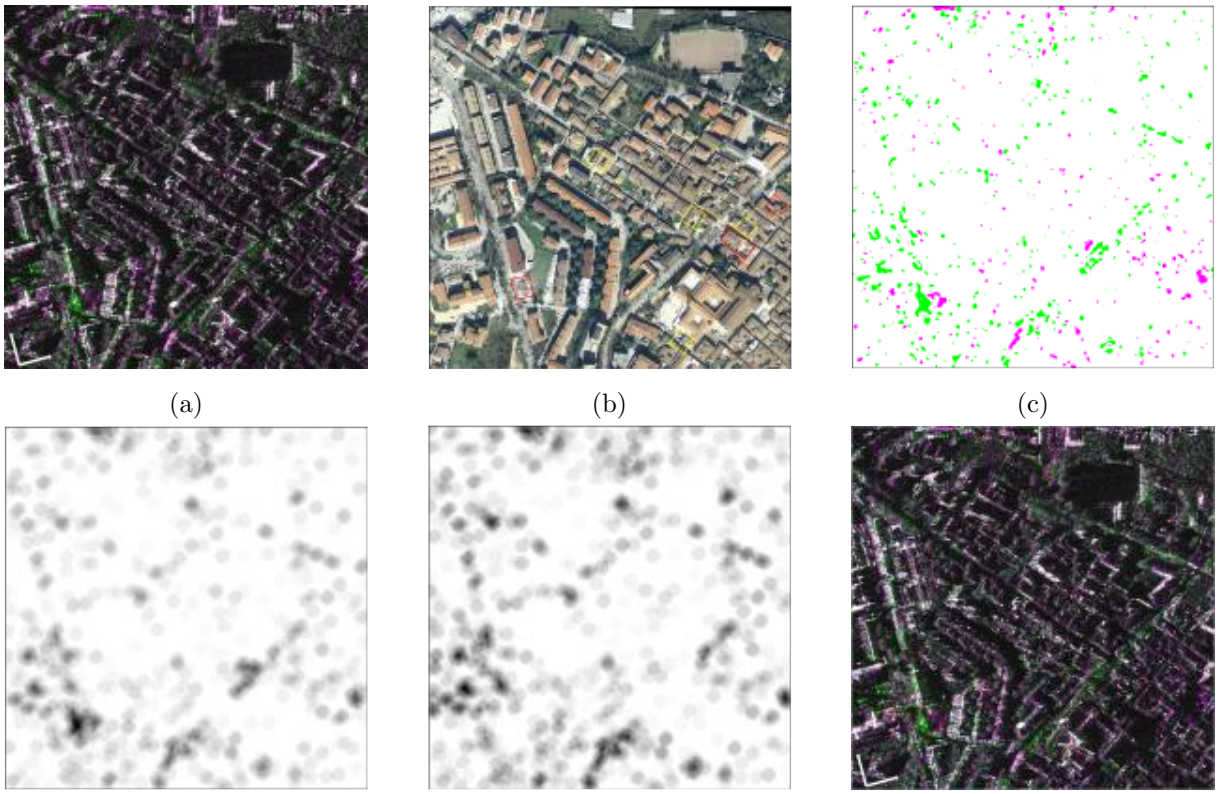

Figure 6.14: Crop 2: a) Multi-temporal false color composition of SAR images (R,B: September 2009, G: April 2009); b) Optical post-event image; c) Backscattering CD Map M_{opt}, with increase and decrease represented in magenta and green, respectively; d) Candidate gray-scale map $C^{(1)}$; e) Candidate gray-scale map $C^{(2)}$; f) Multi-class building CD map overlapped with multi-temporal false color composition of the SAR images (ω_1 (red), ω_2 (green), ω_3 (yellow), ω_4 (blue)).

of local vegetated areas (see 6.14b). This provided a set of 141 candidates. The resulting building candidates have been analyzed with the proposed fuzzy logic set. Thresholding on the aggregate membership values have has been finally conducted. The final CD map is reported in Fig. 6.14f.

Table 6.6: Crop 2: Detection assessment of the proposed approach for L'Aquila dataset.

Building Detection Assessment		
Correct Detections		
Fully Destroyed	2	
Partially Destroyed	2	
Missed Detections		
Fully Destroyed	detected as Partially Destroyed	1
	detected as general change	0
	detected as no change	0
Partially Destroyed	detected as Fully Destroyed	0
	detected as general change	2
	detected as no change	0

Table 6.6 reports the performance analysis for Crop 2. The proposed approach presents the correct detection of 1 fully destroyed building (ω_1) and 2 partially destroyed buildings (ω_3), with the 4 miss detection, namely 2 fully destroyed and 2 partially destroyed buildings. However, it is worth noting that one of the miss detection associated to ω_1 has been detected as ω_3, while both the miss detections in ω_3 are labeled as ω_4. This may result important in an emergency scenario where it is important to trigger a building change event. The proposed approach introduced 6 false alarms in the two hierarchical levels, namely, 1 associated to ω_1, and 2 to ω_2 and 3 for ω_3, respectively. Their presence can be explained by the large building density and the strong presence of vegetation in the local scene, which introduce modifications in the expected building scattering model.

6.6 Conclusion

In this chapter, a novel approach for the building change detection in multi-temporal VHR SAR has been presented. The approach aims at defining a hierarchical detection of the changes, based on the spatial scale level. In particular, two level of analysis are considered, associated to either new, fully destroyed buildings or partially destroyed buildings.

A multi-temporal scattering model for partially damaged building has been illustrated in this work for supporting the detection capabilities of the proposed strategy. The model makes some assumptions about the geometry and the size of the building and its damaged part. It derives the multi-temporal scattering behavior by comparing the two single-time scattering patterns, each obtained by applying the ray-tracing method to the corresponding model. The multi-temporal behavior has been used for defining a novel set of fuzzy-based geometrical rules for the class of partially-damaged building.
A validation of the proposed approach has been conducted by considering a pair of VHR SAR images acquired by Cosmo-SkyMed constellation before and after the earthquake in L'Aquila, 2009. The results highlighted the effectiveness of the detection, with the detection of damages not associated to fully destroyed buildings, but with a large relevance in practical applications as damage assessment and emergency response.
Future developments aim at considering further geometries for the partially destroyed building in the automatic detection strategy. Furthermore, they will study the detection problem in presence of dense built-up areas, where building footprint is partially affected by surrounding elements.

Chapter 7

Discussion and future developments

This chapter draws the conclusions for the unsupervised methods for CD in Polarimetric SAR and VHR SAR imagery that have been presented the thesis and illustrates the future developments.

7.1 Conclusions

In this thesis, we described the properties of SAR imagery and the scattering information in terms of more polarimetric channels (PolSAR) or a very high resolution (VHR SAR). Based on that, we proposed novel strategies for unsupervised CD that discriminate several change classes (as in the case of PolSAR) or improve the detection of changed buildings in urban areas (as in the case of VHR SAR). Concerning PolSAR data, methods have been designed based on the polarimetric scattering properties: i) an unsupervised multi-class change detection approach based on bi-temporal dual-pol SAR data; ii) an unsupervised approach for change detection of built-up areas for bi-temporal full-pol SAR imagery; iii) an approach for change detection and robust classification based on a full-pol SAR image time-series. Concerning VHR SAR data, we focused on the separation of different building change classes, performed according to the geometrical properties of the building multi-temporal scattering. The unsupervised approach detects both fully and partially destroyed buildings.

In Chapter 3, an unsupervised approach for multi-class CD of bi-temporal dual-pol SAR images has been presented. The approach generates a multi-dimensional polarimetric change vector as the comparison of the dual-pol images. The polarimetric scattering theory allowed to model the behavior of no-change and multiple changes classes in the PCV polar domain. The proposed representation drives the design of a CD strategy that automatically estimates the number of classes and separates the no-change and the multiple change classes. The framework proved to effective in several change detection

problems with both different number and kinds of change, on images acquired by different polarimetric sensors. The method accuracy is comparable with the state of the art but results provide more information on the change class, compared to standard methods in the literature that tackle binary CD.

In Chapter 4 an unsupervised CD strategy for bi-temporal full-pol SAR data focusing on built-up elements has been presented. The approach is based on the extraction of two polarimetric features, namely the overall scattering power and average scattering mechanism, represented in terms of angle. The single-time features are combined into a multi-temporal change index describing the changes in built-up areas. Positive and negative values are associated to constructed and demolished buildings, respectively. The approach has been validated on two multi-temporal full-pol datasets of urban scenarios with different complexity, in terms of both the extension and number of changed classes. The proposed approach has shown good detection performance.

In Chapter 5 an approach for multi-temporal image analysis based on a full-polarimetric SAR image time series and the use of a framework of wavelet transforms in the time domain has been proposed. The framework aims both at separating different natural classes with multi-temporal data and detecting changes in the time series. The analysis is based on the use of polarimetric features from two incoherent decompositions, based on power scattering mechanisms and eigenvalues-eigenvectors, respectively; and the use of the wavelet transform in the time domain. In the wavelet analysis, different approaches considering either decimation step or not have been considered for the analysis. Together with their direct application to the image, the wavelet transforms have been used for multi-scale and spline-based strategies. Experimental results focused on a selected set of regions for quantitative assessment of performance indicators for class separation and analysis of changes evolution, based on the wavelet approximation and detail components, respectively. For all the indicators, helix and volume power scattering have proved to be effective features.

In Chapter 6, an unsupervised approach for the detection of fully- and partially-destroyed buildings based on bi-temporal VHR SAR data has been presented. The multi-temporal scattering model for both fully- and partially-destroyed buildings is defined and integrated into an automatic detection strategy by means of a fuzzy logic set. Two hierarchical steps are designed: one for the detection of fully-destroyed buildings, and one for partially-destroyed ones, which accounts for the different size of the scattering changes. The approach has been validated on two multi-temporal datasets and proved its effectiveness in detecting the different building classes. Misclassifications were caused in presence of strong vegetated areas and dense urban areas, where the proposed scattering model is less funded.

The contributions of the different chapters incremented the state of the art for the multi-temporal analysis of VHR SAR and PolSAR data and opened to possible applications based on the separation of multiple change classes.

7.2 Future developments

The proposed strategies for CD in PolSAR images provided good accuracy performance. However, improvements can be achieved by: integrating pixel context information in the unsupervised strategies to mitigate the presence of misclassifications; a rigorous study of the statistical model to fit the multi-temporal features proposed in the two approaches and of definition of thresholding strategies for polarimetric data. Furthermore, the increasing amount of full-polarimetric SAR data allows for the extension of the proposed multi-class model to the use of full-polarimetric information, represented in terms of complex covariance elements or real decomposition features. It also introduces the possibility of multi-scale analysis and different wavelet filters with on temporal wavelet based on large temporal series of full-pol SAR images, showing different aspects of the multi-temporal information. The integration of spatial and temporal wavelet analysis for robust analysis of polarimetric image time series represent is also one of the future developments.
Concerning the CD strategy for VHR SAR images, improvements can be achieved by: the integration of polarimetric VHR SAR data, acquired by airborne and forthcoming spaceborne SAR systems, in the multi-temporal analysis (i.e., in presence of external elements perturbing the expected building footprint); the integration of multi-angle and multi-modality SAR data for very dense urban areas; the definition of a scattering model for partially destroyed buildings with different geometries.

List of Publications

7.2.1 Book Chapters

- M. Dalla Mura, J.A. Benediktsson, J. Chanussot, L. Bruzzone, "Advances in Change Detection Techniques for Multitemporal SAR Images" , in Mathematical Models for Remote Sensing Image Processing, Ed. B. Aiazzi, F. Bovolo, L. Bruzzone, A. Garzelli, D. Pirrone, C. Zoppetti, Springer Verlag, ISBN-13.

7.2.2 International Conferences

- Pirrone, D., Bovolo, F. and Bruzzone, L., "Analysis of backscattering behaviors for partially damaged buildings in VHR SAR images." In Proceedings of SPIE Remote Sensing (Tolouse, France, September 21 - 24, 2015).

- Pirrone, D., Bovolo, F. and Bruzzone, L., "A novel framework for change detection in bi-temporal polarimetric SAR images." In Proceedings of SPIE Remote Sensing (Edinburgh, France, September 26 - 29, 2016).

- De, S., Pirrone, D., Bovolo, F., Bruzzone, L., Bhatthacharya, A., "A novel change detection framework based on deep learning for the analysis of multi-temporal polarimetric SAR images" In Proceedings of IEEE Geoscience And Remote Sensing Symposium (IGARSS) (Forth Worth, United States, July 23-28, 2017).

- Pirrone, D., De, S., Bhattacharya, A., Bruzzone, L., Bovolo, F., "Unsupervised change detection in built-up areas by multi-temporal polarimetric SAR images" In Proceedings of IEEE Geoscience And Remote Sensing Symposium (IGARSS) (Forth Worth, United States, July 23-28, 2017).

7.2.3 International Journals (Submitted, Under Review and Ready to Submit)

- Pirrone, D., Bovolo, F., Bruzzone, L., "A Novel Framework for Unsupervised Multiclass Change Detection in Dual-pol Intensity SAR Images" , In IEEE Transactions of Geoscience and Remote Sensing (ready to submit).

- Pirrone, D., De, S., Bhattacharya, A., Bruzzone, L., Bovolo, F., "An Unsupervised Approach to Change Detection in Built-Up Areas by Multi-Temporal Full-pol SAR Images" , In IEEE Geoscience and Remote Sensing Letters (submitted).

- Pirrone, D., Bovolo, F., Bruzzone, L., "An Approach to Unsupervised Detection of Fully and Partially Destroyed Buildings in Multi-temporal VHR SAR Images" In IEEE Transactions of Geoscience and Remote Sensing (ready to submit).

Bibliography

[1] Sardegna clima onlus homepage. `http:/http://sardegna-clima.it/`. Accessed: 2010-09-30.

[2] United nations institute for training and research (unitar) homepage. `http://www.unitar.org/`. Accessed: 2010-09-30.

[3] Aiazzi, Bruno; Alparone, Luciano, and Baronti, Stefano. Multiresolution local-statistics speckle filtering based on a ratio laplacian pyramid. *IEEE Transactions on Geoscience and Remote Sensing*, 36(5):1466–1476, 1998.

[4] Aiazzi, Bruno; Alparone, Luciano; Baronti, Stefano; Garzelli, Andrea, and Zoppetti, Claudia. Nonparametric change detection in multitemporal sar images based on mean-shift clustering. *IEEE Transactions on Geoscience and Remote Sensing*, 51(4):2022–2031, 2013.

[5] Aiazzi, Bruno; Bovolo, Francesca; Bruzzone, Lorenzo; Garzelli, Andrea; Pirrone, Davide, and Zoppetti, Claudia. Change detection in multitemporal images through single-and multi-scale approaches. In *Mathematical Models for Remote Sensing Image Processing*, pages 325–355. Springer, 2018.

[6] Akbari, Vahid; Anfinsen, Stian N; Doulgeris, Anthony P; Eltoft, Torbjørn; Moser, Gabriele, and Serpico, Sebastiano B. Polarimetric sar change detection with the complex hotelling–lawley trace statistic. *IEEE Transactions on Geoscience and Remote Sensing*, 54(7):3953–3966, 2016.

[7] Alparone, Luciano; Aiazzi, Bruno; Baronti, Stefano; Garzelli, Andrea, and Nencini, Filippo. Robust change analysis of sar data through information-theoretic multitemporal features. In *Geoscience and Remote Sensing Symposium, 2007. IGARSS 2007. IEEE International*, pages 3883–3886. IEEE, 2007.

[8] Amici, G; Dell'Acqua, F; Gamba, P, and Pulina, G. A comparison of fuzzy and neuro-fuzzy data fusion for flooded area mapping using sar images. *International journal of remote sensing*, 25(20):4425–4430, 2004.

[9] An, Liqiang; Zhang, Jingfa; Gong, Lixia, and Li, Qiang. Integration of sar image and vulnerability data for building damage degree estimation. In *Geoscience and Remote Sensing Symposium (IGARSS), 2016 IEEE International*, pages 4263–4266. IEEE, 2016.

[10] Argenti, Fabrizio and Alparone, Luciano. Speckle removal from sar images in the undecimated wavelet domain. *IEEE Transactions on Geoscience and Remote Sensing*, 40(11):2363–2374, 2002.

[11] Atto, Abdourrahmane Mahamane; Trouvé, Emmanuel; Berthoumieu, Yannick, and Mercier, Grégoire. Multidate divergence matrices for the analysis of sar image time series. *IEEE Transactions on Geoscience and Remote Sensing*, 51(4):1922–1938, 2013.

[12] Atto, Abdourrahmane Mahamane; Trouvé, Emmanuel; Nicolas, Jean-Marie, and Lê, Thu Trang. Wavelet operators and multiplicative observation models—application to sar image time-series analysis. *IEEE Transactions on Geoscience and Remote Sensing*, 54(11):6606–6624, 2016.

[13] Auer, Stefan; Hinz, Stefan, and Bamler, Richard. Ray-tracing simulation techniques for understanding high-resolution sar images. *IEEE Transactions on Geoscience and Remote Sensing*, 48(3):1445–1456, 2010.

[14] Bai, Yanbing; Adriano, Bruno; Mas, Erick; Gokon, Hideomi, and Koshimura, Shunichi. Object-based building damage assessment methodology using only post event alos-2/palsar-2 dual polarimetric sar intensity images. *J. Disaster Res*, 12(2):259–271, 2017.

[15] Balz, Timo and Liao, Mingsheng. Building-damage detection using post-seismic high-resolution sar satellite data. *International Journal of Remote Sensing*, 31(13):3369–3391, 2010.

[16] Ban, Yifang and Hu, Hongtao. Radarsat fine-beam sar data for land-cover mapping and change detection in the rural-urban fringe of the greater toronto area. In *Urban Remote Sensing Joint Event, 2007*, pages 1–7. IEEE, 2007.

[17] Ban, Yifang and Yousif, Osama A. Multitemporal spaceborne sar data for urban change detection in china. *IEEE Journal of Selected Topics in Applied Earth Observations and Remote Sensing*, 5(4):1087–1094, 2012.

[18] Barber, C Bradford; Dobkin, David P, and Huhdanpaa, Hannu. The quickhull algorithm for convex hulls. *ACM Transactions on Mathematical Software (TOMS)*, 22(4):469–483, 1996.

[19] Barber, Jarred. A generalized likelihood ratio test for coherent change detection in polarimetric sar. *IEEE Geoscience and Remote Sensing Letters*, 12(9):1873–1877, 2015.

[20] Bargiel, Damian. A new method for crop classification combining time series of radar images and crop phenology information. *Remote Sensing of Environment*, 198:369–383, 2017.

[21] Baselice, Fabio; Ferraioli, Giampaolo, and Pascazio, Vito. Markovian change detection of urban areas using very high resolution complex sar images. *IEEE Geoscience and Remote Sensing Letters*, 11(5):995–999, 2014.

[22] Bazi, Yakoub; Bruzzone, Lorenzo, and Melgani, Farid. An unsupervised approach based on the generalized gaussian model to automatic change detection in multitemporal sar images. *IEEE Transactions on Geoscience and Remote Sensing*, 43(4):874–887, 2005.

[23] Bazi, Yakoub; Bruzzone, Lorenzo, and Melgani, Farid. Automatic identification of the number and values of decision thresholds in the log-ratio image for change detection in sar images. *IEEE Geoscience and Remote Sensing Letters*, 3(3):349–353, 2006.

[24] Bazi, Yakoub; Bruzzone, Lorenzo, and Melgani, Farid. Image thresholding based on the em algorithm and the generalized gaussian distribution. *Pattern Recognition*, 40(2):619–634, 2007.

[25] Bazi, Yakoub; Melgani, Farid; Bruzzone, Lorenzo, and Vernazza, Gianni. A genetic expectation-maximization method for unsupervised change detection in multitemporal sar imagery. *International Journal of Remote Sensing*, 30(24):6591–6610, 2009.

[26] Bhattacharya, Avik; Muhuri, Arnab; De, Shaunak; Manickam, Surendar, and Frery, Alejandro C. Modifying the yamaguchi four-component decomposition scattering powers using a stochastic distance. *IEEE Journal of Selected Topics in Applied Earth Observations and Remote Sensing*, 8(7):3497–3506, 2015.

[27] Biernacki, Christophe; Celeux, Gilles, and Govaert, Gérard. Choosing starting values for the em algorithm for getting the highest likelihood in multivariate gaussian mixture models. *Computational Statistics & Data Analysis*, 41(3-4):561–575, 2003.

[28] Bishop, Christopher M. Pattern recognition and machine learning, 2006. , 60(1):78–78, 2012.

[29] Blumberg, Dan G. Remote sensing of desert dune forms by polarimetric synthetic aperture radar (sar). *Remote Sensing of Environment*, 65(2):204–216, 1998.

[30] Bombrun, Lionel and Beaulieu, Jean-Marie. Fisher distribution for texture modeling of polarimetric sar data. *IEEE Geoscience and Remote Sensing Letters*, 5(3):512–516, 2008.

[31] Bouhlel, Nizar; Ginolhac, Guillaume; Jolibois, Eric, and Atto, Abdourrahmane. Multivariate statistical modeling for multi-temporal sar change detection using wavelet transforms. In *8th International Workshop on the Analysis of Multitemporal Remote Sensing Images (MultiTemp), 2015*, pages 1–4, 2015.

[32] Bovolo, Francesca and Bruzzone, Lorenzo. A detail-preserving scale-driven approach to change detection in multitemporal sar images. *IEEE Transactions on Geoscience and Remote Sensing*, 43(12):2963–2972, 2005.

[33] Bovolo, Francesca and Bruzzone, Lorenzo. A split-based approach to unsupervised change detection in large-size multitemporal images: Application to tsunami-damage assessment. *IEEE Transactions on Geoscience and Remote Sensing*, 45(6):1658–1670, 2007.

[34] Bovolo, Francesca and Bruzzone, Lorenzo. A theoretical framework for unsupervised change detection based on change vector analysis in the polar domain. *IEEE Transactions on Geoscience and Remote Sensing*, 45 (1):218–236, 2007.

[35] Bovolo, Francesca and Bruzzone, Lorenzo. An adaptive technique based on similarity measures for change detection in very high resolution sar images. In *Geoscience and Remote Sensing Symposium, 2008. IGARSS 2008. IEEE International*, volume 3, pages III–158. IEEE, 2008.

[36] Bovolo, Francesca and Bruzzone, Lorenzo. The time variable in data fusion: A change detection perspective. *IEEE Geoscience and Remote Sensing Magazine*, 3:8–26, 2015.

[37] Bovolo, Francesca and Bruzzone, Lorenzo. The time variable in data fusion: A change detection perspective. *IEEE Geosci. Remote Sens. Mag*, 3(3):8–26, 2015.

[38] Bovolo, Francesca; Marchesi, Silvia, and Bruzzone, Lorenzo. A framework for automatic and unsupervised detection of multiple changes in multitemporal images. *IEEE Transactions on Geoscience and Remote Sensing*, 50(6):2196–2212, 2012.

[39] Bovolo, Francesca; Marin, Carlo, and Bruzzone, Lorenzo. A hierarchical approach to change detection in very high resolution sar images for surveillance applications. *IEEE Transactions on Geoscience and Remote Sensing*, 51(4):2042–2054, 2013.

[40] Breit, Helko; Fritz, Thomas; Balss, Ulrich; Lachaise, Marie; Niedermeier, Andreas, and Vonavka, Martin. Terrasar-x sar processing and products. *IEEE Transactions on Geoscience and Remote Sensing*, 48(2): 727–740, 2010.

[41] Brenner, Andreas R and Roessing, Ludwig. Radar imaging of urban areas by means of very high-resolution sar and interferometric sar. *IEEE Transactions on Geoscience and Remote Sensing*, 46(10):2971–2982, 2008.

[42] Brett, Peter TB and Guida, Raffaella. Earthquake damage detection in urban areas using curvilinear features. *IEEE Trans. Geoscience and Remote Sensing*, 51(9):4877–4884, 2013.

[43] Brisco, Brian; Schmitt, Andreas; Murnaghan, Kevin; Kaya, S, and Roth, Achim. Sar polarimetric change detection for flooded vegetation. *International Journal of Digital Earth*, 6(2):103–114, 2013.

[44] Brunner, Dominik; Lemoine, Guido, and Bruzzone, Lorenzo. Earthquake damage assessment of buildings using vhr optical and sar imagery. *IEEE Transactions on Geoscience and Remote Sensing*, 48(5):2403–2420, 2010.

[45] Bruzzone, Lorenzo; Marconcini, Mattia; Wegmuller, U, and Wiesmann, Andreas. An advanced system for the automatic classification of multitemporal sar images. *IEEE Transactions on Geoscience and Remote Sensing*, 42(6):1321–1334, 2004.

[46] Bujor, Florentin; Trouvé, Emmanuel; Valet, Lionel; Nicolas, J-M, and Rudant, J-P. Application of log-cumulants to the detection of spatiotemporal discontinuities in multitemporal sar images. *IEEE Transactions on Geoscience and Remote Sensing*, 42(10):2073–2084, 2004.

[47] Buono, Andrea; Nunziata, Ferdinando, and Migliaccio, Maurizio. Analysis of full and compact polarimetric sar features over the sea surface. *IEEE Geoscience and Remote Sensing Letters*, 13(10):1527–1531, 2016.

[48] Cao, Fang; Hong, Wen; Wu, Yirong, and Pottier, Eric. An unsupervised segmentation with an adaptive number of clusters using the span/h/α/a space and the complex wishart clustering for fully polarimetric sar data analysis. *IEEE Transactions on Geoscience and Remote Sensing*, 45(11):3454–3467, 2007.

[49] Capodici, Fulvio; D'Urso, Guido, and Maltese, Antonino. Investigating the relationship between x-band sar data from cosmo-skymed satellite and ndvi for lai detection. *Remote Sensing*, 5(3):1389–1404, 2013.

[50] Capodici, Fulvio; Maltese, Antonino; Ciraolo, Giuseppe; D' Urso, Guido, and La Loggia, Goffredo. Power sensitivity analysis of multi-frequency, multi-polarized, multi-temporal sar data for soil-vegetation system variables characterization. *Remote Sensing*, 9(7):677, 2017.

[51] Carincotte, Cyril; Derrode, Stéphane, and Bourennane, Salah. Unsupervised change detection on sar images using fuzzy hidden markov chains. *IEEE Transactions on Geoscience and Remote Sensing*, 44(2):432–441, 2006.

[52] Carotenuto, Vincenzo; De Maio, Antonio; Clemente, Carmine, and Soraghan, John J. Invariant rules for multipolarization sar change detection. *IEEE Transactions on Geoscience and Remote Sensing*, 53(6): 3294–3311, 2015.

[53] Carotenuto, Vincenzo; De Maio, Antonio; Clemente, Carmine; Soraghan, John J, and Alfano, Giusi. Forcing scale invariance in multipolarization sar change detection. *IEEE Transactions on Geoscience and Remote Sensing*, 54(1):36–50, 2016.

[54] Celik, Turgay. Multiscale change detection in multitemporal satellite images. *IEEE Geoscience and Remote Sensing Letters*, 6(4):820–824, 2009.

[55] Celik, Turgay. A bayesian approach to unsupervised multiscale change detection in synthetic aperture radar images. *Signal processing*, 90(5):1471–1485, 2010.

[56] Celik, Turgay and Ma, Kai-Kuang. Multitemporal image change detection using undecimated discrete wavelet transform and active contours. *IEEE Transactions on Geoscience and Remote Sensing*, 49(2): 706–716, 2011.

[57] Cha, Miriam; Phillips, Rhonda D; Wolfe, Patrick J, and Richmond, Christ D. Two-stage change detection for synthetic aperture radar. *IEEE Trans. Geoscience and Remote Sensing*, 53(12):6547–6560, 2015.

[58] Che, Meiqin; Du, Peijun, and Gamba, Paolo. 2-and 3-d urban change detection with quad-polsar data. *IEEE Geoscience and Remote Sensing Letters*, 15(1):68–72, 2018.

[59] Chen, Bangqian; Xiao, Xiangming; Ye, Huichun; Ma, Jun; Doughty, Russell; Li, Xiangping; Zhao, Bin; Wu, Zhixiang; Sun, Rui; Dong, Jinwei, and others, . Mapping forest and their spatial–temporal changes from 2007 to 2015 in tropical hainan island by integrating alos/alos-2 l-band sar and landsat optical images. *IEEE Journal of Selected Topics in Applied Earth Observations and Remote Sensing*, 2018.

[60] Chen, Chia-Tang; Chen, Kun-Shan, and Lee, Jong-Sen. The use of fully polarimetric information for the fuzzy neural classification of sar images. *IEEE Transactions on Geoscience and Remote Sensing*, 41(9): 2089–2100, 2003.

[61] Chen, Si-Wei and Sato, Motoyuki. Tsunami damage investigation of built-up areas using multitemporal spaceborne full polarimetric sar images. *IEEE Transactions on Geoscience and Remote Sensing*, 51(4): 1985–1997, 2013.

[62] Chen, Si-Wei; Wang, Xue-Song, and Sato, Motoyuki. Urban damage level mapping based on scattering mechanism investigation using fully polarimetric sar data for the 3.11 east japan earthquake. *IEEE Transactions on Geoscience and Remote Sensing*, 54(12):6919–6929, 2016.

[63] Chini, Marco; Pierdicca, Nazzareno, and Emery, William J. Exploiting sar and vhr optical images to quantify damage caused by the 2003 bam earthquake. *IEEE Transactions on Geoscience and Remote Sensing*, 47(1):145–152, 2009.

[64] Cloude, Shane R and Pottier, Eric. A review of target decomposition theorems in radar polarimetry. *IEEE transactions on geoscience and remote sensing*, 34(2):498–518, 1996.

[65] Cloude, Shane R and Pottier, Eric. An entropy based classification scheme for land applications of polarimetric sar. *IEEE transactions on geoscience and remote sensing*, 35(1):68–78, 1997.

[66] Colesanti, Carlo; Ferretti, Alessandro; Novali, Fabrizio; Prati, Claudio, and Rocca, Fabio. Sar monitoring of progressive and seasonal ground deformation using the permanent scatterers technique. *IEEE Transactions on Geoscience and Remote Sensing*, 41(7):1685–1701, 2003.

[67] Conradsen, Knut; Nielsen, Allan Aasbjerg; Schou, Jesper, and Skriver, Henning. A test statistic in the complex wishart distribution and its application to change detection in polarimetric sar data. *IEEE Transactions on Geoscience and Remote Sensing*, 41(1):4–19, 2003.

[68] Conradsen, Knut; Nielsen, Allan Aasbjerg, and Skriver, Henning. Determining the points of change in time series of polarimetric sar data. *IEEE Transactions on Geoscience and Remote Sensing*, 54(5):3007–3024, 2016.

[69] Crismer, Fabrizio; Moser, Gabriele; Krylov, Vladimir A, and Serpico, Sebastiano B. Unsupervised change detection on synthetic aperture radar images with generalized gamma distribution. In *Geoscience and Remote Sensing Symposium (IGARSS), 2016 IEEE International*, pages 3350–3353. IEEE, 2016.

[70] Cui, Shiyong and Datcu, Mihai. Statistical wavelet subband modeling for multi-temporal sar change detection. *IEEE Journal of Selected Topics in Applied Earth Observations and Remote Sensing*, 5(4):1095, 2012.

[71] Cyin, Junjun and Yang, Jian. A change detector based on the optimization of polarimetric contrast. In *Geoscience and Remote Sensing Symposium (IGARSS), 2017 IEEE International*, pages 5334–5337. IEEE, 2017.

[72] Dabboor, Mohammed; Collins, Michael J; Karathanassi, Vassilia, and Braun, Alexander. An unsupervised classification approach for polarimetric sar data based on the chernoff distance for complex wishart distribution. *IEEE Transactions on Geoscience and Remote Sensing*, 51(7):4200–4213, 2013.

[73] D'Addabbo, Annarita; Refice, Alberto; Pasquariello, Guido; Lovergine, Francesco P; Capolongo, Domenico, and Manfreda, Salvatore. A bayesian network for flood detection combining sar imagery and ancillary data. *IEEE Transactions on Geoscience and Remote Sensing*, 54(6):3612–3625, 2016.

[74] Del Frate, Fabio; Pacifici, Fabio, and Solimini, Domenico. Monitoring urban land cover in rome, italy, and its changes by single-polarization multitemporal sar images. *IEEE Journal of Selected Topics in Applied Earth Observations and Remote Sensing*, 1(2):87–97, 2008.

[75] Dell'Acqua, Fabio; Bignami, Christian; Chini, Marco; Lisini, Gianni; Polli, Diego Aldo, and Stramondo, Salvatore. Earthquake damages rapid mapping by satellite remote sensing data: L'aquila april 6th, 2009 event. *IEEE Journal of Selected Topics in Applied Earth Observations and Remote Sensing*, 4(4):935–943, 2011.

[76] Derrode, S; Mercier, G, and Pieczynski, W. Unsupervised change detection in sar images using a multicomponent hmc model. In *Analysis Of Multi-Temporal Remote Sensing Images*, pages 195–203. World Scientific, 2004.

[77] Domínguez, Elías Méndez; Meier, Erich; Small, David; Schaepman, Michael E; Bruzzone, Lorenzo, and Henke, Daniel. A multisquint framework for change detection in high-resolution multitemporal sar images. *IEEE Transactions on Geoscience and Remote Sensing*, 56(6):3611–3623, 2018.

[78] Doulgeris, Anthony P; Anfinsen, Stian Normann, and Eltoft, Torbjørn. Classification with a non-gaussian model for polsar data. *IEEE Transactions on Geoscience and Remote Sensing*, 46(10):2999–3009, 2008.

[79] Doulgeris, Anthony P; Akbari, Vahid, and Eltoft, Torbjorn. Automatic polsar segmentation with the u-distribution and markov random fields. In *Synthetic Aperture Radar, 2012. EUSAR. 9th European Conference on*, pages 183–186. VDE, 2012.

[80] Duda, Richard O; Hart, Peter E, and Stork, David G. *Pattern classification*. John Wiley & Sons, 2012.

[81] Erten, Esra; Chesnokova, Olga; Rossi, Cristian, and Hajnsek, Irena. A polarimetric temporal scene parameter and its application to change detection. In *Geoscience and Remote Sensing Symposium (IGARSS), 2011 IEEE International*, pages 1091–1094. IEEE, 2011.

[82] Erten, Esra; Reigber, Andreas; Ferro-Famil, Laurent, and Hellwich, Olaf. A new coherent similarity measure for temporal multichannel scene characterization. *IEEE Transactions on Geoscience and Remote Sensing*, 50(7):2839–2851, 2012.

[83] Ferro, Adamo; Brunner, Dominik; Bruzzone, Lorenzo, and Lemoine, Guido. On the relationship between double bounce and the orientation of buildings in vhr sar images. *IEEE Geoscience and Remote Sensing Letters*, 8(4):612–616, 2011.

[84] Ferro-Famil, Laurent; Pottier, Eric, and Lee, Jong-Sen. Unsupervised classification of multifrequency and fully polarimetric sar images based on the h/a/alpha-wishart classifier. *Geoscience and Remote Sensing, IEEE Transactions on*, 39(11):2332–2342, 2001.

[85] Floricioiu, Dana and Rott, Helmut. Seasonal and short-term variability of multifrequency, polarimetric radar backscatter of alpine terrain from sir-c/x-sar and airsar data. *IEEE Transactions on Geoscience and Remote Sensing*, 39(12):2634–2648, 2001.

[86] Foody, Giles M. On the compensation for chance agreement in image classification accuracy assessment, photogram. *Eng. Remote Sens.*, 58:1459–1460, 1992.

[87] Franceschetti, Giorgio; Iodice, Antonio, and Riccio, Daniele. A canonical problem in electromagnetic backscattering from buildings. *IEEE Transactions on Geoscience and Remote Sensing*, 40(8):1787–1801, 2002.

[88] Franceschetti, Giorgio; Iodice, Antonio; Riccio, Daniele, and Ruello, Giuseppe. Sar raw signal simulation for urban structures. *IEEE Transactions on Geoscience and Remote Sensing*, 41(9):1986–1995, 2003.

[89] Freeman, Anthony and Durden, Stephen L. A three-component scattering model for polarimetric sar data. *IEEE Transactions on Geoscience and Remote Sensing*, 36(3):963–973, 1998.

[90] Frery, Alejandro César; Muller, H-J; Yanasse, Corina da Costa Freitas, and Sant'Anna, Sidnei João Siqueira. A model for extremely heterogeneous clutter. *IEEE transactions on geoscience and remote sensing*, 35(3): 648–659, 1997.

[91] Fukuda, Seisuke and Hirosawa, Haruto. A wavelet-based texture feature set applied to classification of multifrequency polarimetric sar images. *IEEE Transactions on Geoscience and Remote Sensing*, 37(5): 2282–2286, 1999.

[92] Galland, Frédéric; Nicolas, Jean-Marie; Sportouche, Hélène; Roche, Muriel; Tupin, Florence, and Réfrégier, Philippe. Unsupervised synthetic aperture radar image segmentation using fisher distributions. *IEEE Transactions on Geoscience and Remote Sensing*, 47(8):2966–2972, 2009.

[93] Gamba, Paolo; Dell'Acqua, Fabio, and Lisini, Gianni. Change detection of multitemporal sar data in urban areas combining feature-based and pixel-based techniques. *IEEE Transactions on Geoscience and Remote Sensing*, 44(10):2820–2827, 2006.

[94] Gamba, Paolo; Dell'Acqua, Fabio, and Trianni, Giovanna. Rapid damage detection in the bam area using multitemporal sar and exploiting ancillary data. *IEEE Transactions on Geoscience and Remote Sensing*, 45(6):1582–1589, 2007.

[95] Garzelli, Andrea and Zoppetti, Claudia. Optimizing sar change detection based on log-ratio features. In *Analysis of Multitemporal Remote Sensing Images (MultiTemp), 2017 9th International Workshop on the*, pages 1–4. IEEE, 2017.

[96] Ghanbari, M; Akbari, V; Abkar, AA, and Sahebi, MR. Minimum-error thresholding for unsupervised change detection in multilook polarimetric sar images. *Journal of Geomatics Science and Technology*, 5(2):17–29, 2015.

[97] Gimeno, M; San-Miguel-Ayanz, J, and Schmuck, G. Identification of burnt areas in mediterranean forest environments from ers-2 sar time series. *International Journal of Remote Sensing*, 25(22):4873–4888, 2004.

[98] Giustarini, Laura; Hostache, Renaud; Matgen, Patrick; Schumann, Guy J-P; Bates, Paul D, and Mason, David C. A change detection approach to flood mapping in urban areas using terrasar-x. *IEEE transactions on Geoscience and Remote Sensing*, 51(4):2417–2430, 2013.

[99] Gong, Lixia; Wang, Chao; Wu, Fan; Zhang, Jingfa; Zhang, Hong, and Li, Qiang. Earthquake-induced building damage detection with post-event sub-meter vhr terrasar-x staring spotlight imagery. *Remote Sensing*, 8(11):887, 2016.

[100] Gong, Maoguo; Cao, Yu, and Wu, Qiaodi. A neighborhood-based ratio approach for change detection in sar images. *IEEE Geoscience and Remote Sensing Letters*, 9(2):307–311, 2012.

[101] Gong, Maoguo; Zhou, Zhiqiang, and Ma, Jingjing. Change detection in synthetic aperture radar images based on image fusion and fuzzy clustering. *IEEE Transactions on Image Processing*, 21(4):2141–2151, 2012.

[102] Gong, Maoguo; Su, Linzhi; Jia, Meng, and Chen, Weisheng. Fuzzy clustering with a modified mrf energy function for change detection in synthetic aperture radar images. *IEEE Transactions on Fuzzy Systems*, 22 (1):98–109, 2014.

[103] Gong, Maoguo; Zhao, Jiaojiao; Liu, Jia; Miao, Qiguang, and Jiao, Licheng. Change detection in synthetic aperture radar images based on deep neural networks. *IEEE transactions on neural networks and learning systems*, 27(1):125–138, 2016.

[104] Goodenough, David G; Chen, Hao; Richardson, Ashlin; Cloude, Shane; Hong, Wen, and Li, Yang. Mapping fire scars using radarsat-2 polarimetric sar data. *Canadian Journal of Remote Sensing*, 37(5):500–509, 2012.

[105] Guida, Raffaella; Iodice, Antonio; Riccio, Daniele, and Stilla, Uwe. Model-based interpretation of high-resolution sar images of buildings. *IEEE Journal of Selected Topics in Applied Earth Observations and Remote Sensing*, 1(2):107–119, 2008.

[106] Hajnsek, Irena; Pottier, Eric, and Cloude, Shane R. Inversion of surface parameters from polarimetric sar. *IEEE Transactions on Geoscience and Remote Sensing*, 41(4):727–744, 2003.

[107] Hajnsek, Irena; Jagdhuber, Thomas; Schon, Helmut, and Papathanassiou, Konstantinos Panagiotis. Potential of estimating soil moisture under vegetation cover by means of polsar. *IEEE Transactions on Geoscience and Remote Sensing*, 47(2):442–454, 2009.

[108] Hou, Biao; Wei, Qian; Zheng, Yaoguo, and Wang, Shuang. Unsupervised change detection in sar image based on gauss-log ratio image fusion and compressed projection. *IEEE J. Sel. Top. Appl. Earth Obs. Remote Sens*, 7(8):3297–3317, 2014.

[109] Hu, Hongtao and Ban, Yifang. Unsupervised change detection in multitemporal sar images over large urban areas. *IEEE Journal of Selected Topics in Applied Earth Observations and Remote Sensing*, 7(8):3248–3261, 2014.

[110] Huang, Lei; Li, Zhen; Tian, Bang-Sen; Chen, Quan; Liu, Jiu-Liang, and Zhang, Rui. Classification and snow line detection for glacial areas using the polarimetric sar image. *Remote sensing of environment*, 115 (7):1721–1732, 2011.

[111] Huang, Xiaojing; Yang, Wen; Xia, Gui-Song, and Liao, Mingsheng. Superpixel-based change detection in high resolution sar images using region covariance features. In *Analysis of Multitemporal Remote Sensing Images (Multi-Temp), 2015 8th International Workshop on the*, pages 1–4. IEEE, 2015.

[112] Hussain, Masroor; Chen, Dongmei; Cheng, Angela; Wei, Hui, and Stanley, David. Change detection from remotely sensed images: From pixel-based to object-based approaches. *ISPRS Journal of photogrammetry and remote sensing*, 80:91–106, 2013.

[113] Inglada, Jordi and Grégoire, Mercier. A new statistical similarity measure for change detection in multitemporal sar images and its extension to multiscale change analysis. *IEEE transactions on geoscience and remote sensing*, 45(5):1432–1445, 2007.

[114] Jia, Kun; Li, Qiangzi; Tian, Yichen; Wu, Bingfang; Zhang, Feifei, and Meng, Jihua. Crop classification using multi-configuration sar data in the north china plain. *International Journal of Remote Sensing*, 33 (1):170–183, 2012.

[115] Jia, Lu; Li, Ming; Zhang, Peng; Wu, Yan, and Zhu, Huahui. Sar image change detection based on multiple kernel k-means clustering with local-neighborhood information. *IEEE Geoscience and Remote Sensing Letters*, 13(6):856–860, 2016.

[116] Jiao, Licheng and Liu, Fang. Wishart deep stacking network for fast polsar image classification. *IEEE Transactions on Image Processing*, 25(7):3273–3286, 2016.

[117] Kim, Duk-jin; Hensley, Scott; Yun, Sang-Ho, and Neumann, Maxim. Detection of durable and permanent changes in urban areas using multitemporal polarimetric uavsar data. *IEEE Geoscience and Remote Sensing Letters*, 13(2):267–271, 2016.

[118] Kim, Yunjin and van Zyl, Jakob J. A time-series approach to estimate soil moisture using polarimetric radar data. *IEEE Transactions on Geoscience and Remote Sensing*, 47(8):2519–2527, 2009.

[119] Kuny, Silvia; Schulz, Karsten, and Hammer, Horst. Signature analysis of destroyed buildings in simulated high resolution sar data. In *Geoscience and Remote Sensing Symposium (IGARSS), 2013 IEEE International*, pages 903–906. IEEE, 2013.

[120] Kuruoglu, Ercan E and Zerubia, Josiane. Modeling sar images with a generalization of the rayleigh distribution. *IEEE Transactions on Image Processing*, 13(4):527–533, 2004.

[121] Lavalle, Marco. A new automated algorithm for detecting forest disturbances with the dual-polarimetric sar alpha angle. In *Geoscience and Remote Sensing Symposium (IGARSS), 2017 IEEE International*, pages 5299–5302. IEEE, 2017.

[122] Lee, Jong-Sen and Pottier, Eric. *Polarimetric radar imaging: from basics to applications*. CRC press, 2009.

[123] Lee, Jong-Sen; Grunes, Mitchell R; Ainsworth, Thomas L; Du, Li-Jen; Schuler, Dale L, and Cloude, Shane R. Unsupervised classification using polarimetric decomposition and the complex wishart classifier. *Geoscience and Remote Sensing, IEEE Transactions on*, 37(5):2249–2258, 1999.

[124] Lee, Jong-Sen; Grunes, Mitchell R, and De Grandi, Gianfranco. Polarimetric sar speckle filtering and its implication for classification. *IEEE Transactions on Geoscience and remote sensing*, 37(5):2363–2373, 1999.

[125] Li, Hejing; Li, Ming; Zhang, Peng; Song, Wanying; An, Lin, and Wu, Yan. Sar image change detection based on hybrid conditional random field. *IEEE Geosci. Remote Sensing Lett.*, 12(4):910–914, 2015.

[126] Li, Heng-Chao; Hong, Wen; Wu, Yi-Rong, and Fan, Ping-Zhi. An efficient and flexible statistical model based on generalized gamma distribution for amplitude sar images. *IEEE Transactions on Geoscience and Remote Sensing*, 48(6):2711–2722, 2010.

[127] Li, Heng-Chao; Celik, Turgay; Longbotham, Nathan, and Emery, William J. Gabor feature based unsupervised change detection of multitemporal sar images based on two-level clustering. *IEEE Geoscience and Remote Sensing Letters*, 12(12):2458–2462, 2015.

[128] Li, Shutao; Fang, Leyuan, and Yin, Haitao. Multitemporal image change detection using a detail-enhancing approach with nonsubsampled contourlet transform. *IEEE Geoscience and Remote Sensing Letters*, 9(5): 836–840, 2012.

[129] Lillesand, Thomas; Kiefer, Ralph W, and Chipman, Jonathan. *Remote sensing and image interpretation*. John Wiley & Sons, 2014.

[130] Liu, Canran; Frazier, Paul, and Kumar, Lalit. Comparative assessment of the measures of thematic classification accuracy. *Remote sensing of environment*, 107(4):606–616, 2007.

[131] Liu, Jia; Gong, Maoguo; Qin, Kai, and Zhang, Puzhao. A deep convolutional coupling network for change detection based on heterogeneous optical and radar images. *IEEE transactions on neural networks and learning systems*, 2016.

[132] Liu, Meng; Zhang, Hong; Wang, Chao, and Wu, Fan. Change detection of multilook polarimetric sar images using heterogeneous clutter models. *IEEE Transactions on Geoscience and Remote Sensing*, 52(12): 7483–7494, 2014.

[133] Liu, Sicong; Bruzzone, Lorenzo; Bovolo, Francesca, and Du, Peijun. Hierarchical unsupervised change detection in multitemporal hyperspectral images. *IEEE Transactions on Geoscience and Remote Sensing*, 53(1):244–260, 2015.

[134] Liu, Wensong; Yang, Jie; Zhao, Jinqi, and Yang, Le. A novel method of unsupervised change detection using multi-temporal polsar images. *Remote Sensing*, 9(11):1135, 2017.

[135] Liu, Wensong; Yang, Jie; Zhao, Jinqi; Shi, Hongtao, and Yang, Le. An unsupervised change detection method using time-series of polsar images from radarsat-2 and gaofen-3. *Sensors*, 18(2):559, 2018.

[136] Lopez, C Villamil; Kempf, T; Speck, R; Anglberger, H, and Stilla, U. Automatic change detection using very high-resolution sar images and prior knowledge about the scene. In *Radar Sensor Technology XXI*, volume 10188, page 1018805. International Society for Optics and Photonics, 2017.

[137] Lopez-Martinez, Carlos; Pottier, Eric, and Cloude, Shane R. Statistical assessment of eigenvector-based target decomposition theorems in radar polarimetry. *IEEE Transactions on Geoscience and Remote Sensing*, 43(9):2058–2074, 2005.

[138] Lopez-Sanchez, Juan M; Cloude, Shane R, and Ballester-Berman, J David. Rice phenology monitoring by means of sar polarimetry at x-band. *IEEE Transactions on Geoscience and Remote Sensing*, 50(7): 2695–2709, 2012.

[139] Lu, Dengsheng; Mausel, P; Brondizio, E, and Moran, Emilio. Change detection techniques. *International journal of remote sensing*, 25(12):2365–2401, 2004.

[140] Lu, Jun; Li, Jonathan; Chen, Gang; Zhao, Linjun; Xiong, Boli, and Kuang, Gaoyao. Improving pixel-based change detection accuracy using an object-based approach in multitemporal sar flood images. *IEEE Journal of Selected Topics in Applied Earth Observations and Remote Sensing*, 8(7):3486–3496, 2015.

[141] Ma, Wenping; Jiao, Licheng; Gong, Maoguo, and Li, Congling. Image change detection based on an improved rough fuzzy c-means clustering algorithm. *International Journal of Machine Learning and Cybernetics*, 5(3):369–377, 2014.

[142] Mahdavi, Sahel; Salehi, Bahram; Amani, Meisam; Granger, Jean Elizabeth; Brisco, Brian; Huang, Weimin, and Hanson, Alan. Object-based classification of wetlands in newfoundland and labrador using multi-temporal polsar data. *Canadian Journal of Remote Sensing*, 43(5):432–450, 2017.

[143] Maître, Henri. *Processing of Synthetic Aperture Radar (SAR) Images*. John Wiley & Sons, 2013.

[144] Mallat, Stéphane. *A wavelet tour of signal processing*. Elsevier, 1999.

[145] Marchesi, Silvia; Bovolo, Francesca, and Bruzzone, Lorenzo. A context-sensitive technique robust to registration noise for change detection in vhr multispectral images. *IEEE transactions on Image Processing*, 19 (7):1877–1889, 2010.

[146] Marin, Carlo; Bovolo, Francesca, and Bruzzone, Lorenzo. Building change detection in multitemporal very high resolution sar images. *IEEE Transactions on Geoscience and Remote Sensing*, 53(5):2664–2682, 2015.

[147] Marino, Armando and Alonso-González, Alberto. An optimization of the difference of covariance matrices for polsar change detection. In *Geoscience and Remote Sensing Symposium (IGARSS), 2017 IEEE International*, pages 5315–5318. IEEE, 2017.

[148] Marino, Armando and Hajnsek, Irena. A change detector based on an optimization with polarimetric sar imagery. *IEEE Transactions on Geoscience and Remote Sensing*, 52(8):4781–4798, 2014.

[149] Marino, Armando; Cloude, Shane R, and Lopez-Sanchez, Juan M. A new polarimetric change detector in radar imagery. *IEEE Transactions on Geoscience and Remote Sensing*, 51(5):2986–3000, 2013.

[150] Matsuoka, Masashi and Yamazaki, Fumio. Use of satellite sar intensity imagery for detecting building areas damaged due to earthquakes. *Earthquake Spectra*, 20(3):975–994, 2004.

[151] McNairn, H and Brisco, B. The application of c-band polarimetric sar for agriculture: a review. *Canadian Journal of Remote Sensing*, 30(3):525–542, 2004.

[152] Mian, Ammar; Ovarlez, Jean-Philippe; Ginolhac, Guillaume, and Atto, Abdourahmane M. A robust change detector for highly heterogeneous multivariate images. In *2018 IEEE International Conference on Acoustics, Speech and Signal Processing (ICASSP)*, pages 3429–3433. IEEE, 2018.

[153] Michel, Rémi; Avouac, Jean-Philippe, and Taboury, Jean. Measuring near field coseismic displacements from sar images: Application to the landers earthquake. *Geophysical Research Letters*, 26(19):3017–3020, 1999.

[154] Miura, Hiroyuki; Midorikawa, Saburoh, and Matsuoka, Masashi. Building damage assessment using high-resolution satellite sar images of the 2010 haiti earthquake. *Earthquake Spectra*, 32(1):591–610, 2016.

[155] Moran, M Susan; Alonso, Luis; Moreno, Jose F; Mateo, Maria Pilar Cendrero; De La Cruz, D Fernando, and Montoro, Amelia. A radarsat-2 quad-polarized time series for monitoring crop and soil conditions in barrax, spain. *IEEE Transactions on Geoscience and Remote Sensing*, 50(4):1057–1070, 2012.

[156] Moser, Gabriele and Serpico, Sebastiano B. Generalized minimum-error thresholding for unsupervised change detection from sar amplitude imagery. *IEEE Transactions on Geoscience and Remote Sensing*, 44 (10):2972–2982, 2006.

[157] Moser, Gabriele and Serpico, Sebastiano B. Unsupervised change detection from multichannel sar data by markovian data fusion. *IEEE Transactions on Geoscience and Remote Sensing*, 47(7):2114–2128, 2009.

[158] Moser, Gabriele; Serpico, Sebastiano, and Vernazza, Gianni. Unsupervised change detection from multichannel sar images. *IEEE Geoscience and Remote Sensing Letters*, 4(2):278–282, 2007.

[159] Muhuri, Arnab; Manickam, Surendar, and Bhattacharya, Avik. Scattering mechanism based snow cover mapping using radarsat-2 c-band polarimetric sar data. *IEEE Journal of Selected Topics in Applied Earth Observations and Remote Sensing*, 10(7):3213–3224, 2017.

[160] Mullissa, Adugna G; Persello, Claudio, and Tolpekin, Valentyn. Fully convolutional networks for multitemporal sar image classification. In *IGARSS 2018-2018 IEEE International Geoscience and Remote Sensing Symposium*, pages 6635–6638. IEEE, 2018.

[161] Nascimento, Abraão DC; Frery, Alejandro C, and Cintra, Renato J. Detecting changes in fully polarimetric sar imagery with statistical information theory. *arXiv preprint arXiv:1801.08901*, 2018.

[162] Nielsen, Allan Aasbjerg; Conradsen, Knut, and Skriver, Henning. Change detection in full and dual polarization, single-and multifrequency sar data. *IEEE Journal of Selected Topics in Applied Earth Observations and Remote Sensing*, 8(8):4041–4048, 2015.

[163] Novak, Leslie M. Change detection for multi-polarization multi-pass sar. In *Algorithms for Synthetic Aperture Radar Imagery XII*, volume 5808, pages 234–247. International Society for Optics and Photonics, 2005.

[164] Oh, Yisok; Sarabandi, Kamal, and Ulaby, Fawwaz T. Semi-empirical model of the ensemble-averaged differential mueller matrix for microwave backscattering from bare soil surfaces. *IEEE Transactions on Geoscience and Remote Sensing*, 40(6):1348–1355, 2002.

[165] Oliver, Chris and Quegan, Shaun. *Understanding synthetic aperture radar images*. SciTech Publishing, 2004.

[166] Paloscia, S; Pettinato, S; Santi, E; Notarnicola, C; Pasolli, L, and Reppucci, A. Soil moisture mapping using sentinel-1 images: Algorithm and preliminary validation. *Remote Sensing of Environment*, 134:234–248, 2013.

[167] Park, Sang-Eun; Yamaguchi, Yoshio, and Kim, Duk-jin. Polarimetric sar remote sensing of the 2011 tohoku earthquake using alos/palsar. *Remote sensing of Environment*, 132:212–220, 2013.

[168] Park, Sang-Eun; Yamaguchi, Yoshio; Singh, Gulab; Yamaguchi, Satoru, and Whitaker, Andrew C. Polarimetric sar response of snow-covered area observed by multi-temporal alos palsar fully polarimetric mode. *IEEE Transactions on Geoscience and Remote Sensing*, 52(1):329–340, 2014.

[169] Pham, Minh-Tan; Mercier, Grégoire, and Michel, Julien. Change detection between sar images using a pointwise approach and graph theory. *IEEE Trans. Geoscience and Remote Sensing*, 54(4):2020–2032, 2016.

[170] Pirrone, Davide; Bovolo, Francesca, and Bruzzone, Lorenzo. Analysis of backscattering behaviors for partially damaged buildings in vhr sar images. In *Image and Signal Processing for Remote Sensing XXI*, volume 9643, page 96431D. International Society for Optics and Photonics, 2015.

[171] Pirrone, Davide; Bovolo, Francesca, and Bruzzone, Lorenzo. A novel framework for change detection in bitemporal polarimetric sar images. In *SPIE Remote Sensing*, pages 100040Z–100040Z. International Society for Optics and Photonics, 2016.

[172] Pirrone, Davide; De, Shaunak; Bhattacharya, Avik; Bruzzone, Lorenzo, and Bovolo, Francesca. Unsupervised change detection in built-up areas by multi-temporal polarimetric sar images. In *Geoscience and Remote Sensing Symposium (IGARSS), 2017 IEEE International*, pages 4554–4557. IEEE, 2017.

[173] Poulain, Vincent; Inglada, Jordi; Spigai, Marc; Tourneret, Jean-Yves, and Marthon, Philippe. Fusion of high resolution optical and sar images with vector data bases for change detection. In *Geoscience and Remote Sensing Symposium, 2009 IEEE International, IGARSS 2009*, volume 4, pages IV–956. IEEE, 2009.

[174] Qi, Zhixin; Yeh, Anthony Gar-On; Li, Xia, and Lin, Zheng. A novel algorithm for land use and land cover classification using radarsat-2 polarimetric sar data. *Remote Sensing of Environment*, 118:21–39, 2012.

[175] Qi, Zhixin; Yeh, Anthony Gar-On; Li, Xia, and Zhang, Xiaohu. A three-component method for timely detection of land cover changes using polarimetric sar images. *ISPRS Journal of Photogrammetry and Remote Sensing*, 107:3–21, 2015.

[176] Qong, Muhtar. Polarization state conformation and its application to change detection in polarimetric sar data. *IEEE Geoscience and remote sensing letters*, 1(4):304–308, 2004.

[177] Quartulli, Marco and Datcu, Mihai. Stochastic geometrical modeling for built-up area understanding from a single sar intensity image with meter resolution. *IEEE Transactions on geoscience and remote sensing*, 42(9):1996–2003, 2004.

[178] Quin, Guillaume; Pinel-Puyssegur, Beatrice; Nicolas, Jean-Marie, and Loreaux, Philippe. Mimosa: An automatic change detection method for sar time series. *IEEE Transactions on Geoscience and Remote Sensing*, 52(9):5349–5363, 2014.

[179] Ramsey III, Elijah; Rangoonwala, Amina; Suzuoki, Yukihiro, and Jones, Cathleen E. Oil detection in a coastal marsh with polarimetric synthetic aperture radar (sar). *Remote Sensing*, 3(12):2630–2662, 2011.

[180] Ratha, Debanshu; De, Shaunak; Celik, Turgay, and Bhattacharya, Avik. Change detection in polarimetric sar images using a geodesic distance between scattering mechanisms. *IEEE Geoscience and Remote Sensing Letters*, 14(7):1066–1070, 2017.

[181] Reigber, Andreas; Jäger, M; Neumann, Maxim, and Ferro-Famil, Laurent. Classifying polarimetric sar data by combining expectation methods with spatial context. *International Journal of Remote Sensing*, 31(3): 727–744, 2010.

[182] Richards, John Alan and others, . *Remote sensing with imaging radar*, volume 1. Springer, 2009.

[183] Ridd, Merrill K and Liu, Jiajun. A comparison of four algorithms for change detection in an urban environment. *Remote sensing of environment*, 63(2):95–100, 1998.

[184] Rignot, Eric JM and Van Zyl, Jakob J. Change detection techniques for ers-1 sar data. *IEEE Transactions on Geoscience and Remote sensing*, 31(4):896–906, 1993.

[185] Ródenas, Josep A and Garello, René. Internal wave detection and location in sar images using wavelet transform. *IEEE transactions on geoscience and remote sensing*, 36(5):1494–1507, 1998.

[186] Ross, Timothy J. *Fuzzy logic with engineering applications*. John Wiley & Sons, 2009.

[187] Sato, Akinobu; Yamaguchi, Yoshio; Singh, Gulab, and Park, Sang-Eun. Four-component scattering power decomposition with extended volume scattering model. *IEEE Geoscience and Remote Sensing Letters*, 9 (2):166–170, 2012.

[188] Schellenberger, Thomas; Ventura, Bartolomeo; Zebisch, Marc, and Notarnicola, Claudia. Wet snow cover mapping algorithm based on multitemporal cosmo-skymed x-band sar images. *IEEE Journal of Selected Topics in Applied Earth Observations and Remote Sensing*, 5(3):1045–1053, 2012.

[189] Schmitt, Andreas; Brisco, Brian; Kaya, Shannon, and Murnaghan, Kevin. Polarimetric change detection for wetlands. *IAHS Red Book*, 2010.

[190] Schmitt, Andreas; Wessel, Birgit, and Roth, Achim. An innovative curvelet-only-based approach for automated change detection in multi-temporal sar imagery. *Remote Sensing*, 6(3):2435–2462, 2014.

[191] Shao, Pan; Shi, Wenzhong; He, Pengfei; Hao, Ming, and Zhang, Xiaokang. Novel approach to unsupervised change detection based on a robust semi-supervised fcm clustering algorithm. *Remote Sensing*, 8(3):264, 2016.

[192] Shi, Jiao; Wu, Jiaji; Paul, Anand; Jiao, Licheng, and Gong, Maoguo. Change detection in synthetic aperture radar images based on fuzzy active contour models and genetic algorithms. *Mathematical Problems in Engineering*, 2014, 2014.

[193] Shibayama, Takashi and Yamaguchi, Yoshio. A landslide detection based on the change of scattering power components between multi-temporal polsar data. In *Geoscience and Remote Sensing Symposium (IGARSS), 2014 IEEE International*, pages 2734–2737. IEEE, 2014.

[194] Shu, Yuanming; Li, Jonathan; Yousif, Hamad, and Gomes, Gary. Dark-spot detection from sar intensity imagery with spatial density thresholding for oil-spill monitoring. *Remote Sensing of Environment*, 114(9): 2026–2035, 2010.

[195] Silva, Wagner B; Freitas, Corina C; Sant'Anna, Sidnei JS, and Frery, Alejandro C. Classification of segments in polsar imagery by minimum stochastic distances between wishart distributions. *IEEE Journal of Selected Topics in Applied Earth Observations and Remote Sensing*, 6(3):1263–1273, 2013.

[196] Singh, Gulab; Yamaguchi, Yoshio; Boerner, Wolfgang-Martin, and Park, Sang-Eun. Monitoring of the march 11, 2011, off-tohoku 9.0 earthquake with super-tsunami disaster by implementing fully polarimetric high-resolution polsar techniques. *Proceedings of the IEEE*, 101(3):831–846, 2013.

[197] Su, Linzhi; Gong, Maoguo; Sun, Bo, and Jiao, Licheng. Unsupervised change detection in sar images based on locally fitting model and semi-em algorithm. *International journal of remote sensing*, 35(2):621–650, 2014.

[198] Su, Xin; Deledalle, Charles-Alban; Tupin, Florence, and Sun, Hong. Change detection and classification of multi-temporal sar series based on generalized likelihood ratio comparing-and-recognizing. In *Geoscience and Remote Sensing Symposium (IGARSS), 2014 IEEE International*, pages 1433–1436. IEEE, 2014.

[199] Su, Xin; Deledalle, Charles-Alban; Tupin, Florence, and Sun, Hong. Norcama: Change analysis in sar time series by likelihood ratio change matrix clustering. *ISPRS Journal of Photogrammetry and Remote Sensing*, 101:247–261, 2015.

[200] Tang, Kan; Sun, Xian; Sun, Hao, and Wang, Hongqi. A geometrical-based simulator for target recognition in high-resolution sar images. *IEEE Geoscience and Remote Sensing Letters*, 9(5):958–962, 2012.

[201] Tao, Mingliang; Zhou, Feng; Liu, Yan, and Zhang, Zijing. Tensorial independent component analysis-based feature extraction for polarimetric sar data classification. *IEEE Transactions on Geoscience and Remote Sensing*, 53(5):2481–2495, 2015.

[202] Tertulliani, Andrea; Rossi, Antonio; Cucci, Luigi, and Vecchi, Maurizio. L'aquila (central italy) earthquakes: The predecessors of the april 6, 2009 event. *Seismological Research Letters*, 80(6):1008–1013, 2009.

[203] Tison, Céline; Nicolas, J-M; Tupin, Florence, and Maître, Henri. A new statistical model for markovian classification of urban areas in high-resolution sar images. *IEEE transactions on geoscience and remote sensing*, 42(10):2046–2057, 2004.

[204] Torre, Andrea; Calabrese, Diego, and Porfilio, Manfredi. Cosmo-skymed: Image quality achievements. In *Recent Advances in Space Technologies (RAST), 2011 5th International Conference on*, pages 861–864. IEEE, 2011.

[205] Torres, Ramon; Snoeij, Paul; Geudtner, Dirk; Bibby, David; Davidson, Malcolm; Attema, Evert; Potin, Pierre; Rommen, BjÖrn; Floury, Nicolas; Brown, Mike, and others, . Gmes sentinel-1 mission. *Remote Sensing of Environment*, 120:9–24, 2012.

[206] Touzi, R. On the use of polarimetric sar data for ship detection. In *Geoscience and Remote Sensing Symposium, 1999. IGARSS'99 Proceedings. IEEE 1999 International*, volume 2, pages 812–814. IEEE, 1999.

[207] Trianni, Giovanna; Lisini, G; Gamba, Paolo, and Dell'Acqua, F. Fusion of gis and sar statistical features for earthquake damage mapping at the block scale. In *Machine Interpretation Of Patterns: Image Analysis and Data Mining*, pages 195–206. World Scientific, 2010.

[208] Ulaby, Fawwaz T and Dobson, M Craig. Handbook of radar scattering statistics for terrain (artech house remote sensing library). *Norwood, MA, USA: Artech House*, 1989.

[209] Ulaby, Fawwaz T; Moore, Richard K, and Fung, Adrian K. Microwave remote sensing active and passive. 2015.

[210] Uprety, Pralhad; Yamazaki, Fumio, and Dell'Acqua, Fabio. Damage detection using high-resolution sar imagery in the 2009 l'aquila, italy, earthquake. *Earthquake Spectra*, 29(4):1521–1535, 2013.

[211] Van Zyl, Jakob J; Arii, Motofumi, and Kim, Yunjin. Model-based decomposition of polarimetric sar covariance matrices constrained for nonnegative eigenvalues. *IEEE Transactions on Geoscience and Remote Sensing*, 49(9):3452–3459, 2011.

[212] Wang, Fan; Wu, Yan; Zhang, Qiang; Zhang, Peng; Li, Ming, and Lu, Yunlong. Unsupervised change detection on sar images using triplet markov field model. *IEEE Geoscience and Remote Sensing Letters*, 10 (4):697–701, 2013.

[213] Wang, Tian-Lin and Jin, Ya-Qiu. Postearthquake building damage assessment using multi-mutual information from pre-event optical image and postevent sar image. *IEEE Geoscience and Remote Sensing Letters*, 9(3):452–456, 2012.

[214] Wang, Yan; Du, Lan, and Dai, Hui. Unsupervised sar image change detection based on sift keypoints and region information. *IEEE Geoscience and Remote Sensing Letters*, 13(7):931–935, 2016.

[215] Whittle, Martin; Quegan, Shaun; Uryu, Yumiko; Stüewe, Michael, and Yulianto, Kokok. Detection of tropical deforestation using alos-palsar: A sumatran case study. *Remote sensing of environment*, 124:83–98, 2012.

[216] Wood, Derick and Yap, Chee K. The orthogonal convex skull problem. *Discrete & Computational Geometry*, 3(4):349–365, 1988.

[217] Wu, Fan; Shan, Jie, and Wang, Chao. Earthquake-induced collapsed building detection with vhr synthetic aperture radar images. 2017.

[218] Xia, Zong-Guo and Henderson, Floyd M. Understanding the relationships between radar response patterns and the bio-and geophysical parameters of urban areas. *IEEE Transactions on Geoscience and Remote Sensing*, 35(1):93–101, 1997.

[219] Xiong, Boli; Chen, Qi; Jiang, Yongmei, and Kuang, Gangyao. A threshold selection method using two sar change detection measures based on the markov random field model. *IEEE Geoscience and Remote Sensing Letters*, 9(2):287–291, 2012.

[220] Yamaguchi, Yoshio; Moriyama, Toshifumi; Ishido, Motoi, and Yamada, Hiroyoshi. Four-component scattering model for polarimetric sar image decomposition. *IEEE Transactions on Geoscience and Remote Sensing*, 43(8):1699–1706, 2005.

[221] Yan, Shiyong; Guo, Huadong; Liu, Guang, and Ruan, Zhixing. Mountain glacier displacement estimation using a dem-assisted offset tracking method with alos/palsar data. *Remote sensing letters*, 4(5):494–503, 2013.

[222] Yang, Wen; Song, Hui; Huang, Xiaojing; Xu, Xin, and Liao, Mingsheng. Change detection in high-resolution sar images based on jensen-shannon divergence and hierarchical markov model. *IEEE Journal of Selected Topics in Applied Earth Observations and Remote Sensing*, 7(8):3318–3327, 2014.

[223] Yang, Wen; Yang, Xiangli; Yan, Tianheng; Song, Hui, and Xia, Gui-Song. Region-based change detection for polarimetric sar images using wishart mixture models. *IEEE Transactions on Geoscience and Remote Sensing*, 54(11):6746–6756, 2016.

[224] Yousif, Osama and Ban, Yifang. Improving urban change detection from multitemporal sar images using pca-nlm. *IEEE Transactions on Geoscience and Remote Sensing*, 51(4):2032–2041, 2013.

[225] Yousif, Osama and Ban, Yifang. Improving sar-based urban change detection by combining map-mrf classifier and nonlocal means similarity weights. *IEEE Journal of Selected Topics in Applied Earth Observations and Remote Sensing*, 7(10):4288–4300, 2014.

[226] Yousif, Osama and Ban, Yifang. Object-based urban change detection using high resolution sar images. In *Urban Remote Sensing Event (JURSE), 2015 Joint*, pages 1–4. IEEE, 2015.

[227] Yueh, SH; Kong, Jin Au; Jao, JK; Shin, RT, and Novak, LM. K-distribution and polarimetric terrain radar clutter. *Journal of Electromagnetic Waves and Applications*, 3(8):747–768, 1989.

[228] Zhai, Wei and Huang, Chunlin. Fast building damage mapping using a single post-earthquake polsar image: a case study of the 2010 yushu earthquake. *Earth, Planets and Space*, 68(1):86, 2016.

[229] Zhang, Xiaohua; Chen, Jiawei, and Meng, Hongyun. A novel sar image change detection based on graph-cut and generalized gaussian model. *IEEE Geoscience and Remote Sensing Letters*, 10(1):14–18, 2013.

[230] Zhang, Yonghong; Wu, Hong'an; Wang, Huiqin, and Jin, Shanshan. Distance measure based change detectors for polarimetric sar imagery. *Photogrammetric Engineering & Remote Sensing*, 82(9):719–727, 2016.

[231] Zhang, Yudong; Wu, Lenan; Neggaz, Nabil; Wang, Shuihua, and Wei, Geng. Remote-sensing image classification based on an improved probabilistic neural network. *Sensors*, 9(9):7516–7539, 2009.

[232] Zheng, Honglei; Zhang, Yanmin, and Wang, Yunhua. Polarimetric features analysis of oil spills in c-band and l-band sar images. In *Geoscience and Remote Sensing Symposium (IGARSS), 2016 IEEE International*, pages 4683–4686. IEEE, 2016.

[233] Zheng, Jin and You, Hongjian. A new model-independent method for change detection in multitemporal sar images based on radon transform and jeffrey divergence. *IEEE Geoscience and Remote Sensing Letters*, 10(1):91–95, 2013.

[234] Zheng, Yaoguo; Zhang, Xiangrong; Hou, Biao, and Liu, Ganchao. Using combined difference image and k-means clustering for sar image change detection. *IEEE Geoscience and Remote Sensing Letters*, 11(3): 691–695, 2014.